

DISSOLUTION OF GRAIN BOUNDARY ALLOTRIOMORPHS IN
THE Al-Cu AND Al-Ag SYSTEMS

BY

ARISTEDES PASPARAKIS

B.Sc., University of Pretoria, 1964
M.Sc. (Tech.), University of Sheffield, 1967

A THESIS SUBMITTED IN PARTIAL FULFILMENT OF THE
REQUIREMENTS FOR THE DEGREE OF

DOCTOR OF PHILOSOPHY

in the Department

of

METALLURGY

We accept this thesis as conforming to the
required standard

THE UNIVERSITY OF BRITISH COLUMBIA

February, 1972

In presenting this thesis in partial fulfilment of the requirements for an advanced degree at the University of British Columbia, I agree that the Library shall make it freely available for reference and study. I further agree that permission for extensive copying of this thesis for scholarly purposes may be granted by the Head of my Department or by his representatives. It is understood that copying or publication of this thesis for financial gain shall not be allowed without my written permission.

Department of Metallurgy

The University of British Columbia
Vancouver 8, Canada

Date April 4, 1972

ABSTRACT

The dissolution behaviour of grain boundary allotriomorphs has been studied in the systems Al-Cu and Al-Ag. Using electron probe microanalysis, isoconcentration contours around dissolving allotriomorphs in an effectively infinite matrix have been determined. The influences of allotriomorph shape, grain boundary misorientation, solute supersaturation in the matrix, volume and grain boundary diffusion, and homologous temperature on the shape of these contours have been examined.

It was established that the shape of the isoconcentration contours is dependent only on homologous temperature (T_H) for both systems studied. Above $T_H = 0.92$, no grain boundary diffusion contribution to the dissolution process is observed. The grain boundary diffusion contribution was found to increase with decreasing T_H and to completely dominate the dissolution process below $T_H = 0.72$.

Using the back scattered electron image on the electron probe microanalyzer, the dissolution rate of individual grain boundary allotriomorphs was determined for various values of T_H , under conditions in which there was impingement of diffusion fields from adjacent precipitates. An exponential relationship between axial length or width and dissolution time was found to adequately describe the observed dissolution kinetics. A change in axial ratio accompanied the dissolution of the grain boundary allotriomorphs. At high T_H an increase in axial ratio with dissolution time was observed, whereas at low T_H , a decrease in axial ratio (i.e., spheroidization) was observed. A model has been proposed to account for this behaviour.

TABLE OF CONTENTS

	<u>Page</u>
1. INTRODUCTION	1
1.1 Grain Boundary Precipitates	1
1.2 Growth of Precipitates	4
1.2.1 Thickening of Grain Boundary Allotriomorphs.	5
1.2.2 Lengthening of Grain Boundary Allotriomorphs	6
1.2.3 The "Grain Boundary Collector Plate" Model .	6
1.3 Dissolution Studies of Precipitates	7
1.3.1 Observations of the Dissolution of Precipitates by Electron Microscopy	12
1.3.2 Dissolution Studies Using the Electron Probe Microanalyzer	16
1.4 Dissolution Mechanisms Derived from Precipitate Growth	16
1.5 Objective of Present Investigation	17
2. EXPERIMENTAL PROCEDURE	20
2.1 Reasons for Systems Chosen	20
2.2 Preparation of Master Alloys	21
2.3 Procedure Used to Grow Large Grain Boundary Allotriomorphs	24
2.4 Dissolution Heat Treatment Procedure	25
2.5 Diffusion Couple Work	28
2.6 Electron Probe Microanalysis	29
2.6.1 Isoconcentration Contours	29
2.6.1.1 Resolution of Experimental Technique	32
2.6.2 Kinetic Studies	36

	<u>Page</u>
2.6.3 Diffusion Couple Measurements	38
2.7 Validity of Experimental Technique	38
2.7.1 Isoconcentration Contour Measurements	38
2.7.2 Kinetic Measurements	41
3. ISOCONCENTRATION CONTOUR RESULTS AND DISCUSSION	44
3.1 Introduction	44
3.1.1 Diffusion Couple Results	45
3.1.2 The Microstructure of Equilibrated Alloys ..	49
3.1.3 Dissolution Isoconcentration Contours	50
3.2 Rate Controlling Mechanism	54
3.3 The Effect of Precipitate Shape [S_o/R_o]	56
3.4 Homologous Temperature [T_H]	60
3.4.1 Calculations of D_V and C_I	71
3.5 The Effect of Supersaturation (k) and Volume Diffusion Coefficient (D_V)	77
3.6 The Effect of Grain Boundary Misorientation (R) ...	81
3.6.1 Evaluation of the Grain Boundary Diffusion Coefficient($D_{g.b.}$).....	84
3.7 Semi-Quantitative Analysis of Isoconcentration Contours	89
3.8 The Al-15.75 wt.% Ag System	94
3.9 Applicability of Contours	99

	<u>Page</u>
4. KINETIC RESULTS AND DISCUSSION	101
4.1 Introduction	101
4.2 Application of the Existing Models for Dissolution Kinetics	102
4.3 An Exponential Model for Planar Dissolution Kinetics	111
4.4 Precipitate Shape Change During Dissolution	122
4.4.1 High Homologous Temperatures	131
4.4.2 Low Homologous Temperatures	137
4.4.3 Intermediate Homologous Temperatures	138
5. CONCLUSIONS	142
BIBLIOGRAPHY	144
APPENDIX I Correction Procedures for Quantitative Electron Probe Microanalysis	148
I.1 The Al-Cu System	148
I.2 The Al-Ag System	153
APPENDIX II Electron Spot Size Determination	156
APPENDIX III Calculation of the Flux Line Divergence for Different Sections of a Two Dimensional Elliptical geometry	159
APPENDIX IV D_V Calculation from the Diffusion Couple Results	162
APPENDIX V Calculation of Standard Deviation for the Isoconcentration Contours	164

	<u>Page</u>
APPENDIX VI Calculation of ψ	166
APPENDIX VII Calculations of the Impingement Resulting from the Interaction of the Confocal Spheroids About an Allotriomorph and a Surrounding Spherical Field	170

LIST OF FIGURES

<u>Figure</u>		<u>Page</u>
1	A schematic diagram of the "Grain Boundary Collector Plate" model showing the three steps that take place in the growth of grain boundary allotriomorphs	8
2	(a) Section of an equilibrium phase diagram showing T_G and T_D for an alloy of composition C_0 . (b) Dissolution composition profile for an alloy of composition C_0	10
3	A comparison of composition contours for (a) growth, (b) dissolution	18
4	(a) The aluminum-copper equilibrium phase diagram (b) The aluminum rich end of the aluminum-copper equilibrium phase diagram	22
5	The aluminum-silver equilibrium phase diagram	23
6	Optical micrograph of a typical alloy microstructure for the Al-2.81 wt.% Cu alloy	26
7	Schematic representation of the directions of movement of a specimen relative to the electron beam, in the electron probe microanalyzer	30
8	Optical micrograph of a typical grain boundary allotriomorph, with contamination marks showing the full extent of scans across the precipitate and grain boundary	31

<u>Figure</u>		<u>Page</u>
9	The (a) specimen current, (b) background concentration, and (c) Cu-K α_1 concentration, for the blank profile (1) Through the centre of the precipitate, (2) at the allotriomorph tip and (3) 5 μ away from the tip across the grain boundary	34
10	Schematic diagram depicting the effect of spot size on the evaluation of concentration C_1 at a point x_1 away from the precipitate interface	35
11	A schematic depiction of the dissolution flux lines for; (a) an allotriomorph sectioned above the minor axis b, (b) an allotriomorph sectioned at the minor axis and (c) an allotriomorph sectioned below the minor axis	35
12	Optical micrograph showing (a) electron probe traces across the bonded interface of an Al-CuAl $_2$ diffusion couple, (b) microstructure of large CuAl $_2$ grain in an $\alpha + \theta$ matrix	39
13	Dissolution isoconcentration contours of a grain boundary allotriomorph on the surface and 3 μ below the surface (A and B) and a second allotriomorph in the bulk material (C). At $T_H = 0.97$ for alloy A ...	40
14	Population distribution curve for allotriomorphs of varying axial ratio S_o/R_o for alloy A	42
15	Composition contour for Al-CuAl $_2$ diffusion couple at 500°C	46

<u>Figure</u>		<u>Page</u>
16	Probability plot of atomic % Cu versus diffusion distance (x) over the solid solubility range of the α phase for the 500°C diffusion couple	47
17	Arrhenius plot of D_V versus $1/T^\circ K^{-1}$ for the diffusion couple results	48
18	Size distribution (S_O) of precipitates as a function of S_O/R_O for alloy A	51
19	Isoconcentration contours at $T_H = 0.91$ for alloy B..	52
20	Concentration contour along the minor axis of a grain boundary allotriomorph at 545°C for alloy A ..	55
21	Isoconcentration contours for three allotriomorphs having axial ratios S_O/R_O of 1) 18, 2) 3.5, 3) 1.7 for alloy A at $T_H = 0.93$	57
22	Isoconcentration contours of two Widmanstätten plates for alloy A at $T_H = 0.93$	59
23	Isoconcentration contours for alloy A at $T_H = 0.97$..	62
24	Isoconcentration contours for alloy B at $T_H = 0.94$..	63
25	Isoconcentration contours for alloy B at $T_H = 0.92$..	64
26	Isoconcentration contours for alloy B at $T_H = 0.905$..	65
27	Isoconcentration contours for alloy B at $T_H = 0.86$..	66
28	Isoconcentration contours for alloy C at $T_H = 0.80$..	67
29	Isoconcentration contours for alloy C at $T_H = 0.77$..	68
30	Isoconcentration contour for alloy D at $T_H = 0.72$...	70
31	Interface concentration C_I versus \sqrt{Dt} for alloy B at $T_H = 0.92$	73

<u>Figure</u>		<u>Page</u>
32	C versus $\text{erf} \left(\frac{x}{2\sqrt{Dt}} \right)$ for alloy B at $T_H = 0.92$	74
33	Probability plot of $\left[\frac{C(x,t) - C_M}{C_I - C_M} \right]$ versus diffusion distance (x) for alloy B at $T_H = 0.92$	75
34	Isoconcentration contours for alloy A at $T_H = 0.92$..	79
35	Isoconcentration contours of two allotriomorph shaped precipitates situated on a low angle grain boundary for the Al-Ag alloy at $T_H = 0.84$	82
36	Isoconcentration contours for the Al-Ag alloy at $T_H = 0.84$	83
37	Schematic diagram for Shewmon surface diffusion model (after P.G. Shewmon)	85
38	Evaluation of $D_{g.b.}$ for alloy B at $T_H = 0.86$	86
39	The function $\frac{\text{flux via grain boundary diffusion}}{\text{flux via volume diffusion}} (\psi)$ versus temperature T.	91
40	A comparison of theoretically derived ψ versus homologous temperature T_H with the experimental observation of $\frac{\text{solute via grain boundary diffusion}}{\text{solute via volume diffusion}}$..	92
41	Schematic diagram of method used to calculate 1) solute via grain boundary diffusion, and 2) solute via volume diffusion	94
42	Isoconcentration contours for the Al-Ag alloy at $T_H = 0.885$	95
43	Isoconcentration contours for the Al-Ag alloy at $T_H = 0.93$	96

<u>Figure</u>		<u>Page</u>
44	Isoconcentration contour for alloy B at $T_H = 0.83...$	97
45	Isoconcentration contours for alloy B at $T_H = 0.885.$	98
46	Arrhenius plot of D_V versus $1/T^\circ K^{-1}$ for the Al-15.75 wt.% Ag alloy	100
47	A plot of R^2 versus t and R versus \sqrt{t} for alloy B at $T_H = 0.92$	104
48	Log $[S/S_O]$ versus t and log $[R/R_O]$ versus t for alloy A at $T_H = 0.97$	106
49	Log $[S/S_O]$ versus t and log $[R/R_O]$ versus t for alloy D at $T_H = 0.86$	107
50	Log $[S/S_O]$ versus t and log $[R/R_O]$ versus t for alloy B at $T_H = 0.86$	108
51	Log $[S/S_O]$ versus t and log $[R/R_O]$ versus t for alloy D at $T_H = 0.84$	109
52	Log $[S/S_O]$ versus t and log $[R/R_O]$ versus t for alloy D at $T_H = 0.76$	110
53	(a) Geometrical model of a particle with half-thickness R_O in a matrix with interparticle spacing ℓ . (b) An appropriate phase diagram with growth of precipitates taking place at T_1 and dissolution at T_2 , (c) Dissolution profile prior to impingement.	111
54	(a) The concentration distributions during dissolution after impingement takes place, (b) Schematic diagram of model used with a constant concentration C_2 , at $x = \ell$	112
		113

<u>Figure</u>		<u>Page</u>
55	R versus t for equations 11 and 12	117
56	Log $[R/R_0]$ versus t for dissolution of precipitates in an Al-4 wt.% Cu system at 520°C	119
57	Log $[R/R_0]$ versus t for the dissolution of planar precipitate in a finite system with $k = 0.22$	120
58	Arrhenius plot of D_v versus $1/T^\circ K^{-1}$ for the kinetic results	121
59	Back scattered electron image micrographs, used to observe the dissolution kinetics of an allotriomorph at $T_H = 0.97$ for alloy A	123
60	Back scattered electron image micrographs, used to observe the dissolution kinetics of an allotriomorph at $T_H = 0.97$ for alloy A	124
61	Back scattered electron image micrographs, used to observe the dissolution kinetics of an allotriomorph at $T_H = 0.88$ for the Al-Ag alloy	125
62	Back scattered electron image micrographs, used to observe the dissolution kinetics of an allotriomorph at $T_H = 0.88$ for alloy B	126
63	Back scattered electron image micrographs, used to observe the dissolution kinetics of an allotriomorph at $T_H = 0.84$ for the Al-Ag alloy	127
64	Fraction of precipitates showing an increase in axial ratio greater than 10% (F) versus super- saturation (k)	129

<u>Figure</u>		<u>Page</u>
65	Fraction of precipitates showing an increase in axial ratio greater than 10% (F) versus T_H	130
66	(a) Symmetrical distribution of precipitates with $[S_O/R_O] = 4$	131
	(b) Schematic representation of concentration fields around a symmetrical array of precipitates...	132
	(c) Diagram of spherically symmetrical field surrounding a grain boundary allotriomorph	132
67	The resulting impingement between the confocal spheroids isoconcentration contours about an allotriomorph and the contours of the surrounding spherical field after $t = 500$ seconds for various $[C/C_I]$ values	134
68	(a) $[C/C_I]$ versus x for the minor axis O_b	135
	(b) $[C/C_I]$ versus x for the equatorial plane O_a	136
69	Percentage increase in $[\frac{S_F/R_F}{S_O/R_O}]$ versus $[S_O/R_O]$	139
70	(a) $\log [R/R_O]$ versus t	
	(b) $[S/R]$ versus t	140
I-1	C_{Cu} versus K_{Cu}	152
I-2	C_{Ag} versus K_{Ag}	155
II-1	Schematic diagram of the electron spot size	157
III-1	Two dimensional sections of an oblate spheroid	159
IV-1	Composition profile of diffusion couple at $500^\circ C$	162
VII-1	Schematic diagram comparing actual contour to confocal spheroid	170

<u>Figure</u>	<u>Page</u>
VII-2 Position of error function profile	171
VII-3 Pertaining to Equation 4	172
VII-4 Schematic diagram of the summing up of two in- dependent profiles	174

LIST OF TABLES

<u>Table</u>		<u>Page</u>
I	Morphology Classification and Relationship to Boundary Misorientation	3
II	(a) Precipitate Growth Equations	13
	(b) Precipitate Dissolution Equations	14
III	Average S_o for Allotriomorphs with $S_o/R_o = 3.5$ and Average Width of Precipitate Free Zone for the Different Alloys	50
IV	Contour Experiments	61
V	Interface Concentration (C_I) and Volume Diffusion Coefficient (D_V) for Contour Experiments	75
VI	Comparison of the Effects of k , T and T_H on the Shape of Isoconcentration Contours	80
VII	Grain Boundary Diffusion Coefficients ($D_{g.b.}$) Determined from Contours.....	88
VIII	Kinetic Experiments	103
II-1	E_K , A , Z and ρ Values for Ag $L\alpha_1$, Al $K\alpha_1$ and Cu $K\alpha_1$ Radiation	156
III-1	$\Delta\theta^\circ$ for Different Values of x/b	160
IV-1	D_V Values of the Diffusion Couple Results	163
V-1	Diffusion Distances, \bar{x} , σ and $\frac{\bar{x}}{\sigma}$	164
VII-1	Values of $(\eta_1^2 - \beta^2)^{1/2}$ and η_1 of Confocal Spheroids for Different C/C_I Ratios	172
VII-2	Values of r for Concentric Spheres for Different C/C_I Ratios	173

ACKNOWLEDGEMENTS

The author would like to thank Dr. L.C. Brown for invaluable help and encouragement throughout the duration of this project.

Thanks are also due to Dr. D.E. Coates for numerous helpful discussions and guidance during the preparation of this thesis.

The criticisms and suggestions of Dr. E.B. Hawbolt, Dr. F. Weinberg and R.V. Krishnan of the final draft of the thesis are sincerely appreciated.

The assistance of the technical staff and in particular that of Mr. A. Lacis is greatly appreciated.

Thanks are extended to Mr. A. Bakas for his help with the figures and drawings for the thesis.

Financial assistance provided by the National Research Council under grant number A 2459, and the graduate fellowship awarded by the University of British Columbia are gratefully appreciated.

1. INTRODUCTION

The growth of precipitates in solid-state systems has been examined extensively and the results have been analysed theoretically on the basis of diffusion theory. Reasonably good correlation between experiment and theory has been obtained for grain boundary allotriomorph growth, by incorporating volume and grain boundary diffusion in the analysis. Much less experimental effort has been expended on the dissolution of precipitates and, as yet, no conclusive experimental observations have been made on the dissolution of grain boundary allotriomorphs. It has been suggested that the same analysis as used for allotriomorph growth is applicable to allotriomorph dissolution. For a number of reasons, which will be discussed later, this analysis is considered to be at best only a first approximation when applied to dissolution.

The theory pertinent to the growth and the dissolution of precipitates will follow a short discussion of the morphology of grain boundary precipitates.

1.1 Grain Boundary Precipitates

The morphology of grain boundary precipitates as a function of misorientation across the boundary on which they are situated was

originally studied and classified by Dube et al.¹ This classification was amended slightly by Aaronson.² In subsequent work Aaronson³ has shown that grain boundary misorientation can be characterized by the parameter R where:

$$R = \sqrt{X^2 + Y^2 + Z^2}$$

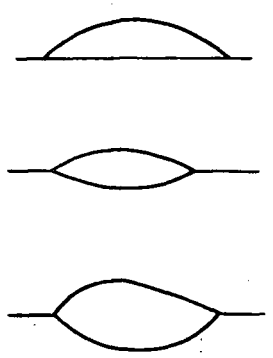
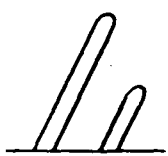
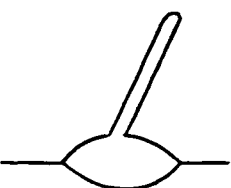
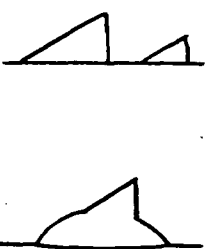

and X, Y, and Z represent the minimum rotations about the three orthogonal axes required to bring the two adjacent lattices into coincidence. This classification of precipitate morphology as a function of R is given in Table I. The fact that precipitate shape is a function of only R has been verified by the work of Toney and Aaronson⁴ in the Fe-Si system, Clark⁵ in the Al-18 wt.% Ag system and Hawbolt and Brown⁶ in the Ag-5.64 wt.% Al system.

Grain boundary allotriomorphs, the most common type of grain boundary precipitates, are confined to grain boundary misorientations of $R > 15^\circ$. These grain boundaries are considered to be high energy disordered boundaries and comprise a large proportion of the boundaries in a random polycrystal.⁷ The high energy of the boundaries is instrumental in: (i) grain boundary allotriomorphs being the first precipitates to nucleate and hence appear during growth, and (ii) allotriomorphs forming in preference to Widmanstätten plates at low degrees of supersaturation.

In general, allotriomorphs have an oblate spheroidal shape, being circular in the plane of the grain boundary and having a lens shaped

Table I⁶⁶

Morphology Classification and Relationship
to Boundary Misorientation

	Grain Boundary Allotriomorphs	Primary Sideplate	Widmanstätten Secondary Sideplates	Primary and Secondary Sawteeth	Idiomorphs
Morphology					
Grain Boundary Misorientation	Associated with large angle or disordered- type grain boundaries i.e., $>15^\circ$ misorientation.	Associated with small angle or dislocation type boundaries and grain interiors $<15^\circ$.	Generally associated with intermediate misorientations $15^\circ - 25^\circ$.	Generally associated with intermediate misorientations $15^\circ - 25^\circ$.	Usually an intragranular morphology although were observed for low angle grain boundaries in the Fe-1.55 Si system.

(Clark⁴, Dubé and Aaronson¹)

(elliptical) cross section. In the Al-18 wt.% Ag⁴ and the Al-4 wt.% Cu⁸ systems, the allotriomorph-matrix interface is generally found to be incoherent and the allotriomorphs develop equally in both grains. It has been noted,^{4,8} however, that nucleation often takes place in only one grain. This results in a planar, semi-coherent interface with a definite crystallographic relationship between the allotriomorph and the matrix grain. Initial growth of the allotriomorph takes place in the adjacent matrix grain. At a later stage of growth the semi-coherent interface becomes mobile followed by growth into both matrix grains.

In an examination of grain boundary ferrite precipitation from austenite in a Co-20% Fe alloy, Ryder and Pitsch⁹ and P.L. Ryder et al.¹⁰ found that grain boundary precipitates on high angle grain boundaries always have an orientation relationship with at least one and sometimes both of the austenite grains. However, they did not make sufficient measurements to determine whether the austenite-austenite relationships are completely random. Thus some doubt is cast on the observations of an orientation relationship between the precipitate and both grains.

1.2 Growth of Precipitates

Theoretical growth rate calculations for the diffusion-controlled growth of planar, cylindrical and spherical precipitates were originally made by Zener¹¹ and Frank.¹² These solutions were extended to cover the growth of spheroids and ellipsoids by Ham.^{13,14} The rate of growth of the major and minor axes of oblate spheroids, for various

axial ratios, was numerically evaluated by Horvay and Cahn.¹⁵ These solutions do not include impingement effects and are therefore only valid during the initial period of growth prior to the interaction of adjacent diffusion fields.

The experimental observations and analysis of the growth and dissolution of allotriomorphs reported in the literature is summarized below. First, growth is considered in terms of thickening and lengthening kinetics.

1.2.1 Thickening of Grain Boundary Allotriomorphs

The first measurements of growth kinetics of grain boundary allotriomorphs were made in commercial steels by Mazanec and Cadek¹⁶ and Hickley and Woodhead.¹⁷ Both reported a parabolic thickening rate for the growth of ferrite precipitates in bulk steel samples, which is consistent with diffusion controlled growth.

Hawbolt and Brown,⁶ using a statistical approach, found that at high homologous temperatures ($T_H > 0.90$) the thickness of β phase grain boundary allotriomorphs in the Ag-5.64 wt.% Al system increases parabolically with time. Aaron and Aaronson¹⁸ examined the thickening of $\theta(\text{CuAl}_2)$ grain boundary allotriomorphs in an Al-4 wt.% Cu alloy for homologous temperatures in the range $T_H = 0.54-0.69$. They assumed the true thickness to be that of the thickest allotriomorphs in a series of foils reacted for successively increasing times at each temperature. Their diffusion coefficients, calculated using Zener's¹¹ planar model, were found to be several orders of magnitude higher than the literature volume diffusion coefficients. They conclude

that at lower homologous temperatures grain boundary diffusion is operative and contributes to the enhanced growth rate.

1.2.2 Lengthening of Grain Boundary Allotriomorphs

Less data on the lengthening rate has been reported than on the thickening rate of grain boundary allotriomorphs. Dube et al.¹ and Aaronson³ measured the largest ferrite precipitate resulting from the Fe-C pro-eutectoid reaction and reported a linear lengthening rate up to impingement. Aaronson's results for the Fe-C system showed reasonable agreement with the lengthening rate equation proposed by Hillert.¹⁹ Hawbolt and Brown⁶ found that the lengthening of grain boundary allotriomorphs increases parabolically with time in the Ag-5.64 wt.% Al system at high homologous temperatures $T_H > 0.90$. At low homologous temperatures, Aaron and Aaronson¹⁸ found that the lengthening rate of grain boundary allotriomorphs in the Al-4% Cu system, cannot be adequately accounted for by the Hillert analysis¹⁹. This analysis gave D_V values several orders of magnitude higher than the literature value.

1.2.3 The "Grain Boundary Collector Plate" Model

The "grain boundary collector plate" model was formulated to account for the greatly enhanced growth kinetics observed by Aaron and Aaronson.¹⁸ This model makes use of the high diffusivity paths provided by the grain boundary and the disordered allotriomorph-matrix interface. The model assumes $D_{g.b.}/D_V \rightarrow \infty$, i.e. the volume diffusion contribution is insignificant, and grain boundary diffusion completely dominates the growth process. Growth of grain boundary allotriomorphs

according to this model occurs by:

1. volume diffusion of solute to the grain boundary;
2. solute transport along the grain boundary collector plate to the allotriomorph (a finite grain boundary area of half length $(R_C - R)$ is associated with each allotriomorph);
3. interphase boundary diffusion and deposition of solute over the surface of the growing allotriomorph as shown in Figures 1(a) and 1(b).

Brailsford and Aaron²⁰ modified the Aaron and Aaronson¹⁸ Collector Plate Model to accommodate situations in which the volume diffusion contribution is significant. The "Grain Boundary Collector Plate" model predicts a thickening rate proportional to $t^{0.5}$ and a lengthening rate proportional to $t^{0.25}$ for the experimental conditions used in the work of Aaron and Aaronson.¹⁸ These predicted rates are in reasonable agreement with the latter's experimental observations of thickening proportional to $t^{0.34}$ and lengthening proportional to $t^{0.27}$. Goldman et al.,²¹ using the Brailsford and Aaron²⁰ analysis for allotriomorph growth rates in the temperature range $T_H = 0.69-0.78$, found that volume diffusion directly to the allotriomorph contributes significantly to growth only at the highest homologous temperature ($T_H = 0.78$). Below this temperature the major contribution to growth is via grain boundary diffusion.

1.3 Dissolution Studies of Precipitates

Dissolution of precipitates occurs when a two-phase material is heated or cooled to a temperature where the precipitate phase becomes unstable. This results in mass transport from the unstable second phase

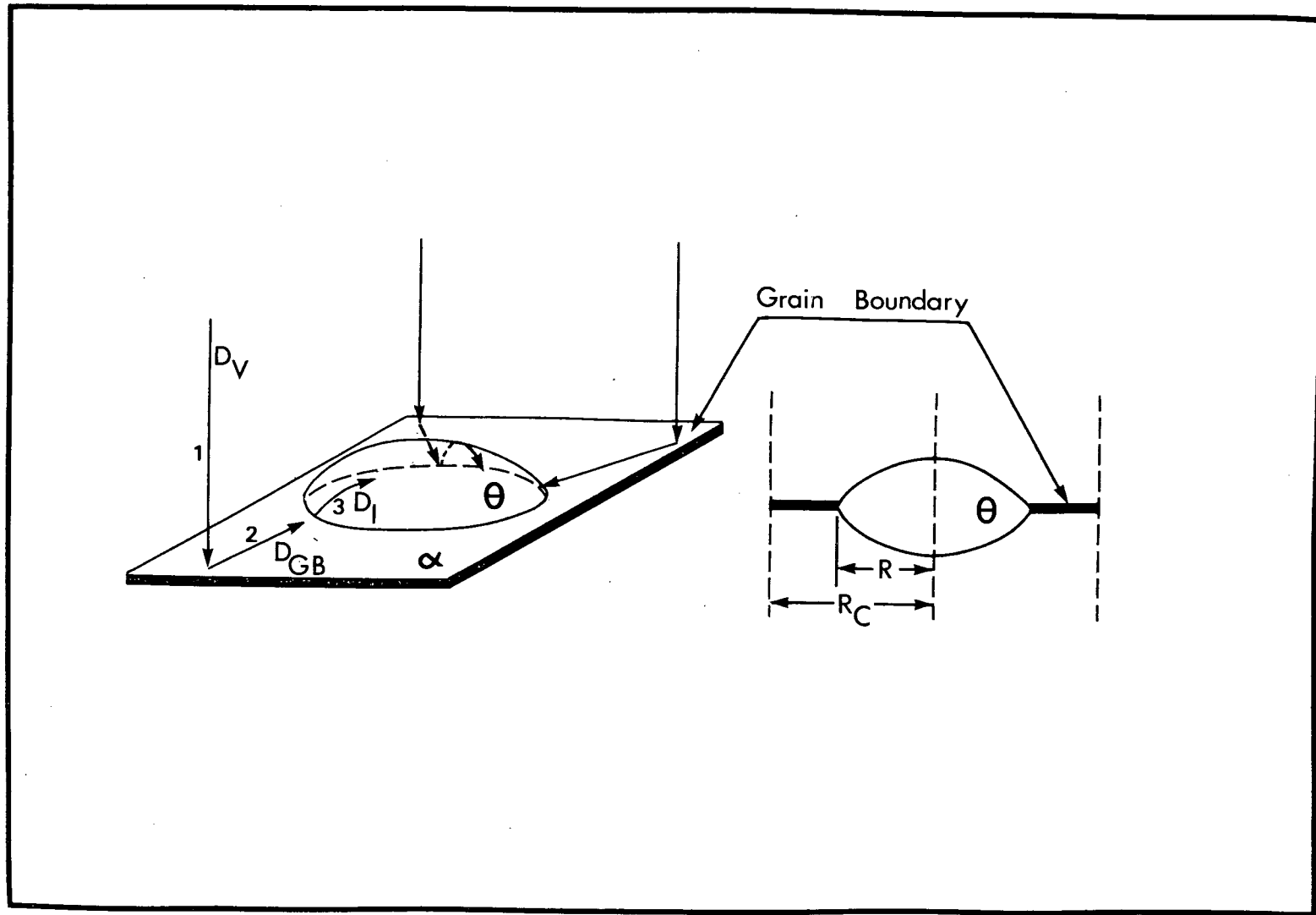


Figure 1. A schematic diagram of the "Grain Boundary Collector Plate" model showing the three steps that take place in the growth of grain boundary allotriomorphs.

to the stable matrix phase, as shown in Figure 2(a), where alloy C_0 may be present as either $(\alpha+\theta)$ or α , depending on the temperature. The dissolution composition profile for an alloy of composition C_0 , after instantaneous heating from T_G to T_D , is depicted in Figure 2(b).

The nomenclature is:

C_0 = equilibrium alloy concentration;

C_I = concentration in the matrix at the precipitate-matrix interface;

C_M = matrix concentration;

C_P = composition of precipitate;

T_G = precipitate growth temperature;

T_D = precipitate dissolution temperature.

Nolfi et al.²² developed analytical expressions for the growth and dissolution of spherical precipitates for diffusion controlled, interface reaction controlled, and mixed control mass transport. In subsequent experimental work on the dissolution of Fe_3C in ferrite, Nolfi et al.^{23,24} found that local equilibrium with respect to the iron is not maintained at the Fe_3C -ferrite interface. They conclude the dissolution of Fe_3C -ferrite is controlled entirely by an interfacial reaction.

Using a numerical method, Tanzili and Heckel^{25,26} treated: the diffusion controlled dissolution, from an unstable spherical, cylindrical or planar second phase to a stable finite matrix phase, as a function of D_α , C_I , D_θ , C_0 and R for complete precipitate solution and subsequent overall homogenisation of the matrix.

Because the present investigation is primarily concerned with diffusion controlled dissolution, it is appropriate that this topic be discussed in greater detail. For a spherical precipitate the

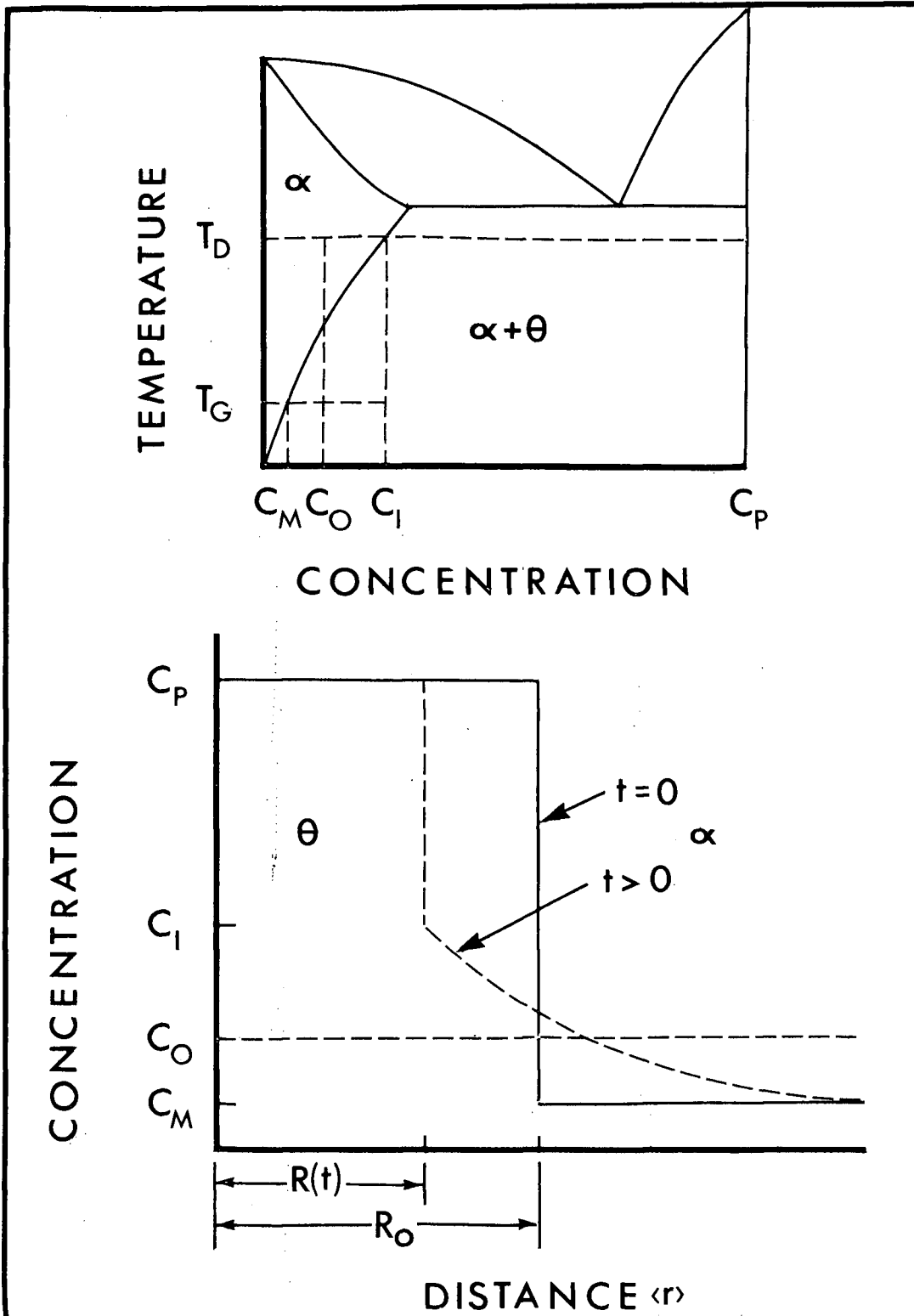


Figure 2. (a) Section of an equilibrium phase diagram showing T_G and T_D for an alloy of composition C_0 . (b) Dissolution composition profile for an alloy of composition C_0 .

diffusion field for diffusion controlled dissolution must satisfy the following field equation:

$$D \nabla^2 C = \frac{dC}{dt} \quad 1$$

where $C = C(r, t)$ is the concentration of solute in the matrix surrounding the precipitate, r (defined as in Figure 2(b)) is the distance from the centre of the precipitate, and it is assumed $D \neq D(C)$.

The following boundary conditions apply:

$$\begin{aligned} C(r = R, t) &= C_I & 0 < t \leq \infty \\ C(r, t=0) &= C_M & r \geq R \\ C(r = \infty, t) &= C_M & 0 \leq t \leq \infty \end{aligned} \quad 2$$

where R is the precipitate radius. C_I is the concentration in the matrix at the precipitate-matrix interface for $t > 0$ and C_M is the initial matrix composition. A further boundary condition is the interface flux balance:

$$(C_P - C_I) \frac{dR}{dt} = D \left. \frac{\partial C}{\partial r} \right|_{r=R} \quad 3$$

where it is assumed $C_P \neq C_P(r, t)$. This assumption is justified, as the change in composition of CuAl_2 over a range of 548°C is less than 0.5 wt.% Al (see Figure 4a).

Several approximations have been used to treat the diffusion controlled dissolution of an isolated precipitate in an infinite matrix. These models include the Reversed Growth model, the Laplace model ($\nabla^2 C = 0$), the Stationary Interface model ($\frac{dR}{dt} = 0$), and the Linearized Gradients model. Of these, the Stationary Interface approximation appears to be the most accurate. In a theoretical comparison of the different mathematical models for diffusion limited growth and dissolution, Aaron et al.²⁷ showed that the stationary interface approximation is the only one valid for both growth and dissolution of spherical and planar precipitates (see Table II).

1.3.1 Observations of the Dissolution of Precipitates by Electron Microscopy

Using electron microscopy at high homologous temperatures, Thomas and Whelan²⁸ (1960) observed precipitate dissolution in an Al-4 wt.% Cu alloy. They found that in the final stages of dissolution three out of twelve precipitates satisfy the following equation:

$$\frac{d(R^2)}{dt} = -kD \quad 4$$

They suggest that equation (4) should adequately describe solution kinetics for small k values where:

$$k = \frac{2(C_I - C_M)}{(C_P - C_I)} \quad 5$$

is the supersaturation. Equation (5) is derived by an approximation using the steady state diffusion theory, for small $\left(\frac{C_I - C_M}{C_P - C_I}\right)$ ratios.

TABLE II. PRECIPITATE GROWTH ²⁷

SPHERE

$$R = \lambda_j (Dt)^{\frac{1}{2}}$$

PLANE

$$S = \lambda_j (Dt)^{\frac{1}{2}}$$

Exact Solution	$\lambda_1 = 2\lambda$ $\lambda^2 e^{\lambda^2} [e^{-\lambda^2} - \lambda \sqrt{\pi} \operatorname{erfc} \lambda] = -\frac{k}{4}$	$\lambda_1 = 2\lambda$ $\sqrt{\pi} \lambda e^{\lambda^2} \operatorname{erfc} \lambda = -\frac{k}{2}$
	$\lim_{k \rightarrow 0} \lambda_1 = \lambda_2$ $\lim_{k \rightarrow 0} \lambda_1 = \lambda_3$ $k < 0: \lambda_1 > \lambda_2 > \lambda_3$ $\lim_{k \rightarrow 0} \lambda_1 = \lambda_4; k \neq -2; \lambda_1 > \lambda_4$	$\lim_{k \rightarrow 0} \lambda_1 = \lambda_2$ $k < 0: \lambda_1 > \lambda_2$ $ k > 1.98: \lambda_1 < \lambda_4$
Invariant Size Approx.	$\lambda_2 = \frac{-k}{2\sqrt{\pi}} + \sqrt{\frac{k^2}{4\pi} - k}$ $\lim_{k \rightarrow 0} \lambda_2 = \lambda_3$	$\lambda_2 = -k/\sqrt{\pi}$
Invariant Field Approx.	$\lambda_3 = \sqrt{-k}$	<p>NOT DEFINED (cannot satisfy the far field condition)</p>
Linearized Gradients Approx.	$f(k) = \left[\frac{-k}{1 + 4k} \right]^{\frac{1}{3}}$ $\gamma = \frac{1 - f(k)}{f(k)}$ $\lambda_4 = \sqrt{-k/\gamma}$	$\lambda_4 = \frac{k}{2(1 + \frac{k}{2})^{\frac{1}{2}}}$ $\lim_{k \rightarrow 0} \lambda_4 = -k/2$

Note: k , C_p , C_M , and C_I are defined in Section 1.3

The λ_j , $j = 1, 2, 3$, and 4 , correspond to the rate constants for the exact solution, invariant size, invariant field and linearized gradients approximations respectively.

TABLE IIb PRECIPITATE DISSOLUTION²⁷

	<u>SPHERE</u>	<u>PLANE</u>
		$S = S_o - \lambda_j (Dt)^{\frac{1}{2}}$
Exact Solution		$\lambda_1 = 2\lambda$ $\sqrt{\pi} \lambda e^{\lambda^2} \text{erfc}(-\lambda) = k/2$ <hr/> $\lim_{k \rightarrow 0} \lambda_1 = \lambda_2 > \lambda_4$ $k > 0: \lambda_2 > \lambda_1$ $0 \leq k \leq 1.5: \lambda_2 \geq \lambda_1 > \lambda_4$
Invariant Size Approx.	$\ln(y + 2p\sqrt{\tau} + y + \tau)$ $= \frac{-2p}{\sqrt{1-p^2}} \arctan\left(\frac{\sqrt{1-p^2}}{\frac{y}{\sqrt{\tau}} + p}\right)$ where $y = R/R_o, \quad \tau = \frac{a^2 t}{R_o^2}$ $a^2 = kD, \quad p^2 = k/4\pi$ and reduces to $y^2 = 1 - \tau$ in the limit as p (or k) goes to zero.	$\lambda_2 = k/\sqrt{\pi}$
Invariant Field Approx.	$R^2 = R_o^2 - kDt$ or $y^2 = 1 - \tau$	NOT DEFINED
Linearized Gradients Approx.	Sufficiently complex to negate its usefulness.	$\lambda_4 = \frac{(C_I - C_M)}{(C_P - C_M)^{\frac{1}{2}} (C_P - C_I)^{\frac{1}{2}}}$ $= \frac{k}{2(1 + \frac{k}{2})^{\frac{1}{2}}}$ <hr/> $\lim_{k \rightarrow 0} \lambda_4 = \frac{k}{2}$

The fact that only a small fraction of the precipitates observed obey equation (4) is attributed to surface diffusion enhancement of dissolution.

In most alloy systems of interest $|k| < 0.3$, and values of $|k| < 0.1$ are quite common. For this small k range, R is a slowly varying function of time, and the solution to equation (1) reduces to that obtained by assuming a stationary interface. Whelan²⁹ used the stationary interface approximation to obtain the following equation for the dissolution rate:

$$\frac{dR}{dt} = -\frac{k}{2} \left[D/R + \sqrt{\frac{D}{\pi t}} \right] \quad 6$$

The D/R term arises from the steady state part of the diffusion field (Equation 4), and the $\sqrt{\frac{D}{\pi t}}$ term arises from the transient part of the field. In the case of planar precipitates (the one dimensional case), there is only a transient term in the expression for dissolution rate, and one obtains:

$$R = R_o - k \sqrt{\frac{Dt}{\pi}} \quad 7$$

For spherical precipitates (the three dimensional case), both terms in equation (6) contribute to the dissolution rate. In the final stages of dissolution of spherical precipitates, the transient term becomes negligible and equation (6) reduces to equation (4). A good physical description of the diffusion fields around dissolving spheres is given by Readey and Cooper.³⁰

1.3.2 Dissolution Studies Using the Electron Probe Microanalyzer.

Hall and Hayworth³¹ used electron probe microanalysis to determine the concentration profiles around dissolving Widmanstätten plates and needles in an Al-5 wt.% Cu alloy. They found that at high homologous temperatures ($T_H = 0.91-0.95$), the plates dissolve via a volume diffusion mechanism and interface equilibrium is maintained. Eifert et al.³² used the probe to observe the β (B.C.C.) \rightarrow α (F.C.C.) transformation in the Cu-12.5 wt.% Al system. They reported a diffusion-controlled lattice transformation in which interface equilibrium is not maintained.

1.4 Dissolution Mechanisms Derived from Precipitate Growth

Both Tanzili and Heckel³³ and Aaron³⁴ have proposed an experimental procedure, based on theoretical considerations, whereby dissolution experiments may be used to determine the growth mode of precipitates. That the observed growth mode cannot be used to arrive at dissolution kinetics has been shown by Aaron et al.²⁷ In their treatment of dissolution at the reverse of growth, they show that to treat dissolution as the mathematical inverse of growth is at best a crude approximation, as the boundary conditions are intrinsically different in the two cases. Table II²⁷ summarizes the relationship between supersaturation (k) and transformation rate constant (λ_j), for the different mathematical models used to determine growth and dissolution kinetics.

It has further been shown by Nolfi et al.²² that curvature and interface reaction kinetics play an important part in the early stages of growth and that both tend to decrease the growth velocity.

Curvature effects on the other hand, are only important in the later stages of dissolution and tend to increase the dissolution velocity.

The inference that research on precipitate growth precludes the need for extensive direct investigation of precipitate dissolution, may be shown to be incorrect by the following reasoning.³⁵ In the case of growth, the formation of a critical nucleus, after some incubation time, is followed by the growth of the precipitate, causing depletion of solute in the matrix immediately ahead of the advancing interface (as shown in Figure 3(a)). At any position r in the matrix phase ($r > R(t)$), the solute concentration is a monotonically decreasing function of time. During dissolution, on the other hand, there is no incubation or nucleation period. The precipitate has a finite size (R_0) and decreases in size by mass transfer of solute into the matrix behind the receding interface (as shown in Figure 3(b)). The variation of solute concentration with time for dissolution is different and more complex than in growth. At a position well away from the precipitate ($\infty > r \gg R(t)$), the solute concentration increases with time; close to the precipitate ($r > R(t)$), the concentration decreases with time; and at intermediate positions, the solute concentration will increase, decrease or remain unchanged. Furthermore, the extent of the regions corresponding to 'near', 'intermediate' and 'far' vary with time.

1.5 Objective of Present Investigation

The purpose of the present investigation is to provide experimental data on the dissolution of grain boundary allotriomorphs and thereby

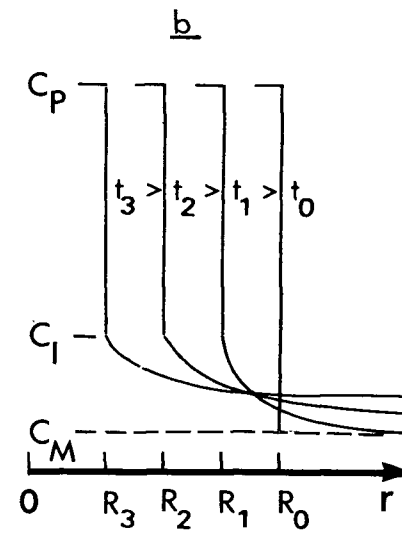
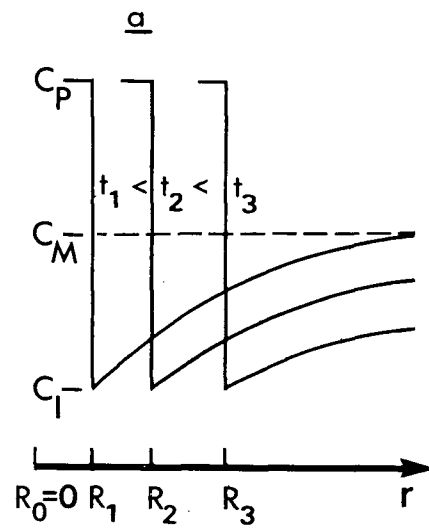


Figure 3. A comparison of composition contours for (a) growth, (b) dissolution.³⁵

elucidate the dissolution process. An attempt to arrive at a satisfactory theoretical analysis to account for the results will be made.

The atomic processes involved in dissolution of precipitates have thus far been indirectly deduced from statistical and other related kinetic measurements. The objective of this investigation is to determine the mechanisms of the dissolution phenomenon in a more direct and fundamental way by the use of electron probe microanalysis.

2. EXPERIMENTAL PROCEDURE

The electron probe microanalyzer was used as an instrument for both quantitative and qualitative analysis. Quantitative electron probe microanalysis was used to determine the concentration profiles around dissolving grain boundary allotriomorphs. A technique was established whereby the concentration profiles around a single precipitate were measured as a function of dissolution time. Kinetic studies of the dissolution rate of grain boundary allotriomorphs were made using the back-scattered electron image on the electron probe to determine the size of a precipitate as a function of dissolution time. Here once again, the dissolution of individual precipitates was observed.

2.1 Reasons for Systems Chosen

The aluminium-copper system was chosen for the following reasons:

1. the solidus composition changes rapidly with temperature, giving rise to a significant variation in concentration around a dissolving precipitate, see the phase diagram (Figure 4);^{36,37}
2. the low vapour pressure of the alloy at the experimental temperatures;
3. the existence of reliable phase diagram data;

4. the well-established relationship between precipitate shape and grain boundary misorientations; and another consideration is

5. the high degree of accuracy that can be achieved in the quantitative analysis of these alloys using the electron probe microanalyzer.

This accuracy is due to the small correction required to convert measured Cu X-ray intensity to weight percent of Cu present in an alloy.

The aluminium-silver system³⁶, (Figure 5), was chosen for supplementary experiments as it also fulfills all the above criteria.

2.2 Preparation of Master Alloys

Four Al-Cu master alloys (A, B, C, and D) of composition Al-4.83wt.% Cu, Al-2.81wt.% Cu, Al-1.57wt.% Cu, and Al-1.22wt.% Cu were prepared by melting 99.99% pure copper and 99.99% pure aluminium in a graphite crucible at 720°C. This was followed by casting in a split graphite mold to produce a slab of dimensions 6"x 2 3/8" x 1/2". An aluminium-15.75 wt.% silver alloy was produced in the same way using silver of 99.95% purity.

Following casting, the slabs were homogenized for seven days at 550°C, then cold-rolled in several passes to give a reduction in thickness of 50%. This was followed by a two hour anneal at 550°C and further cold rolling to give a final sheet thickness of 0.05". The sheet was then given a final anneal at 550°C for five days. The resultant sheet had an equiaxed grain structure, the grain size varying from 2.5 to 4 mm. The grain boundaries were straight and extended from the top to the bottom surface of the sheet. The majority of the grain boundaries were found to be stable on subsequent heat treatment.

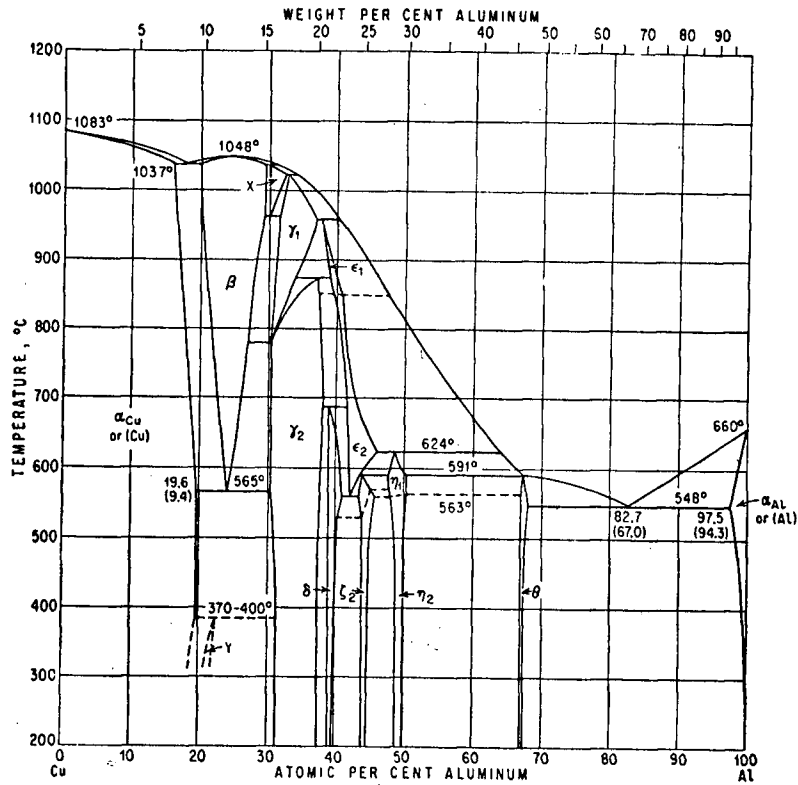


Figure 4. (a) The aluminum-copper equilibrium phase diagram.³⁶

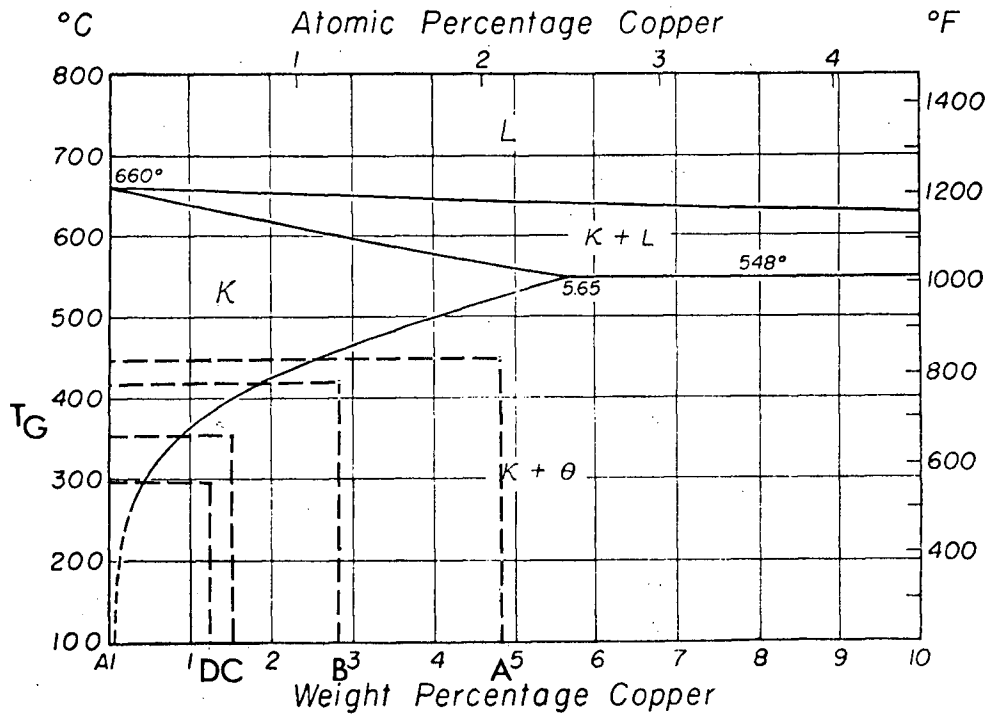


Figure 4. (b) The aluminum rich end of the aluminum-copper equilibrium phase diagram.³⁷

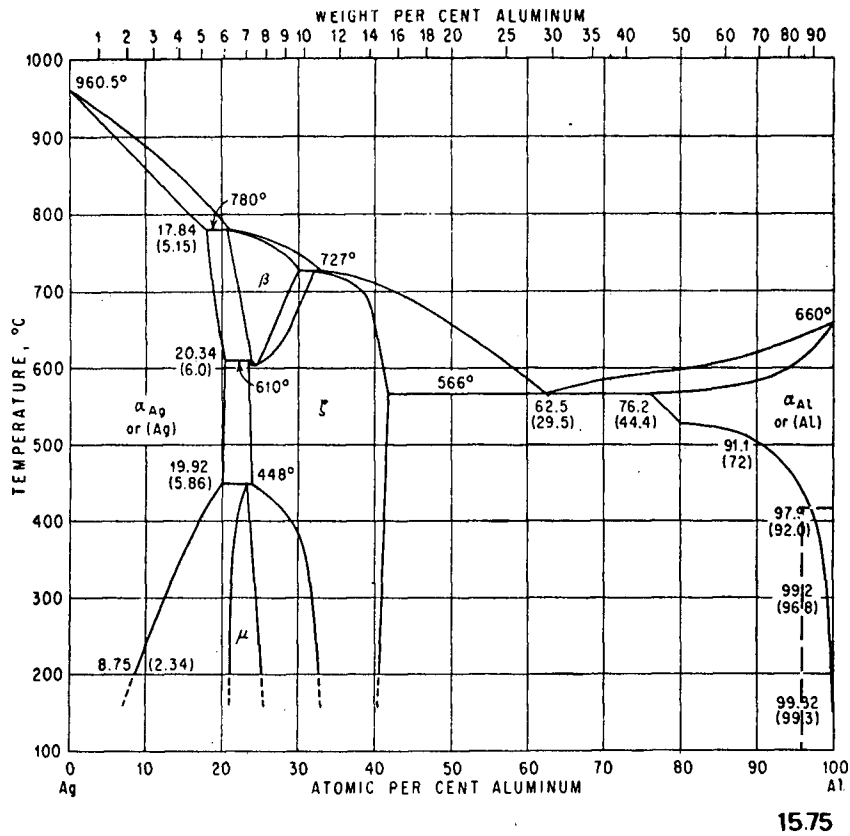


Figure 5. The aluminum-silver equilibrium phase diagram. ³⁶

The copper content of the aluminium-copper alloys, as well as the silver content of the aluminium-silver alloy, were determined using two different techniques: (the analyses were performed by Warnock-Hersey International Ltd. and Cantest Ltd.).

(a) The Atomic Absorption technique, which has an accuracy of $\pm 0.02\%$ up to 2% Cu and $\pm 0.05\%$ for up to 5% Cu.

(b) The electroplating of copper on a platinum electrode, which has an accuracy of 0.02% for the range of interest. The analyses were in all cases within $\pm 0.08\%$ of the cast alloy compositions based on the weight of components used. Microscopic sections of specimens were scanned in the electron probe microanalyzer to evaluate the homogeneity of the material. No significant microsegregation was detected in a series of samples taken across the width of the sheet.

2.3 Procedure Used to Grow Large Grain Boundary Allotriomorphs

To study the concentration profiles associated with individual precipitates, a heat treating procedure had to be established which would produce: (1) a minimum number of precipitates, (2) precipitates large enough in size for accurate probe analysis (thickness of precipitates $> 4\mu$), and (3) large precipitate free zones adjacent to the grain boundaries, as well as large interparticle spacings on the grain boundaries to avoid the impingement of neighbouring diffusion fields at short dissolution times. The desired microstructure was produced in the following way.

Ten discs of 1 1/4" diameter were cut from the final sheet of a particular alloy. These discs were tightly stacked together, tied with

chromel wire, and a hole 1/16" in diameter was made through half of the discs to accommodate a temperature controlling chromel-alumel thermocouple.

The assembly was inserted into a 2" diameter vertical tube furnace with a 4" long maximum temperature zone at 550°C. The temperature was controlled to within $\pm 1^\circ\text{C}$ for prolonged periods using a deviation amplifier. After three days the temperature of the furnace was reduced slowly to a temperature approximately 10°C above the phase diagram solvus temperature. Further cooling at 3°C per day was used to nucleate and grow precipitates. The slow cooling was continued until the precipitates had grown to a suitable size for analysis. The sample was then allowed to equilibrate for seven days to remove any concentration gradients introduced into the matrix by the precipitate growth. The samples were finally quenched in ice water from the equilibration temperatures (T_G) (as depicted in Figures 4 and 5). A typical equilibrated microstructure is shown in Figure 6.

Small test samples were quenched and optically inspected at various stages of the heat treatment. It was established that nucleation occurred at temperatures within $\pm 3^\circ\text{C}$ of the literature phase diagram solvus temperature. The number of grain boundary allotriomorphs present just below the solvus was comparable to that observed in the equilibrated structure.

2.4 Dissolution Heat Treatment Procedure

Specimens approximately 3/8" x 1/4" were cut from the discs (in some cases spark machined), cold mounted and polished to 1 μ diamond.

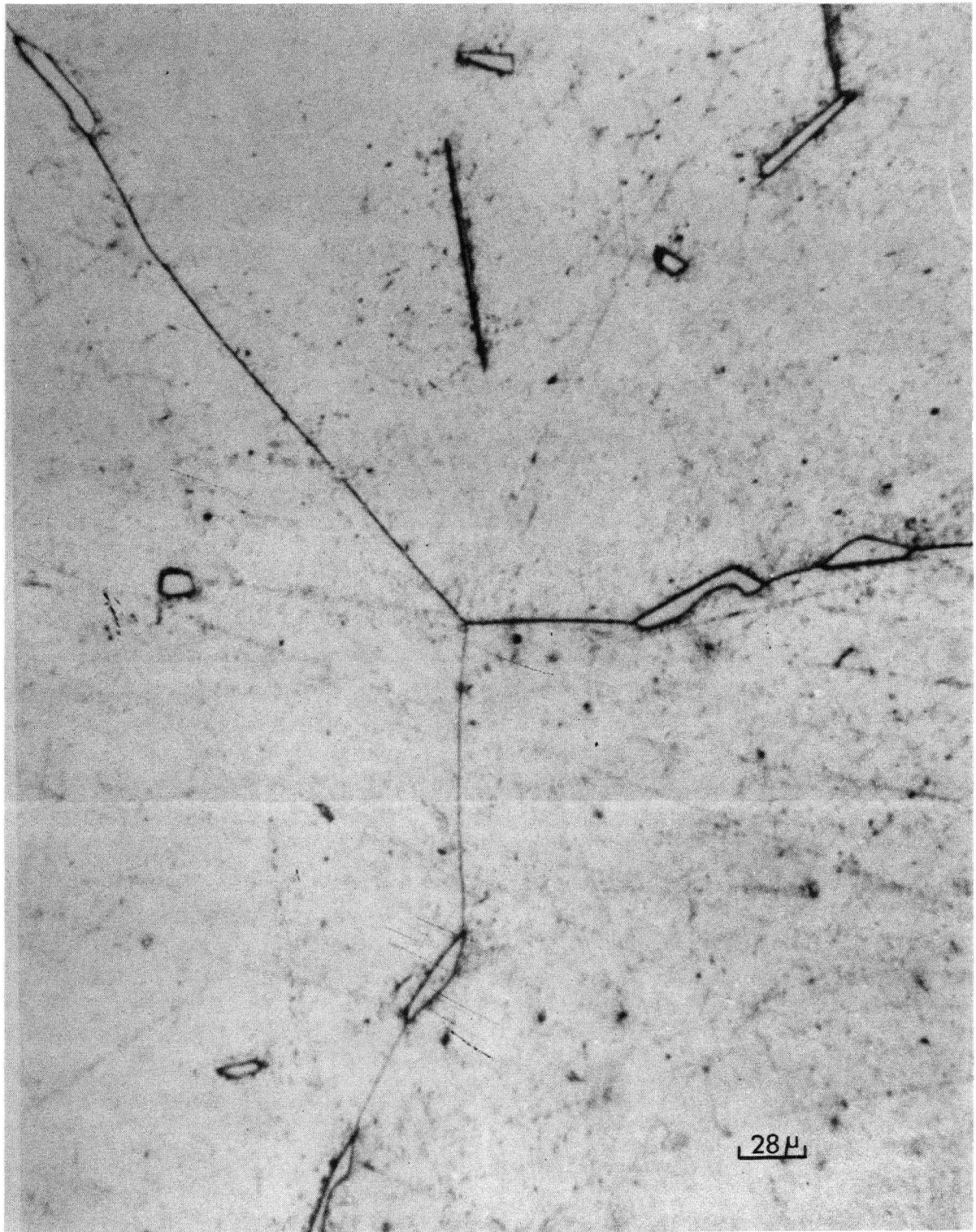


Figure 6. Optical micrograph of a typical alloy microstructure for the Al-2.81 wt.% Cu alloy.

Mechanical polishing, was used in preference to electro-polishing, as this resulted in a surface finish more suitable for microprobe analysis. Polishing produced a slight etching of the surface in the case of the Al-4.83 wt.% Cu, the Al-2.83 wt.% Cu and the Al-Ag alloy, facilitating the location of appropriate grain boundary allotriomorphs. For the other alloys suitable allotriomorphs were selected using the absorbed electron image on the microprobe, thus eliminating the need for etching the specimen to outline the structure.

The same precipitates could be relocated after several heat treatments by the probe contamination marks and by micro-hardness indentations made at strategic points on the surface. For dissolution heat treatment, the specimens were immersed in a 60% KNO_3 -40% NaNO_3 salt bath controlled to $\pm 1^\circ\text{C}$ by a steady state power input unit. Surface contamination by the salt was avoided by wrapping the specimens in 0.0005" thick, high purity tantalum foil. The salt did not penetrate the wrapping foil because of the high viscosity of the salt at the temperatures used. The immersion of the small mass of the sample produced a negligible temperature change in the salt ($< 1^\circ\text{C}$). Temperature stabilization occurred in less than 30 seconds after immersion of the specimen in the salt. It is estimated that the specimen reached bath temperature within two seconds of immersion in the salt. After heat treatment the specimens were quenched in water, the transfer time from the salt to the beaker being less than 1.5 seconds.

Using this procedure, as many as twenty successive heat treatments

were carried out on some specimens without any observable trace of surface contamination by the salt.

2.5 Diffusion Couple Work

Diffusion couples were prepared by clamping an aluminium bi-crystal, with a grain boundary angle $R = 17^\circ$, to a specimen with a structure containing large grains of CuAl_2 surrounded by a fine eutectic of $\alpha + \theta$ (see Figure 12(b)). The aluminium bi-crystal was used to permit the measurement of both grain boundary and volume diffusion coefficients. The specimen containing the CuAl_2 grains was produced by melting stoichiometric amounts of copper (53 wt.%) and aluminium in a vacuum sealed quartz tube at 700°C and quenching in brine. Several attempts were made to produce pure CuAl_2 without success.

The bonding surfaces of both the aluminium and the CuAl_2 were polished to $6\ \mu$ diamond and ultrasonically cleaned prior to bonding. The couples were diffused at a fixed temperature in a cracked ammonia atmosphere. The temperature-controlling thermocouple was placed just above the couple and the maximum temperature fluctuation registered was $< 3^\circ\text{C}$. Unfortunately, bonding was achieved only in four couples at temperatures of 480°C , 500°C , 520°C , and 535°C . Repeated attempts at lower temperatures were unsuccessful, probably due to the presence of the oxide film on the aluminium.

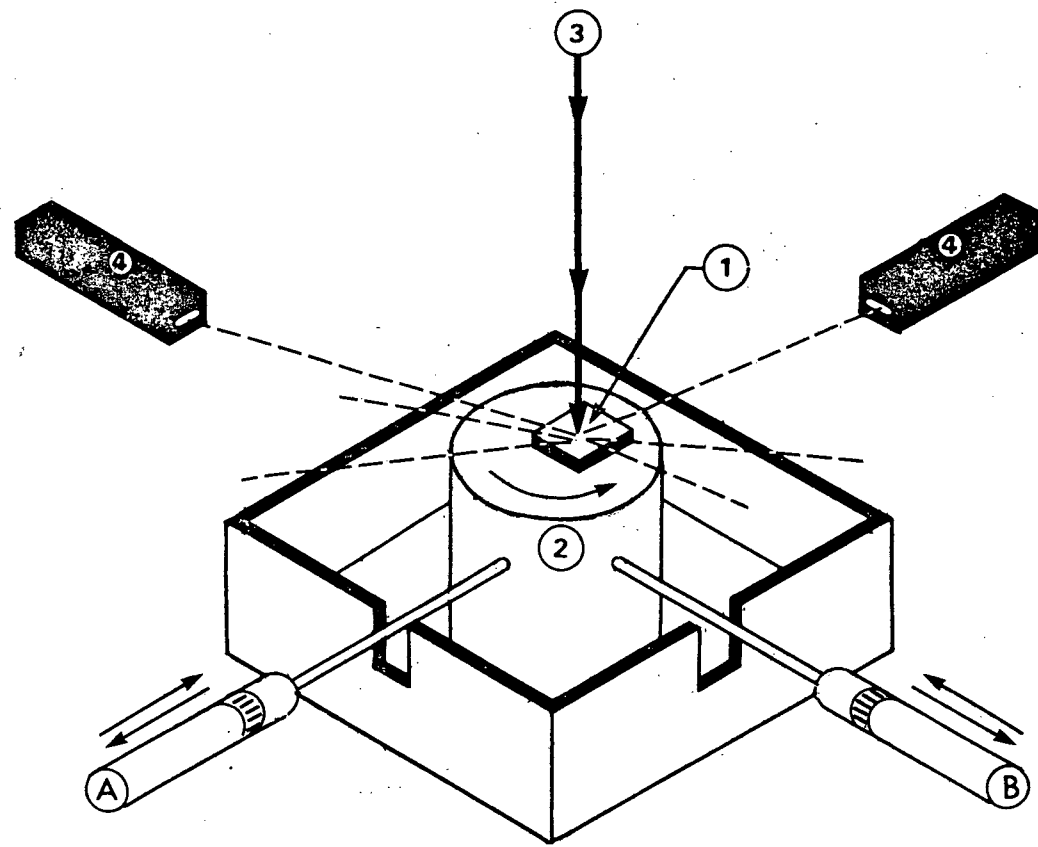
2.6 Electron Probe Microanalysis

2.6.1 Isoconcentration Contours

A JEOLCO (JXA-3A) electron probe microanalyzer with a step-scan attachment was used to determine the composition contours around dissolving grain boundary allotriomorphs. Figure 7 gives a schematic representation of the specimen in the microprobe specimen holder and the micrometer screws, as well as the possible directions of movement of the specimen. The step-scan attachment is an electronic device that may be attached to either of the micrometer screws to automatically displace the specimen relative to the electron beam by steps of 1.25 μ , 5 μ or 20 μ . Most of the measurements in this investigation used 1.25 μ step scanning. Each displacement is followed by a stationary spot count of 10 seconds and the resultant counts are registered automatically.

Grain boundary allotriomorphs situated on straight grain boundaries were selected for investigation and were rotated into a position perpendicular to one micrometer. Step scanning was then carried out across the width of the precipitate into the matrix. The scan was continued until the equilibrium matrix concentration was reached. This procedure was repeated along the length of the precipitate and the adjacent grain boundary. The scanning procedure is depicted in Figure 8. The dark contamination streaks mark the trace of each scan. An initial trace was taken on each precipitate before any dissolution heat treatment was carried out to give a blank profile.

In the analysis of the Al-Cu alloys, one spectrometer was set to coincide with the $\text{CuK}\alpha_1$ peak and the second was set at 30' above the



- 1 Specimen
- 2 Rotating Specimen Holder
- 3 Electron Beam
- 4 Spectrometers
- A&B Micrometer Screws
- X-Rays

Figure 7. Schematic representation of the directions of movement of a specimen relative to the electron beam, in the electron probe microanalyzer.

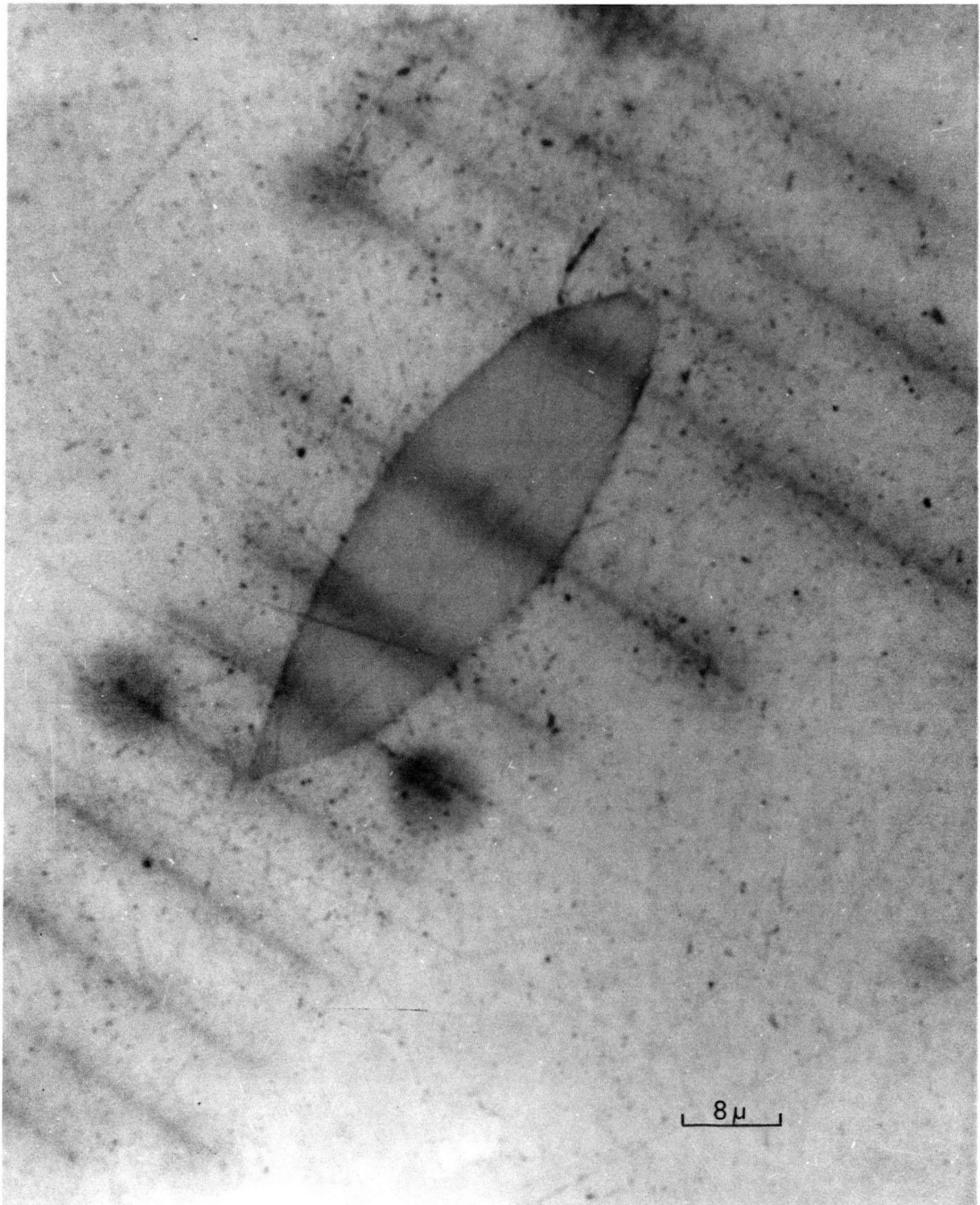


Figure 8. Optical micrograph of a typical grain boundary allotriomorph, with contamination marks showing the full extent of scans across the precipitate and grain boundary.

CuK α_1 peak to measure the background radiation intensity. These settings were chosen in preference to the Al L α_1 radiation because the maximum variation of the aluminium concentration in these alloys is between 95 wt.% and 98.5 wt.% Al, and therefore cannot be picked up with any degree of accuracy. In the Al-Ag alloy, the Ag L α_1 peak and a background at 30' above the peak were registered.

Appendix I gives the details of the correction procedure used to convert measured Cu K α_1 and Ag L α_1 intensities to weight percent copper and weight percent silver, respectively.

2.6.1.1 Resolution of Experimental Technique

The accelerating potential used in the evaluation of the concentration profiles was 25 K.V. This satisfies the criterion³⁸ which has been established for optimum accuracy in quantitative analysis;

$$\frac{V}{V_K} \approx 3$$

where: V = accelerating potential

V_K = excitation potential for any particular radiation.

The principal resolution limitation in quantitative electron probe microanalysis is the finite spot size (i.e., the volume from which X-rays are generated for any one spot count). The experimental conditions in this work resulted in a theoretically-calculated spot size of about 6 μ in diameter in the aluminium-rich matrix, and 3 μ in diameter in the copper-rich CuAl₂. In the Al-Ag alloy, the spot size is approximately 5 μ in the aluminium-rich matrix and 2.5 μ in the silver-rich phase (see Appendix II for calculations). The spot

size was also determined experimentally from the measured Cu concentration in the matrix adjacent to a precipitate interface. A copper concentration above the equilibrium matrix concentration was found to extend over a distance of approximately 5μ in the blank profile (Figure 9). This increase at a distance 5μ away from the determined interface was never greater than 1-2% above the matrix composition. Since 1.25μ step scanning was used, the effective spot size will be $> 3.75 \mu$ in radius, which is in good agreement with the theoretically calculated value.

That step-scanning in 1.25μ steps gives meaningful values of concentration, even though the spot size is $\approx 3.75 \mu$ in radius, may be appreciated if one considers that an error function profile ($\text{erf } x$) of C versus x is very close to a linear profile over the range $x = 0$ to $x = 0.8$. Accordingly for a linear composition profile, adjacent to the allotriomorph interface, the mean composition of the circular area with centre x_1 as in Figure 10, is equal to the C_1 the composition at the point x_1 .

In the present work the spot size limits the X-ray resolution at the precipitate-matrix interface and the grain boundary. The position of the precipitate-matrix interface was determined from the blank profile by a large decrease in specimen current and a sudden increase in background count, associated with going from the aluminium-rich matrix to the copper-rich precipitate (see Figure 9).

The grain boundary position was roughly established from the position of adjacent precipitates, to the precipitate being observed, along the grain boundary (see Figure 6). It was found that the maximum solute concentration on traversing a grain boundary

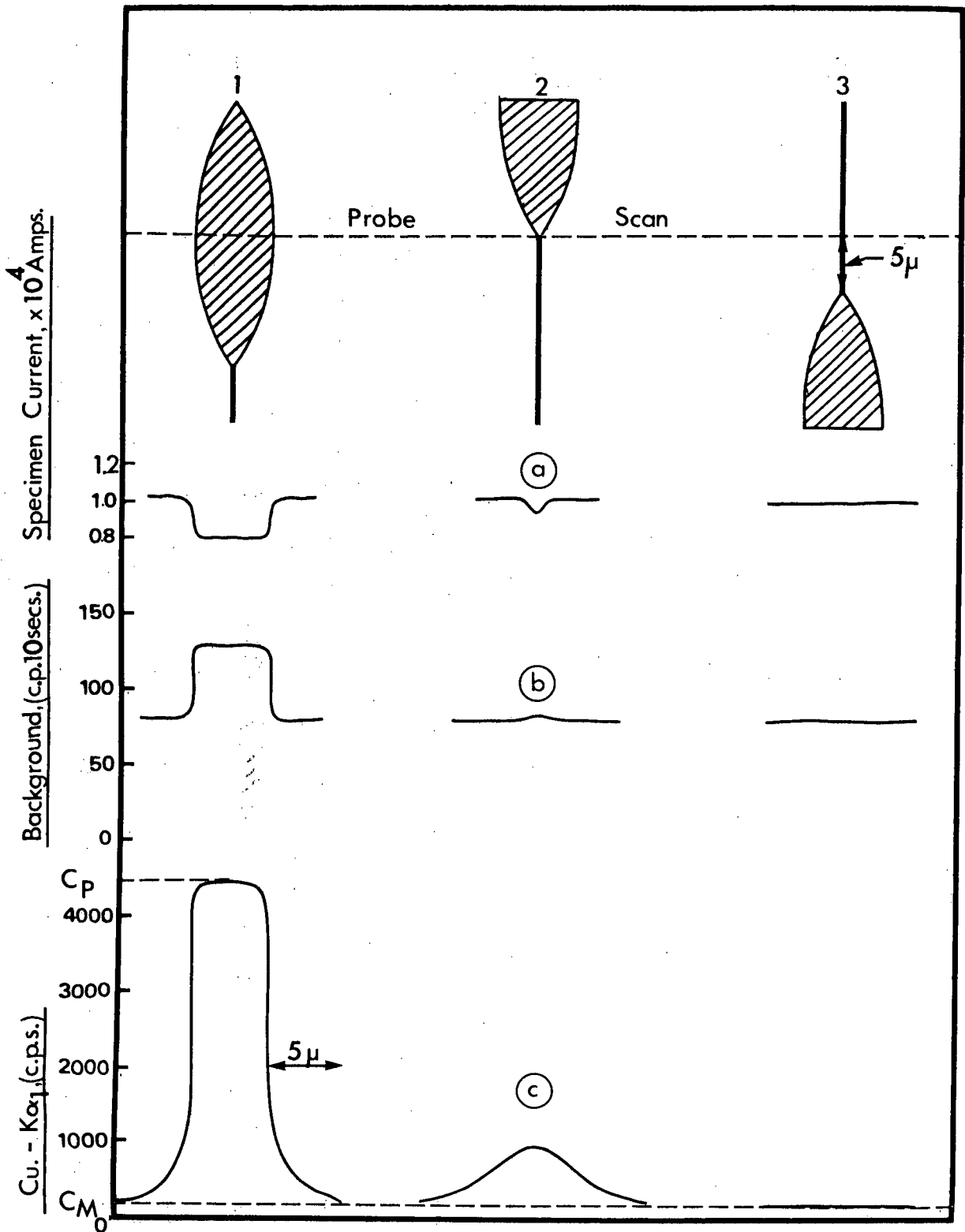


Figure 9. The (a) specimen current, (b) background concentration, and (c) Cu-Kα₁ concentration, for the blank profile (1) through the centre of the precipitate, (2) at the allotriomorph tip and (3) 5 μm away from the tip across the grain boundary.

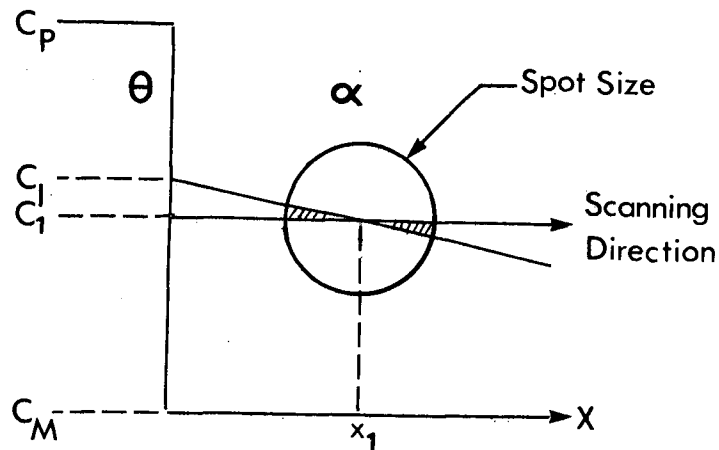


Figure 10. Schematic diagram depicting the effect of spot size on the evaluation of concentration C_1 at a point x_1 away from the precipitate interface.

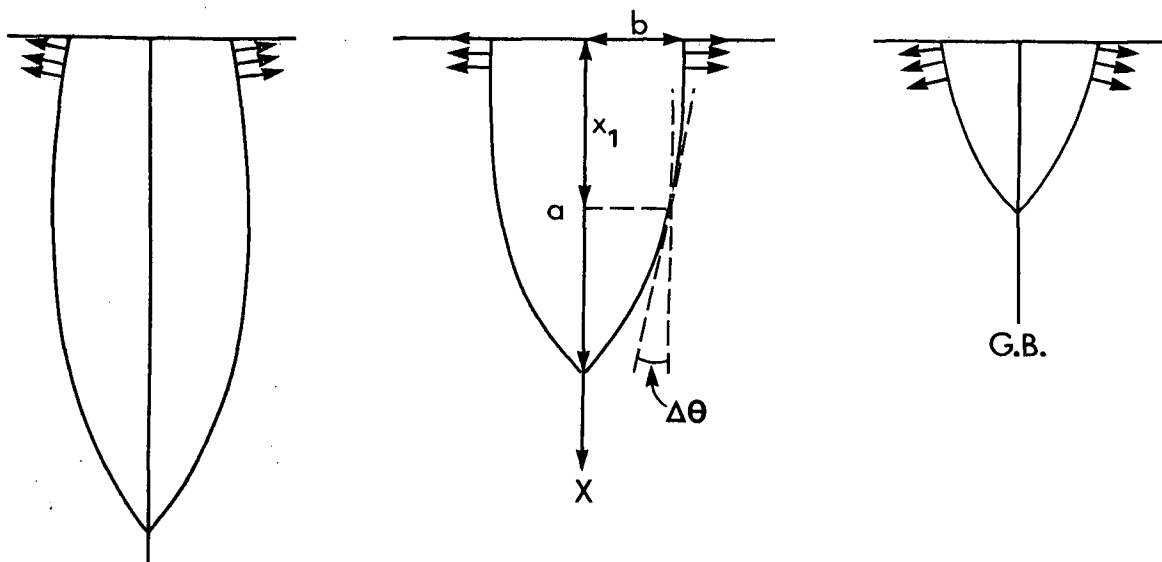


Figure 11. A schematic depiction of the dissolution flux lines for; (a) an allotriomorph sectioned above the minor axis b , (b) an allotriomorph sectioned at the minor axis, and (c) an allotriomorph sectioned below the minor axis.

invariably coincided with the position of the grain boundary as established from the back scattered electron image. Concentration gradients on either side of the maximum concentration were also very similar, providing further verification of the grain boundary position.

2.6.2 Kinetic Studies

Attempts were made to study precipitate dissolution by heat-treating the specimen, etching and examining the micro-structure using an optical microscope. As it was necessary to polish the specimen each time prior to etching, a different position on the precipitate was observed after each heat treatment. Thus the resulting data is not useful for a kinetic analysis.

The back-scattered electron image (b.s.e.i.) of the microprobe proved much more satisfactory since it did not require etching of the specimen. The experimental procedure developed approximates very well the direct observation of precipitate dissolution. The procedure involves photographing the back-scattered electron image of individual grain boundary allotriomorphs after successive heat treatments in the salt. A polaroid camera, attached to a monitor on the microprobe console, was used with polaroid N52 type film.

The largest allotriomorphs found in any one specimen were used for kinetic studies. This was done to ensure that the allotriomorphs studied were sectioned as close to the maximum diameter as possible. As shown in Figure 11, precipitates sectioned above the maximum half length will dissolve more slowly than precipitates sectioned through the

center, whereas precipitates sectioned below the maximum half length will dissolve faster.

For the two-dimensional elliptical geometry depicted in Figure 11, the divergence of the flux lines at x_1 , (Figure 11(b)), may be related to the change in the angle of the tangent at x_1 , relative to the tangent at the maximum half thickness b .

For an ellipse with an axial ratio of 3.5 to 1, the change in angle $\Delta\theta$ is 4° and 10° for x_1 equal to $0.25a$ and $0.5a$ respectively (see Appendix III for calculations). As the precaution was taken to study the dissolution of only the largest grain boundary allotriomorphs in any one sample, the effect of the flux line divergence, which as calculated is quite small, is considered negligible in this work. Photographic observations were made at magnifications of $\times 500$, $\times 1000$, $\times 2084$, and $\times 4168$; at higher magnifications the resolution was found to be impaired.

Measurements of the length of precipitates were made directly from the photograph to within $0.001''$ using vernier callipers. The thickness measurement was made at a position halfway between the tips of the precipitate.

The lengthy heat treatments in this part of the work increased the possibility of contamination by the salt, of grain boundary migration and of extensive thermal grooving of the grain boundaries. If there was any detectable evidence of contamination of the specimen surface, the specimen was rejected.

2.6.3 Diffusion Couple Measurements

An etchant of composition 47% HCl, 6% HI and 47% H₂O, when freshly prepared, delineated the copper composition in diffusion couples. The etchant was used to outline the diffusion field and thus to verify the extent of bonding which had taken place.

For each successfully prepared diffusion couple, at least two composition profiles (in some cases three) were taken across the centre of the two largest CuAl₂ grains at the bonded interface (see Figure 12(a)). The step scan device was used, and in most cases 1.25 μ steps were taken.

2.7 Validity of Experimental Technique

2.7.1 Isoconcentration Contour Measurements

The validity of the experimental technique depends on whether the dissolution contours measured on the sample surface are representative of those present about precipitates in the interior of the sample.

Experiments were carried out to establish that the surface measurements in this investigation are representative of the bulk material. This was done by measuring dissolution contours as follows:

- (A) around a given precipitate at the surface;
- (B) around the same precipitate after a layer of material 2-3 μ thick was carefully removed from the specimen surface; and
- (C) around a second precipitate in the bulk material.

The resultant dissolution contours are shown in Figure 13. Within reasonable scatter results (A), (B) and (C) coincide, ruling out any

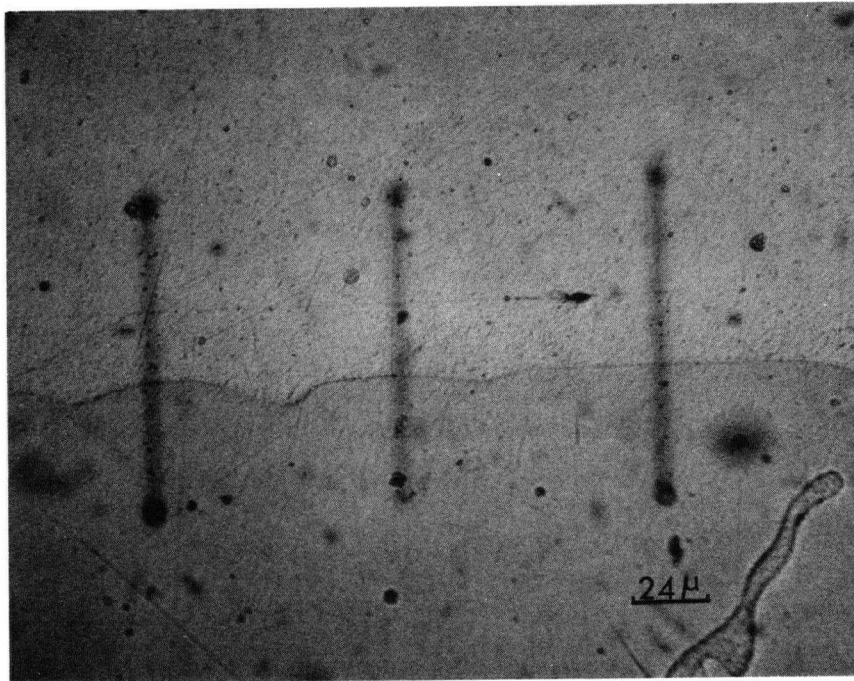


Figure 12(a). Optical micrograph showing electron probe traces across the bonded interface of an Al-CuAl₂ diffusion couple.

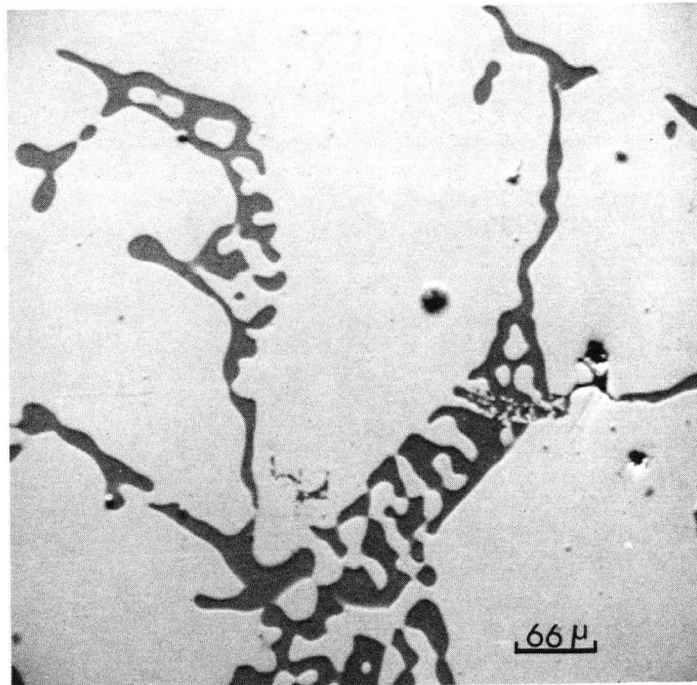


Figure 12(b). Microstructure of large CuAl₂ grain in an $\alpha + \theta$ matrix.

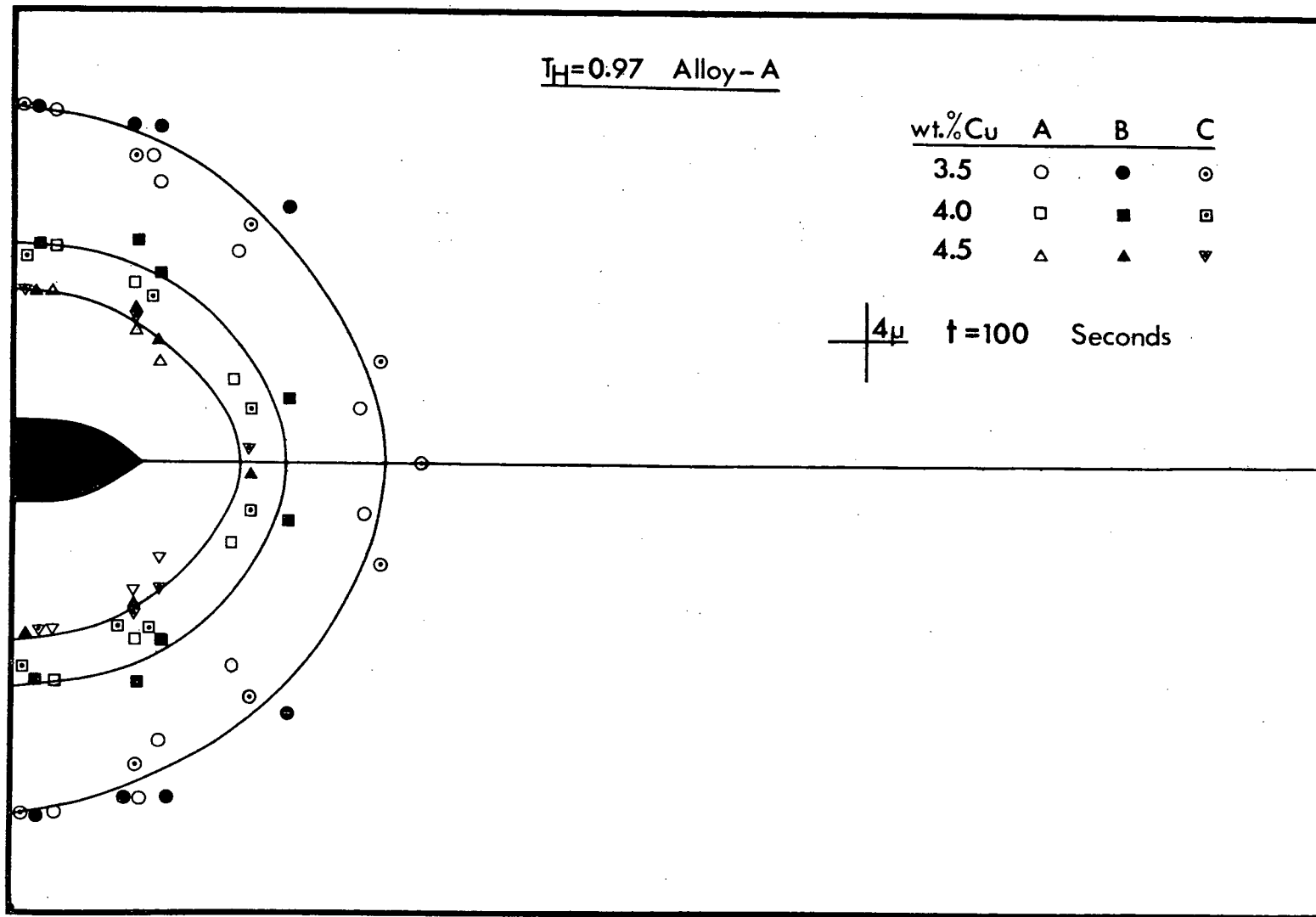


Figure 13. Dissolution isoconcentration contours of a grain boundary allotriomorph on the surface and 3μ below the surface (A and B) and a second allotriomorph in the bulk material (C). At $T_H = 0.97$ for alloy A.

surface diffusion effect. This also indicates that the effect of flux divergence is small relative to the experimental error, an observation that is important for the kinetic studies.

A further important question was whether impingement from adjacent diffusion fields just below the surface was affecting the measured results. To detect this possibility:

(1) A scan was obtained along the direction of the precipitate minor axis from the bulk matrix on one side to the bulk matrix on the other side.

(2) A parallel scan was also obtained just beyond the tips on either side of the precipitate continuing to a distance, on both sides of the grain boundary, associated with an equilibrium matrix composition.

The total diffusion field around the precipitate could then be examined, and any anomalies in the diffusion field became apparent.

2.7.2 Kinetic Measurements

Individual grain boundary precipitates were examined during dissolution. No statistical analysis of dissolution kinetics was carried out in the present work, as is generally done, because there were a relatively small number of precipitates on the grain boundaries, with a large range of precipitate shapes (S_0/R_0 varying from $> 10/1$ to $2/1$) (see Figure 14). With the small number of precipitates in any one specimen, the population distribution curves are inadequate for statistical analysis.

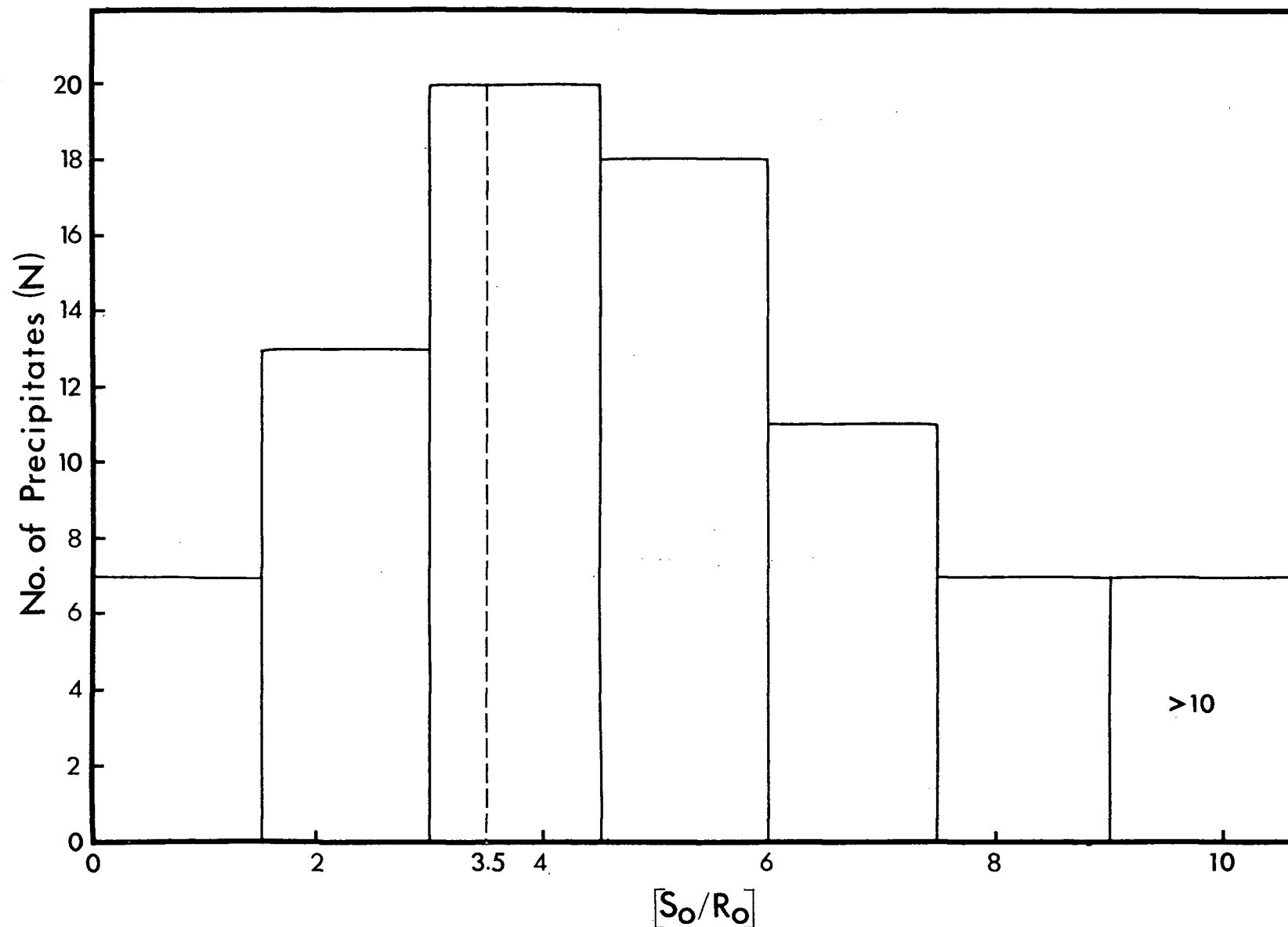


Figure 14. Population distribution curve for allotriomorphs of varying axial ratio S_0/R_0 for alloy A.

To determine if surface diffusion increased the dissolution rate in the kinetic studies, four grain boundary allotriomorphs were examined after a 12 minute dissolution treatment at 527°C. This dissolution heat treatment resulted in a decrease in the initial half-thickness R_0 of about 40%. The precipitate size was observed using the back-scattered electron image. A very thin surface layer was removed, the specimen was etched with a 5% NaOH solution, and the precipitate measurements were taken again optically. For all four precipitates the optical measurements were in good agreement with measurements obtained using the b.s.e.i., thus eliminating the possibility of surface diffusion contribution to the dissolution.

The use of the back-scattered electron image to measure the 'true' precipitate size was tested by measuring the precipitate size optically and comparing the results with those obtained by the b.s.e.i. and the absorbed electron image (a.e.i.). The absorbed electron image was found to be unreliable, as a change in contrast could give a drastically different precipitate size. The b.s.e.i., however, could be picked up at all settings without distorting the image. All the settings gave measurements of precipitate size equal to those obtained optically.

3. ISOCONCENTRATION CONTOUR RESULTS AND DISCUSSION

3.1 Introduction

Experimental determinations of the isoconcentration contours around dissolving grain boundary allotriomorphs, in an effectively infinite matrix, will be presented and analyzed in this chapter. One anticipates that isoconcentration contours associated with dissolving grain boundary precipitates would be influenced by the following parameters:

- (1) Dissolution rate controlling mechanism, i.e., whether the dissolution process is diffusion controlled or interface reaction controlled.
- (2) The precipitate shape (S_0/R_0).
- (3) Homologous temperature T_H .
- (4) The supersaturation (k) of the alloy.
- (5) The volume diffusion coefficient (D_V) of the alloy.
- (6) The grain boundary misorientation (R) and the grain boundary diffusion coefficient $D_{g.b.}$.

These parameters have each been considered experimentally. The results are presented, following a discussion of:

- (a) The diffusion couple results, to establish whether D_V is independent of composition in the α phase;

- (b) The microstructure of the equilibrated alloys, and
- (c) The nature of isoconcentration contours to establish the reproducibility of the technique used.

3.1.1 Diffusion Couple Results

The concentration profiles of dissolving precipitates are strongly dependent on the value of the volume diffusion coefficient of a given material. The analysis of the concentration profiles is greatly simplified if D_V can be considered as independent of alloy composition. To establish to what extent D_V is related to composition, composition measurements were made on a series of Al-CuAl₂ diffusion couples annealed at 480°C, 500°C, 520°C, and 535°C for 163 hours. The results for the 500°C diffusion couple are shown in Figures 15 and 16. In Figure 15 three runs are shown which are essentially coincident, indicating reproducible measurements. The anomalous rise in concentration near the interface is believed due to a two hour dissolution heat treatment at 535°C. This was done to dissolve CuAl₂ precipitates formed in the diffusion zone upon furnace cooling of the couple. Representative values of concentration from Figure 15 are plotted on probability paper, versus distance from the couple interface. The result shows a linear dependence, clearly indicating that D_V is independent of composition over the complete range of solid solution in the α phase, (see Figure 16). (The complete diffusion couple data is listed in Appendix IV). The temperature dependence of D_V from the present results is shown in an Arrhenius plot in Figure 17, along with values of D_V for an Al-0.5 wt.% Cu alloy published by Murphy.³⁹

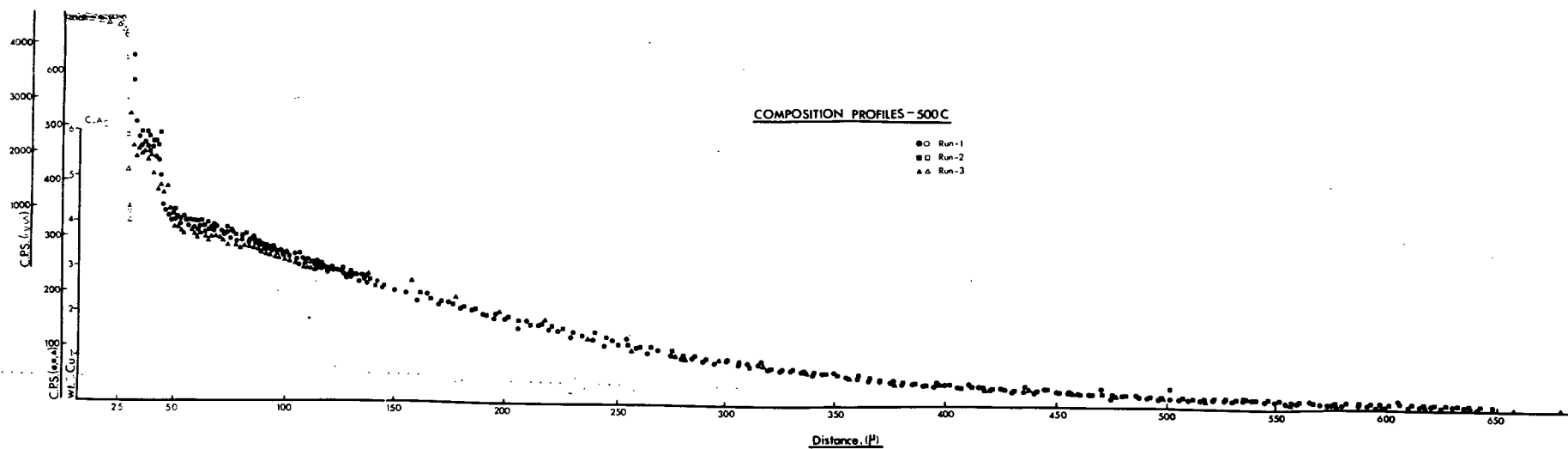


Figure 15. Composition contour for Al-CuAl₂ diffusion couple at 500°C.

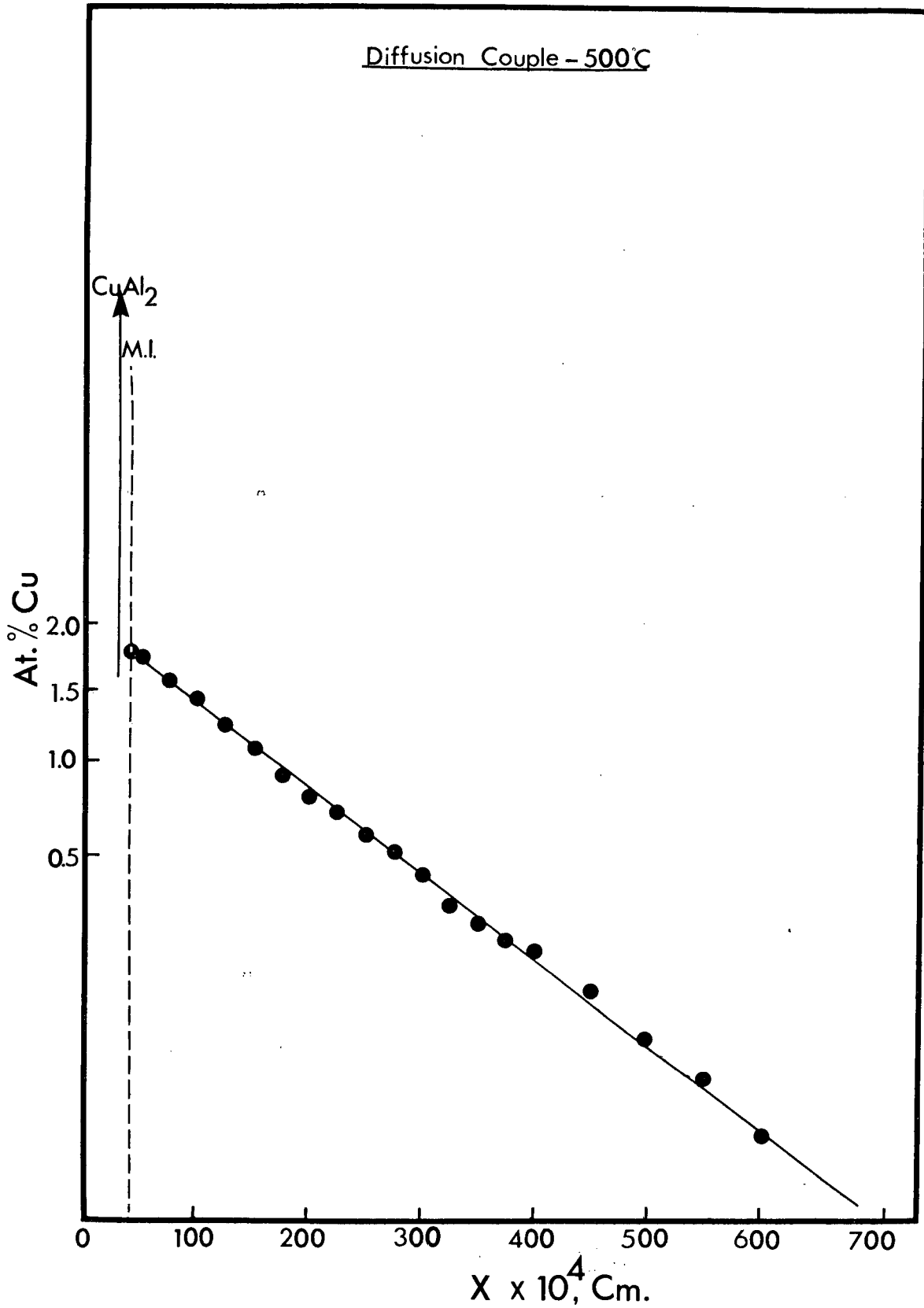


Figure 16. Probability plot of atomic % Cu versus diffusion distance (x) over the solid solubility range of the α phase for the 500°C diffusion couple.

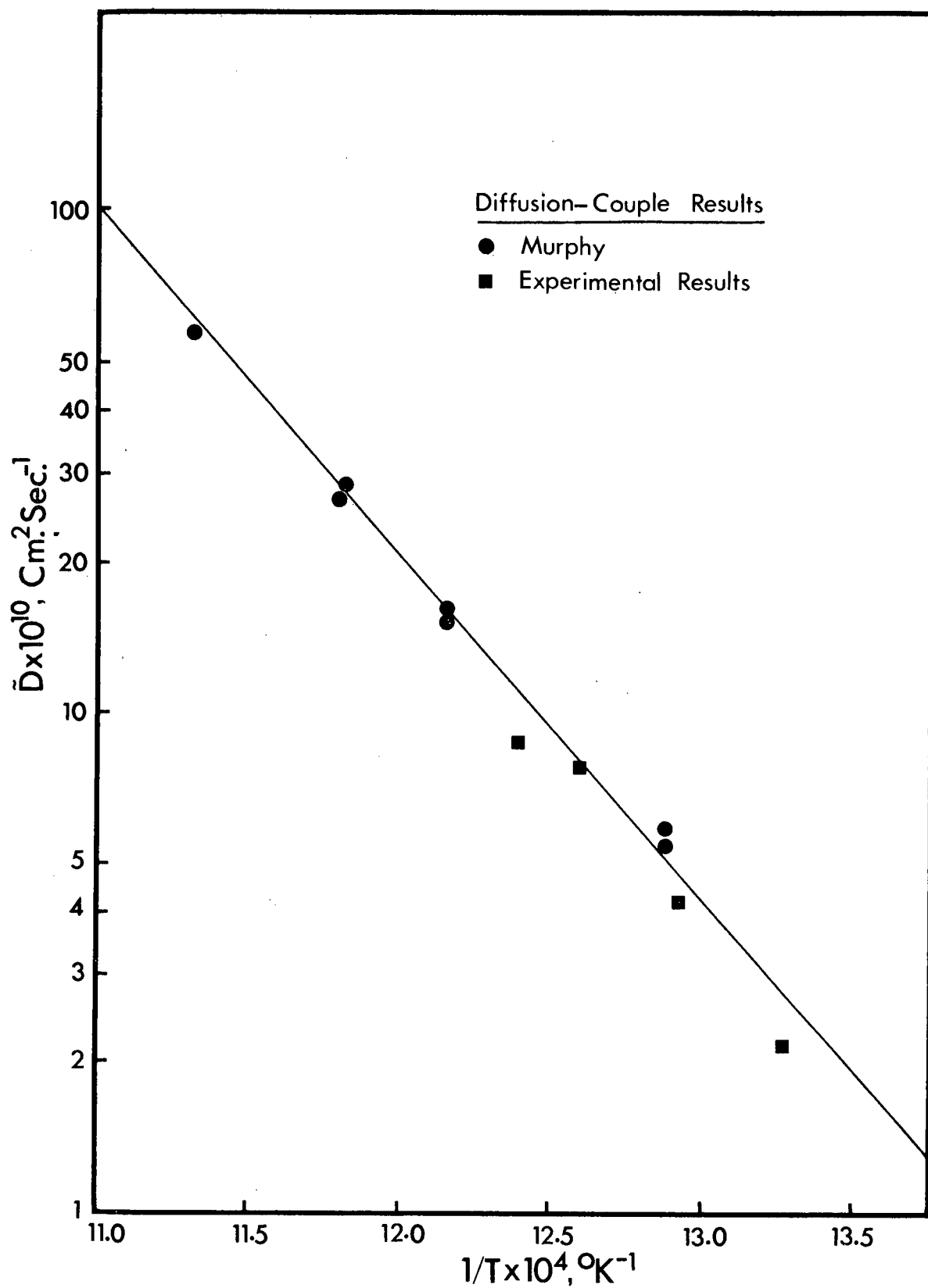


Figure 17. Arrhenius plot of D_V versus $1/T^\circ\text{K}^{-1}$ for the diffusion couple results.

The present results are observed to follow an Arrhenius plot and agree closely with the values of Murphy. Since the results reported by Murphy were obtained for a wider temperature range than in the present case, his values of D_V will be used in the analysis of the present results.

Grain boundary diffusion coefficients could not be determined, as the pressure applied to achieve bonding caused a certain amount of recrystallization in the bi-crystal.

3.1.2 The Microstructure of Equilibrated Alloys

The shape of typical grain boundary allotriomorphs in this investigation can be observed in Figure 6 (on page 26) which is a representative micrograph of alloy B. The precipitate shape is taken as oblate spheroidal and is defined by the length to width ratio S_0/R_0 . The grain boundary allotriomorphs are widely spaced with $3 < S_0/R_0 < 6$. A number of "snakes" of high axial ratio are also observed in the micrographs, which are believed to result from the impingement of two or more adjacent allotriomorphs.

Widmanstätten plates can be observed, however, they are not present in the areas immediately adjacent to the grain boundaries. The presence of a precipitate-free zone adjacent to the grain boundaries is a result of the depletion of vacancies in this area by the grain boundary precipitates which form first. The vacancy concentration is as a result too low for the nucleation of a second phase.^{40,41}

The size distribution (S_o) of the grain boundary precipitates obtained in Alloy A is plotted in Figure 18 as a function of the axial ratio (S_o/R_o) for the precipitate distribution plotted in Figure 14. The average allotriomorph size and the width of the depleted zone is shown in Table III, for the different alloy compositions studied.

Table III. Average S_o for Allotriomorphs with $S_o/R_o = 3.5$ and Average Width of Precipitate Free Zone for the Different Alloys.

Alloy	Half length of allotriomorphs(S_o) μ	Width of Precipitate free zone μ
A	25	90
B	15	70
C	10	60
D	10	30

3.1.3 Dissolution Isoconcentration Contours

Five separate grain boundary allotriomorphs were examined by electron probe microanalysis and concentration contours determined for both sides of each precipitate. The results are shown in Figure 19. (One side of one precipitate was not used because of early impingement from an adjacent allotriomorph.) The top half of the figure shows dissolution contours after 90 seconds from the start of dissolution, the bottom after 360 seconds. The five allotriomorphs were in an alloy B specimen (Al-2.81 wt.% Cu) which was homogenized at 400°C (T_G) and then upquenched to 520°C (T_D). The maximum solubility of Cu

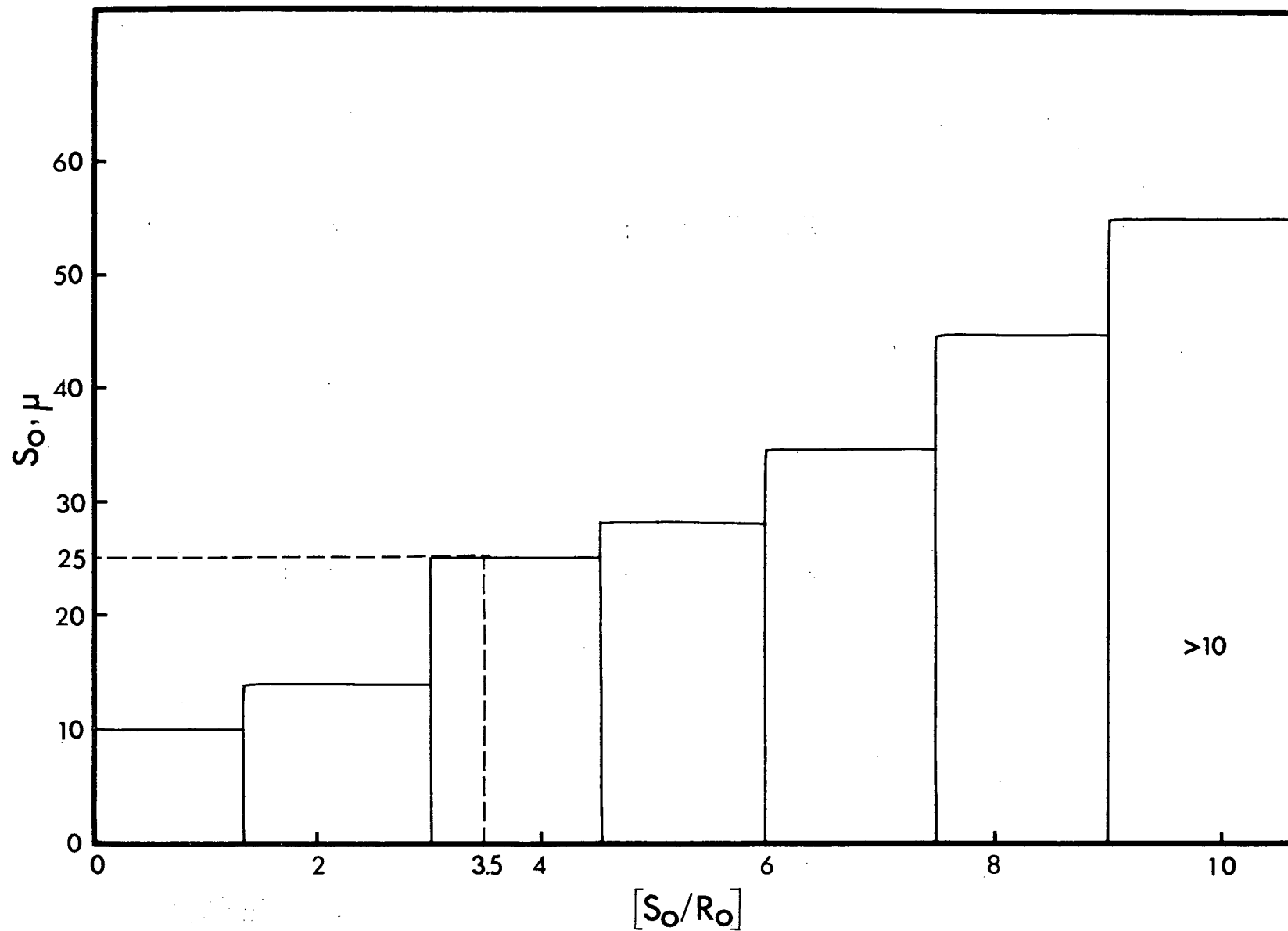


Figure 18. Size distribution (S_o) of precipitates as a function of S_o/R_o for alloy A.

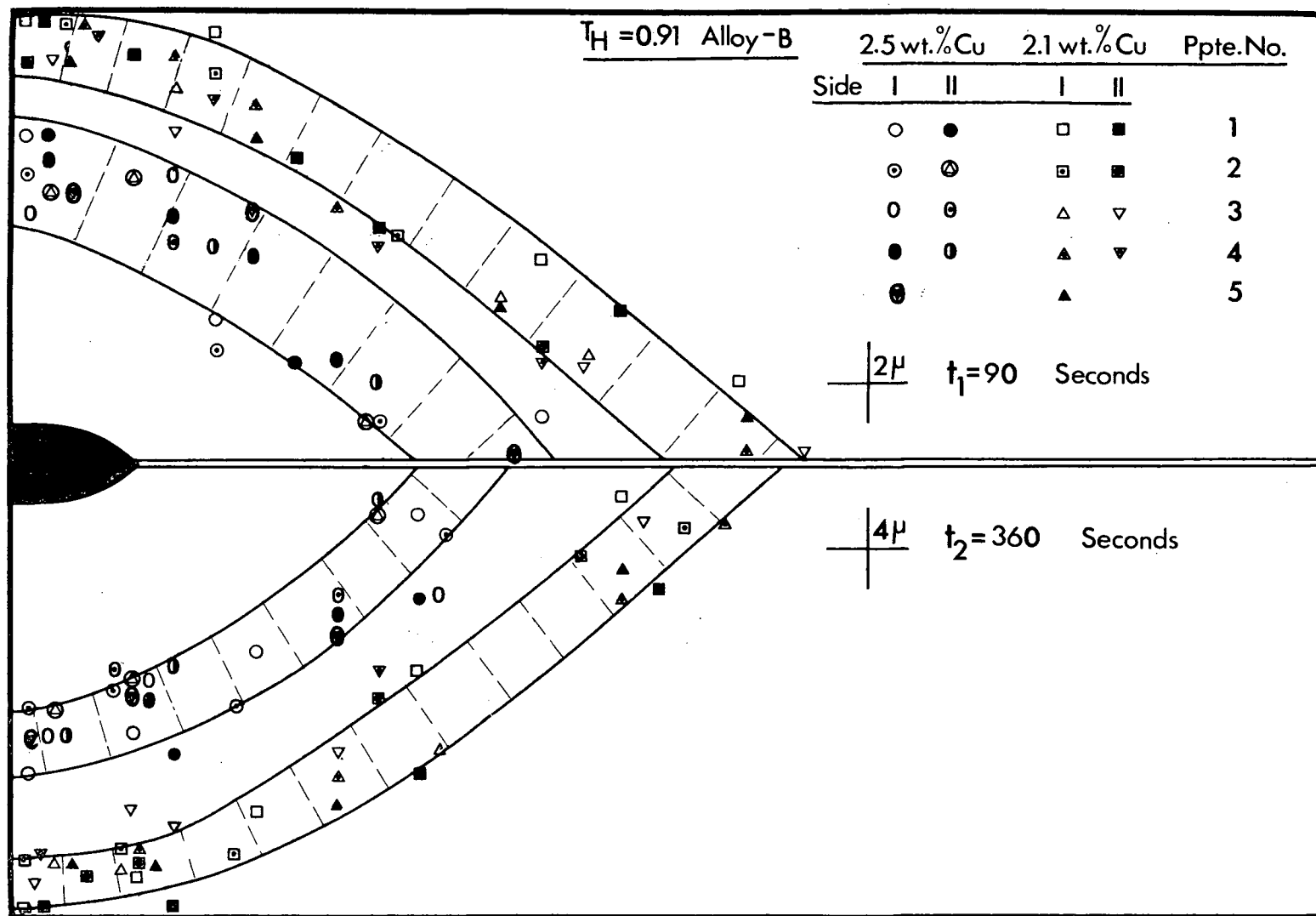


Figure 19. Isoconcentration contours at $T_H = 0.91$ for alloy B.

at 400°C in α is 1.9 wt.%; at 520°C it is 5.2 wt.%. Accordingly the precipitates will dissolve on upquenching until they ultimately disappear. The concentration measurements were confined to the early part of the dissolution process to avoid interaction effects due to solute fields from adjacent allotriomorphs. All composition measurements were made on scans perpendicular to the allotriomorph equatorial axis and grain boundary. In general, concentration measurements could not be made at distances less than 6 μ from the CuAl_2 precipitate, since within this distance Cu in the precipitate could contribute to the measured concentration.

In Figure 19 two values of concentration are plotted, 2.1 and 2.5 wt.% Cu. Higher values of concentration occurred within 6 μ of the precipitate surface and were therefore considered unreliable. Lower values were approaching the matrix composition (1.9 wt.% Cu), thus making composition differences comparable to the experimental uncertainty of the measurements. Examining the values of concentration plotted in Figure 19, it is observed that the position of points from sides I and II of a given precipitate are in close proximity indicating a high degree of symmetry of the isoconcentration contours about a given precipitate. However, points of equal concentration for the five precipitates are not in exact coincidence, as might be expected. The points for 2.5 wt.% Cu can essentially be enclosed in an envelope, shown by the two solid lines closest to the precipitate. The 2.1 wt.% Cu points are contained in the envelope furthest from the precipitate. To a first approximation, lines drawn through the centre of each zone can be taken as the isoconcentration contours for

the composition being considered. The standard deviation (σ) for these profiles varies from 0.68μ at a mean distance (\bar{x}) of 6.11μ from the precipitate interface, to a standard deviation (σ) of 1.17μ at a mean distance (\bar{x}) of 17.59μ from the precipitate interface. (See Appendix V for calculations). In the first case σ is 11.12% of the mean distance \bar{x} whereas in the second case σ is only 6.6% of the mean distance (\bar{x})(calculations in Appendix V). For the evaluation of D_V and C_I values, the longer time dissolution experiments with diffusion distance greater than 20μ from the interface were used, wherever possible, to minimize the effect of scatter just established as inherent in this experimental procedure.

3.2 Rate Controlling Mechanism

To establish that the dissolution process is diffusion controlled, values of concentrations at various time intervals were plotted as a function of x/\sqrt{t} , where x is the distance along the minor axis of the precipitate starting at the precipitate surface, and t is the time. The average result for two precipitates in the Al-4.83 wt.% Cu alloy at a dissolution temperature of 545°C ($T_H = 0.97$) is shown in Figure 20. The points are observed to be effectively coincident, indicating that the composition $C(x,t) = f\left(\frac{x}{\sqrt{Dt}}\right)$. The profile obtained extrapolates at $\frac{x}{\sqrt{t}} = 0$, to an interface concentration $C_I = 5.5$. This is in good agreement with the phase diagram indicating local equilibrium at the interface and therefore no interface reaction control. A similar analysis of data for the range of homologous temperatures between $T_H = 0.72$ and 0.97 gave similar results for diffusion distances

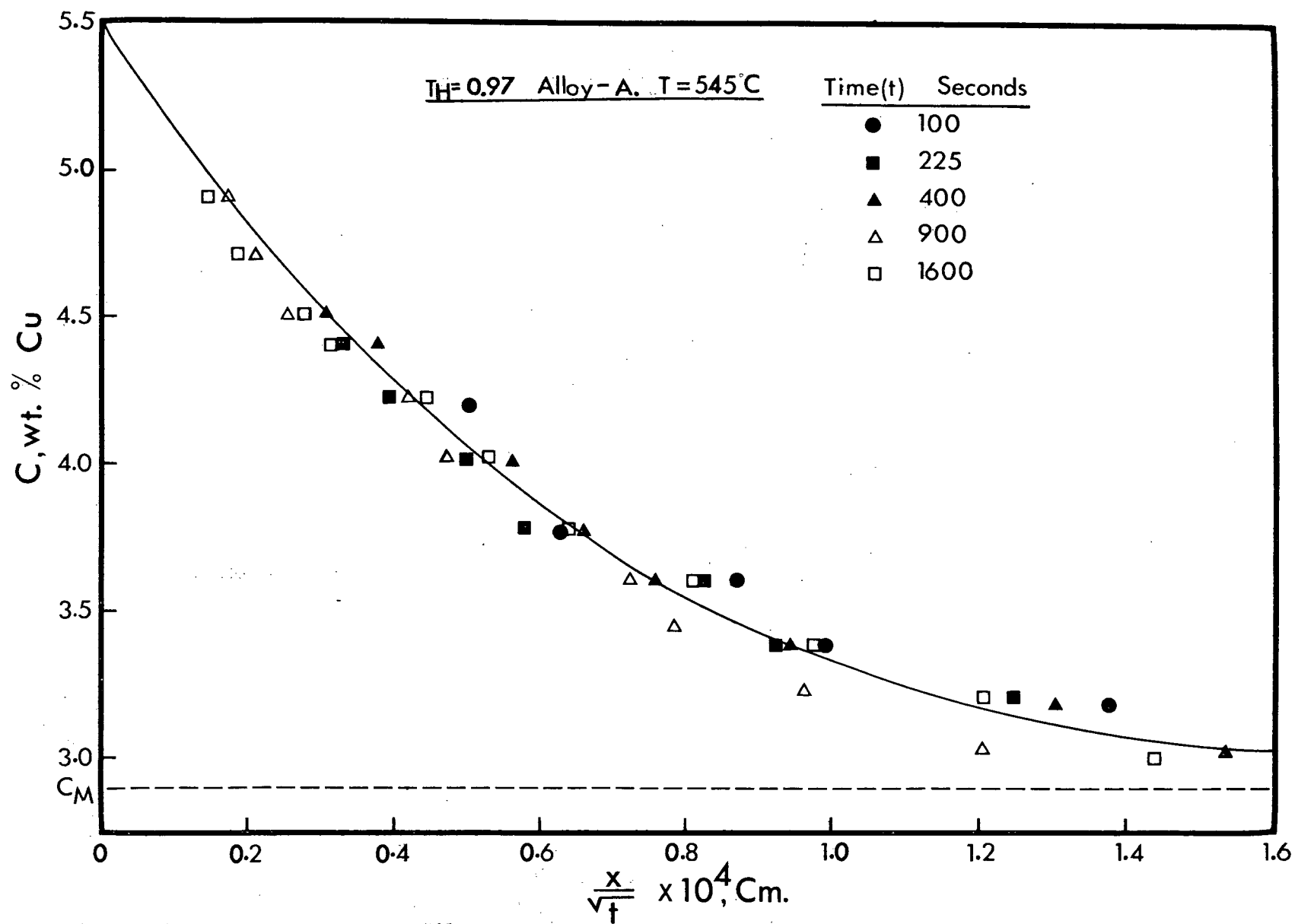


Figure 20. Concentration profile along the minor axis of a grain boundary allotriomorph at 545°C for alloy A.

along the minor axis of the allotriomorphs.

3.3 The Effect of the Precipitate Shape (S_o/R_o)

To determine the effect of precipitate shape on the concentration contours, three precipitates were examined with different axial ratios: (1) a typical allotriomorph with $S_o/R_o = 3.5$, (2) a snake with $S_o/R_o = 18$ and (3) a nearly spherical precipitate having $S_o/R_o = 1.7$. The resultant concentration contours are shown in Figure 21 for concentrations of 3.25 and 3.50 wt.% Cu and dissolution times of 30 and 120 seconds. The dissolution temperature was the same for all three precipitates. The results shown in Figure 21 clearly indicate that the composition contours for the three precipitates are essentially coincident, and therefore that under these experimental conditions the distance from the precipitate surface of the isoconcentration contours is independent of the axial ratio. This is not meant to imply that the overall shape of isoconcentration contours about a sphere and a snake are the same, as may be misconstrued from Figure 21. It should be pointed out that in Figure 21 as in all the figures of isoconcentration contours the points at the extreme left hand side denote average diffusion distances from the interface at the precipitate centre. The isoconcentration contours attempt to give an accurate representation of the isoconcentration lines, about the tip of an allotriomorph, and along the adjacent grain boundary, with only an average diffusional distance away from the broad allotriomorph faces.

In general, two effects have to be considered for dissolution of precipitates of different axial ratios: (a) the Gibbs-Thomson effect

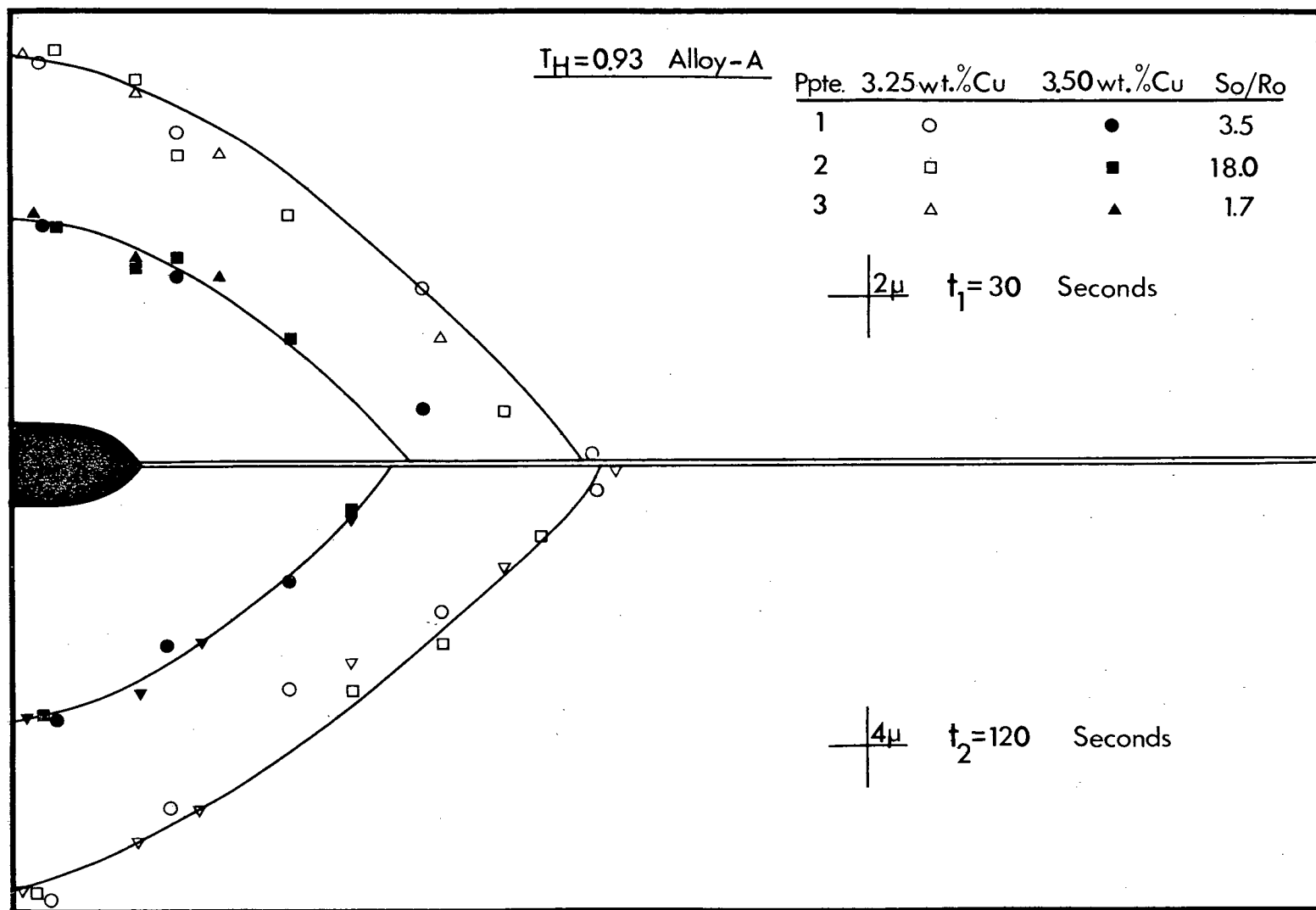


Figure 21. Isoconcentration contours for three allotriomorphs having axial ratios S_o/R_o of 1) 3.5, 2) 18, 3) 1.7 for alloy A at $T_H = 0.93$.

and (b) the point effect of diffusion.

(a) The Gibbs-Thomson effect is the variation with curvature of the equilibrium solute concentration at the precipitate-matrix interface. Aaron and Kotler⁴² have calculated the influence of this effect on the dissolution kinetics of Al-Cu alloys and conclude that it is negligible for the total dissolution time of a precipitate. Therefore the influence of interface curvature on the isoconcentration contours is expected to be minimal.

(b) Because of the point effect of diffusion, the flux from the tip of an allotriomorph is distributed over a greater solid angle than the flux perpendicular to the side of an allotriomorph. Thus the point effect tends to round off the isoconcentration contours at the tip of an allotriomorph.

As a further verification that the Gibbs-Thomson effect does not influence the position of the isoconcentration curves around a dissolving precipitate for short dissolution times, concentration measurements were made around two Widmanstätten plates located in the centre of a grain under the same conditions as those for Figure 21. The average results are shown in Figure 22 and show comparable diffusion distances, along the minor axis, to those for the grain boundary allotriomorphs in Figure 21.

Hence, the shape of the precipitate does not influence the position of the isoconcentration curve relative to the precipitate surface. In addition, Widmanstätten plates, like grain boundary allotriomorphs, are found to dissolve by a diffusion mechanism in agreement with the results of Hall and Hayworth³¹ in an Al-5 wt.% Cu alloy.

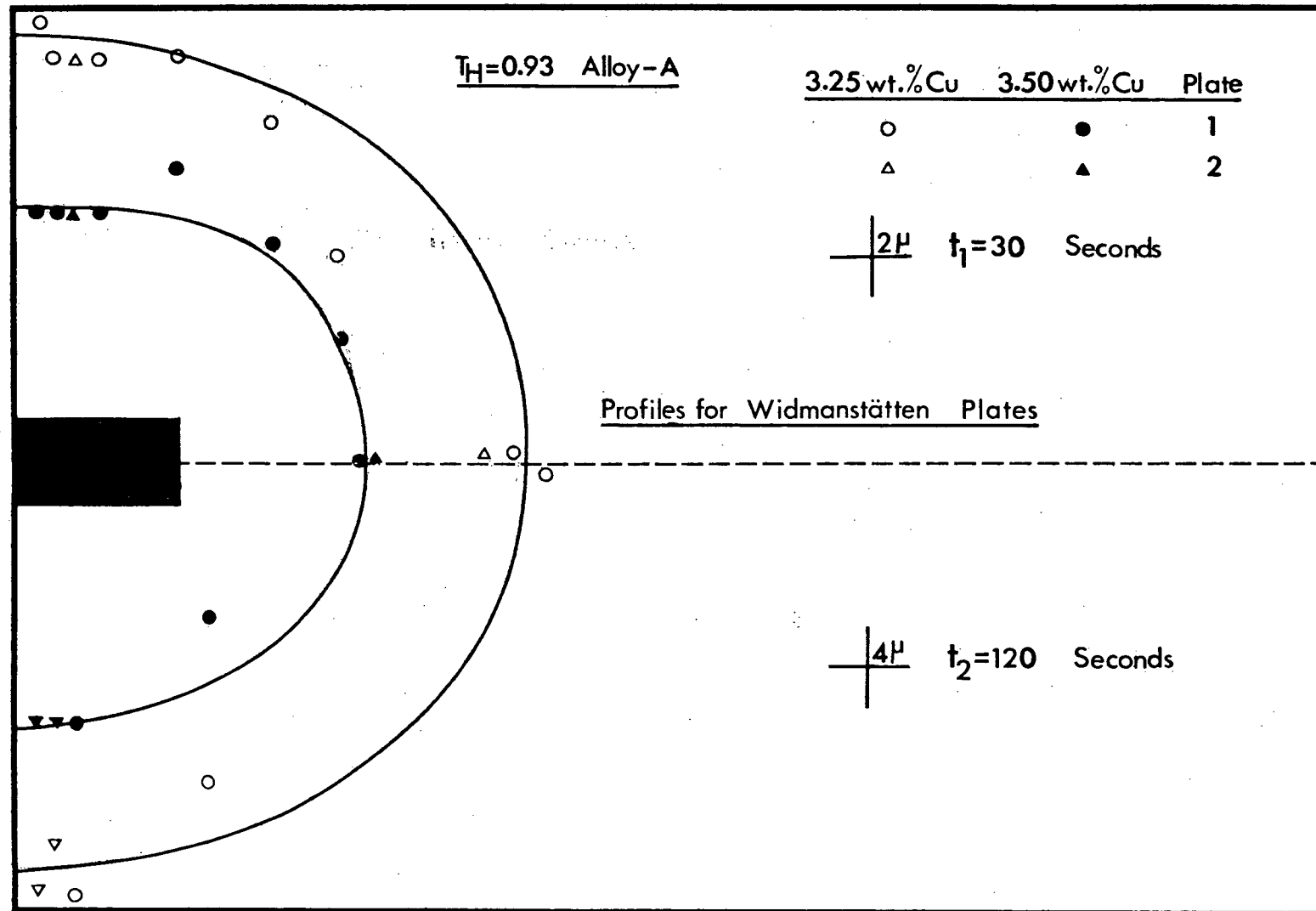


Figure 22. Isoconcentration contours of two Widmanstätten plates for alloy A at $T_H = 0.93$.

3.4 Homologous Temperature T_H

To determine the effect of T_H on the position and shape of the isoconcentration lines around an allotriomorph, concentration measurements were made on a series of alloys, over a range of dissolution times, for $0.72 \leq T_H \leq 0.97$. The specific experiments are tabulated in Table IV. Some of the corresponding concentration contours are given in Figures 23-29 for the times and concentrations indicated. No scatter bars have been placed on the contour plots; the scatter as established in Section 3.1.3 is expected to be the same for these results.

Comparing the isoconcentration contours for $T_H = 0.97$ (Figure 23) with $T_H = 0.77$ (Figure 29), it is observed that the isoconcentration lines in the former are inclined at approximately 90° to the grain boundary plane, whereas in the latter the corresponding angle is about 20° . The decreasing of the angle of inclination is clear evidence that enhanced grain boundary diffusion has occurred at the lower homologous temperature. Figures 23-29 show a progressive decrease in the angle of inclination with decreasing T_H and therefore a progressively greater contribution from grain boundary diffusion to the dissolution process. The contours for the highest homologous temperature $T_H = 0.97$ (Figure 23) exhibit essentially no grain boundary contribution to dissolution. The slight rounding-off of the contours at the precipitate tip is thought to be due to the point effect of diffusion.

At $T_H = 0.92$ there is a very small amount of grain boundary diffusion and the diffusion distance along the grain boundary at the tip of the precipitate is slightly greater than the diffusion distance

Table IV. Contour Experiments

T_H	alloy	No. of allotriomorphs	Dissolution times (seconds)	Figure No.
.97	A	2	25,100,225,400,900,1600	23
.94	B	1	400,900,1600	24
.93	A	5 [*]	30,120	21 and 22
.93	Al-Ag	3	40,160	43
.92	A	3 ^{**}	100,400,1600	34
.92	B	2	400,900,1600,3200	25
.91	B	9	90,360	19
.905	B	1	400,900,1600	26
.885	B	2	500,1600	45
.885	Al-Ag	2	50,100,200	42
.86	B	1	400,900,1600	27
.84	Al-Ag	3 ^{***}	70,150,225,400	35 and 36
.83	B	1	100,400,1600,6400	44
.80	C	1	1600,6400	28
.77	C	2	1600,3600,6400	29
.72	C	2	1600,3600	30

* 2 Widmanstätten plates, plus 3 different shape grain boundary precipitates.

** 1 precipitate only at 1600 seconds

*** 2 precipitates on low angle grain boundary

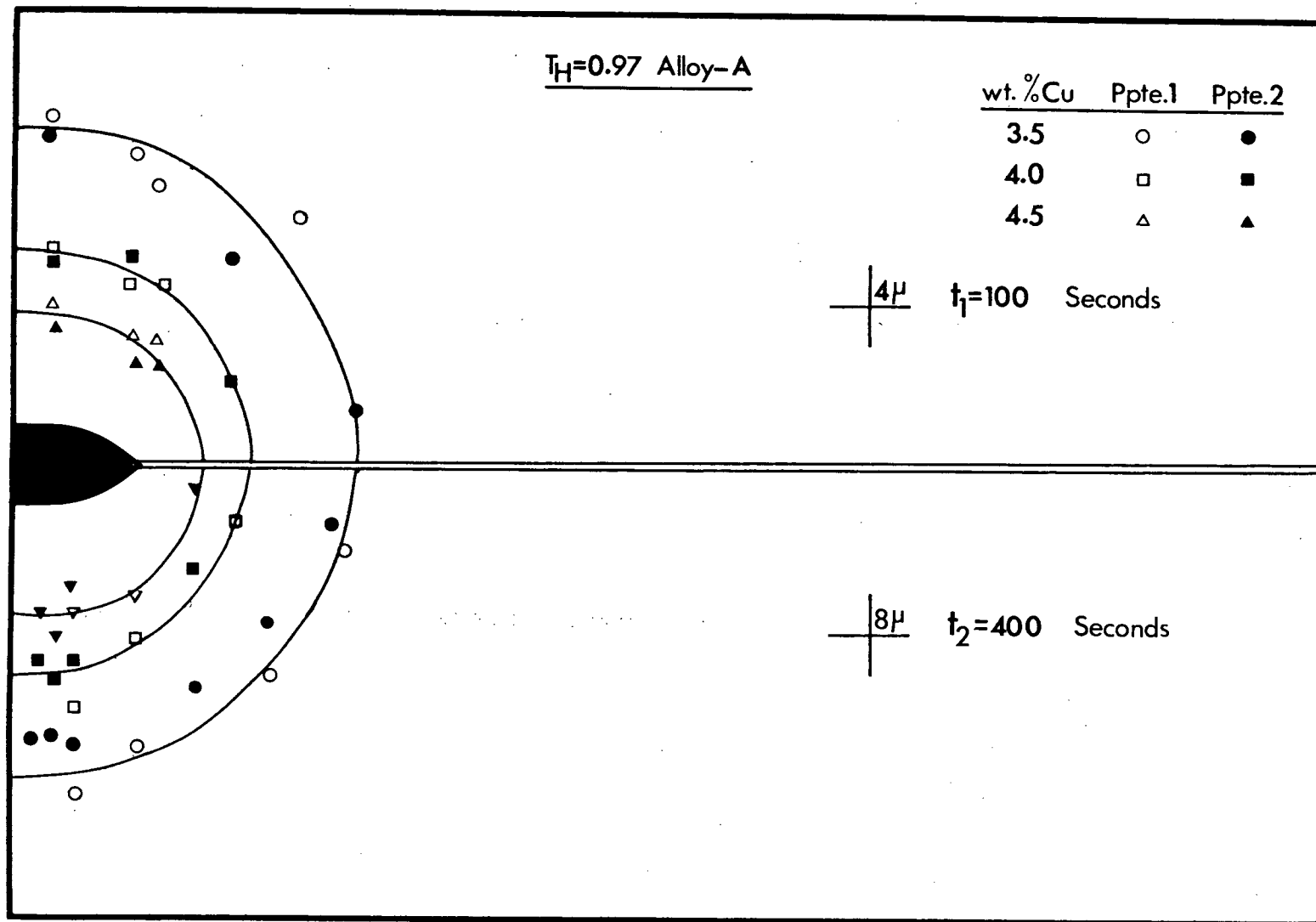


Figure 23. Isoconcentration contours for alloy A at $T_H = 0.97$.

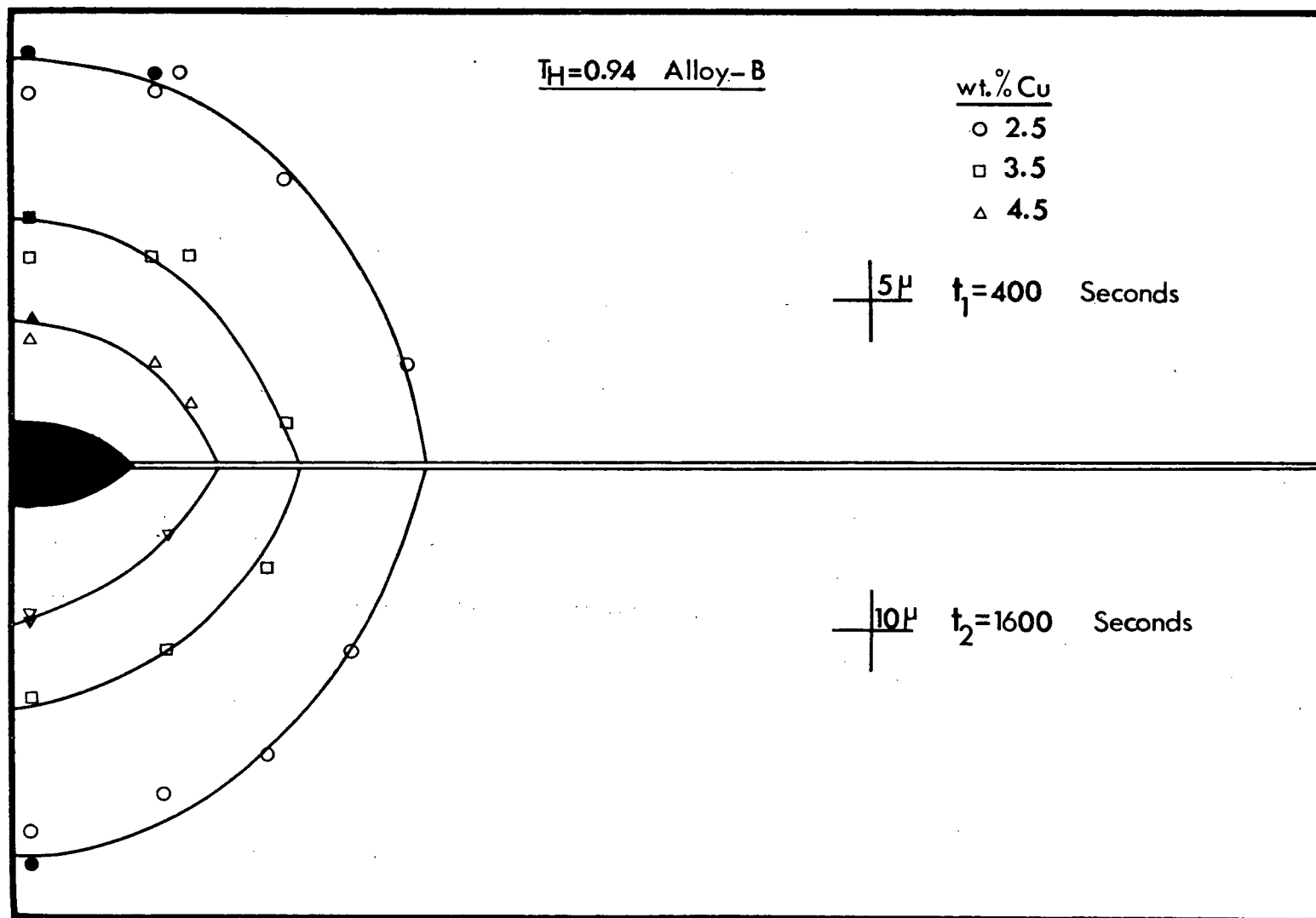


Figure 24. Isoconcentration contours for alloy B at $T_H = 0.94$.

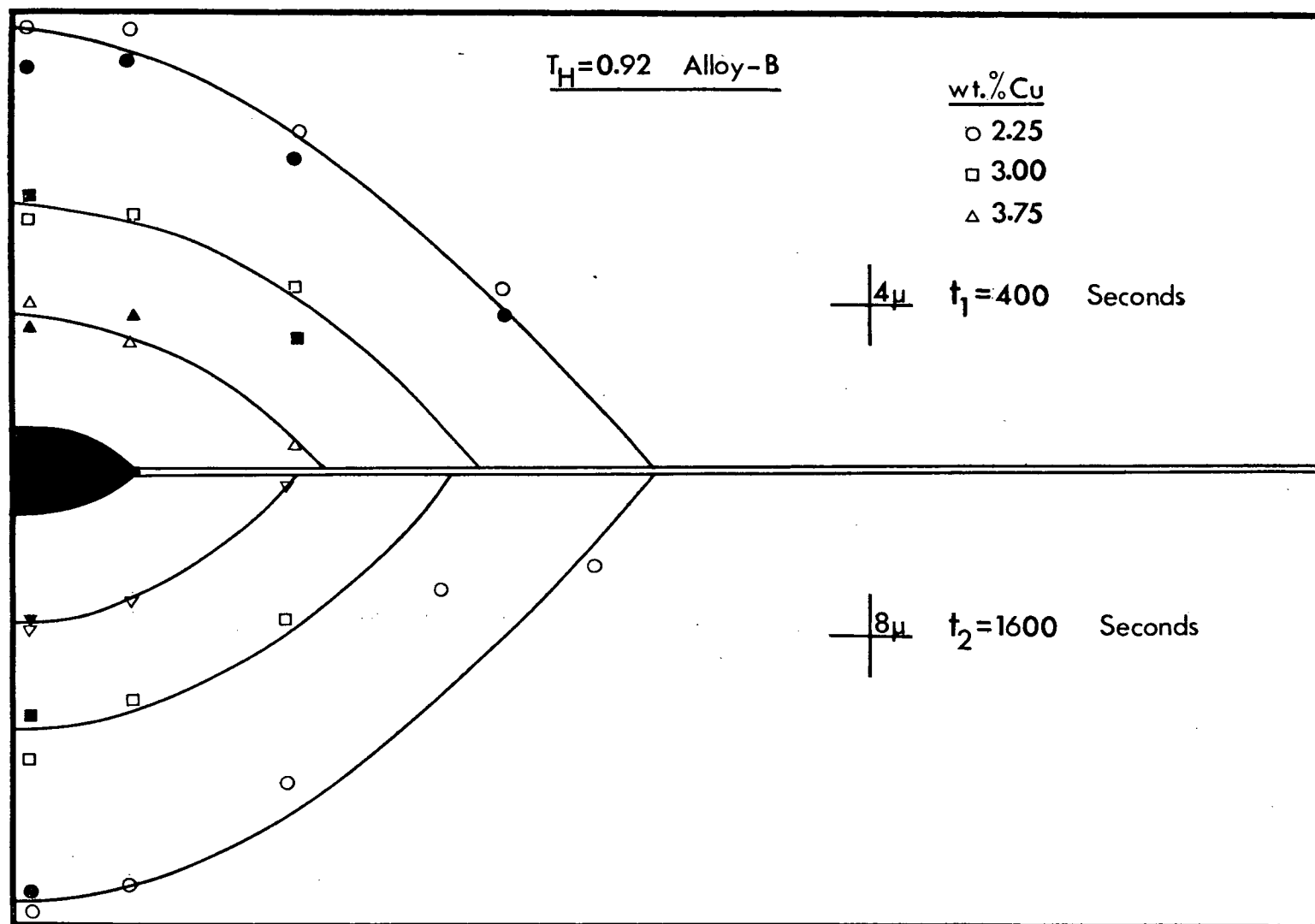


Figure 25. Isoconcentration contours for alloy B at $T_H = 0.92$.

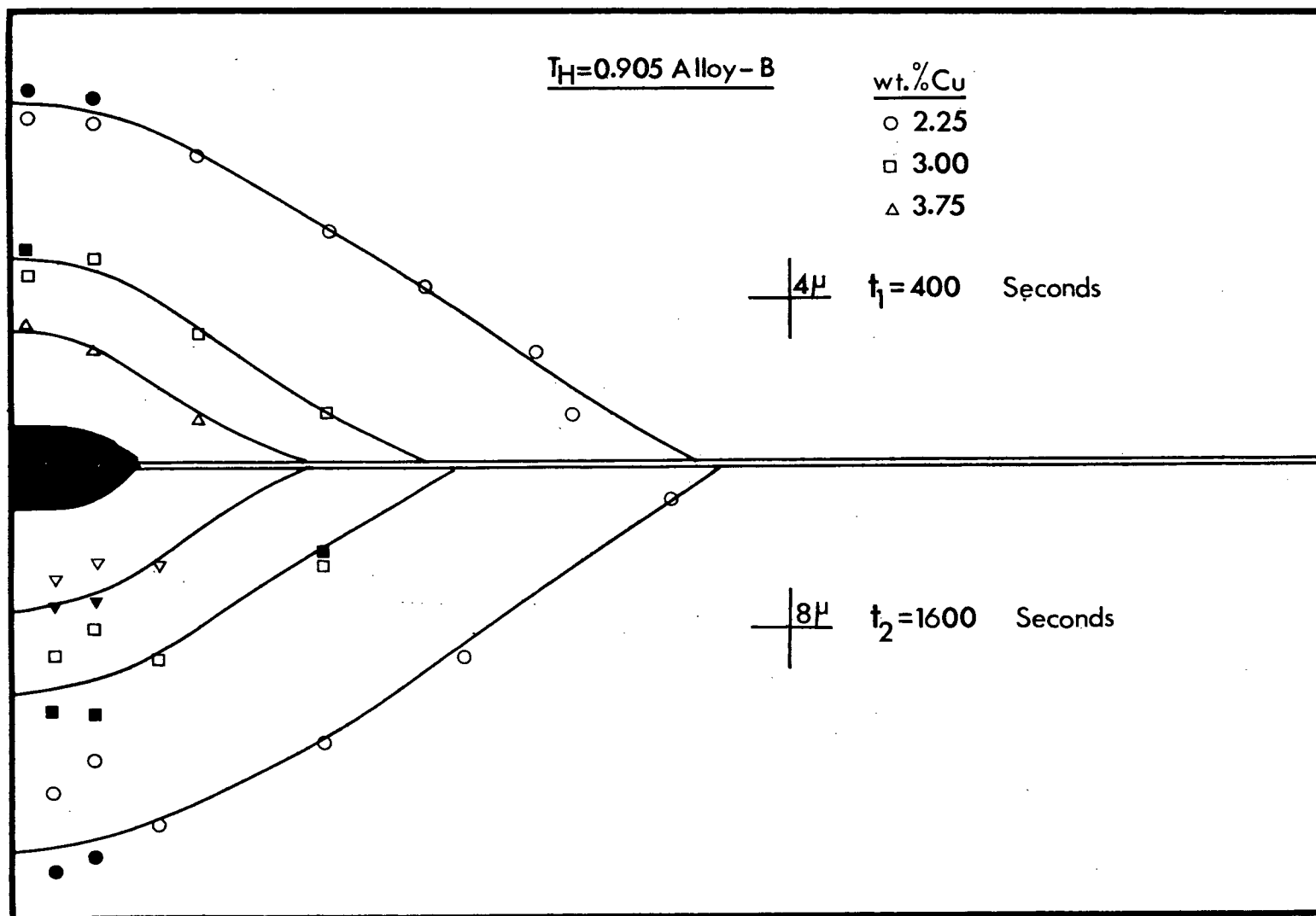


Figure 26. Isoconcentration contours for alloy B at $T_H = 0.905$.

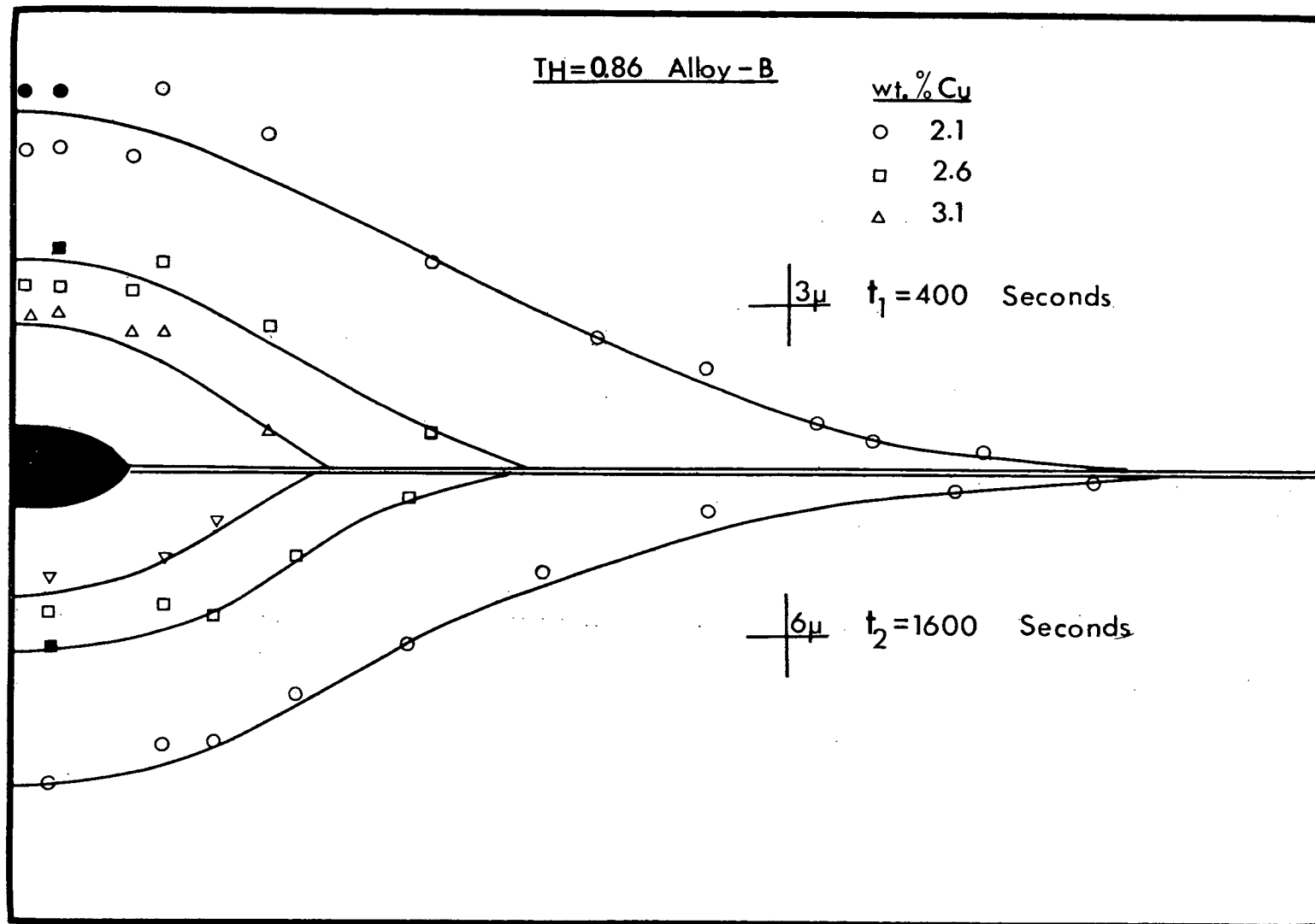


Figure 27. Isoconcentration contours for alloy B at $T_H = 0.86$.

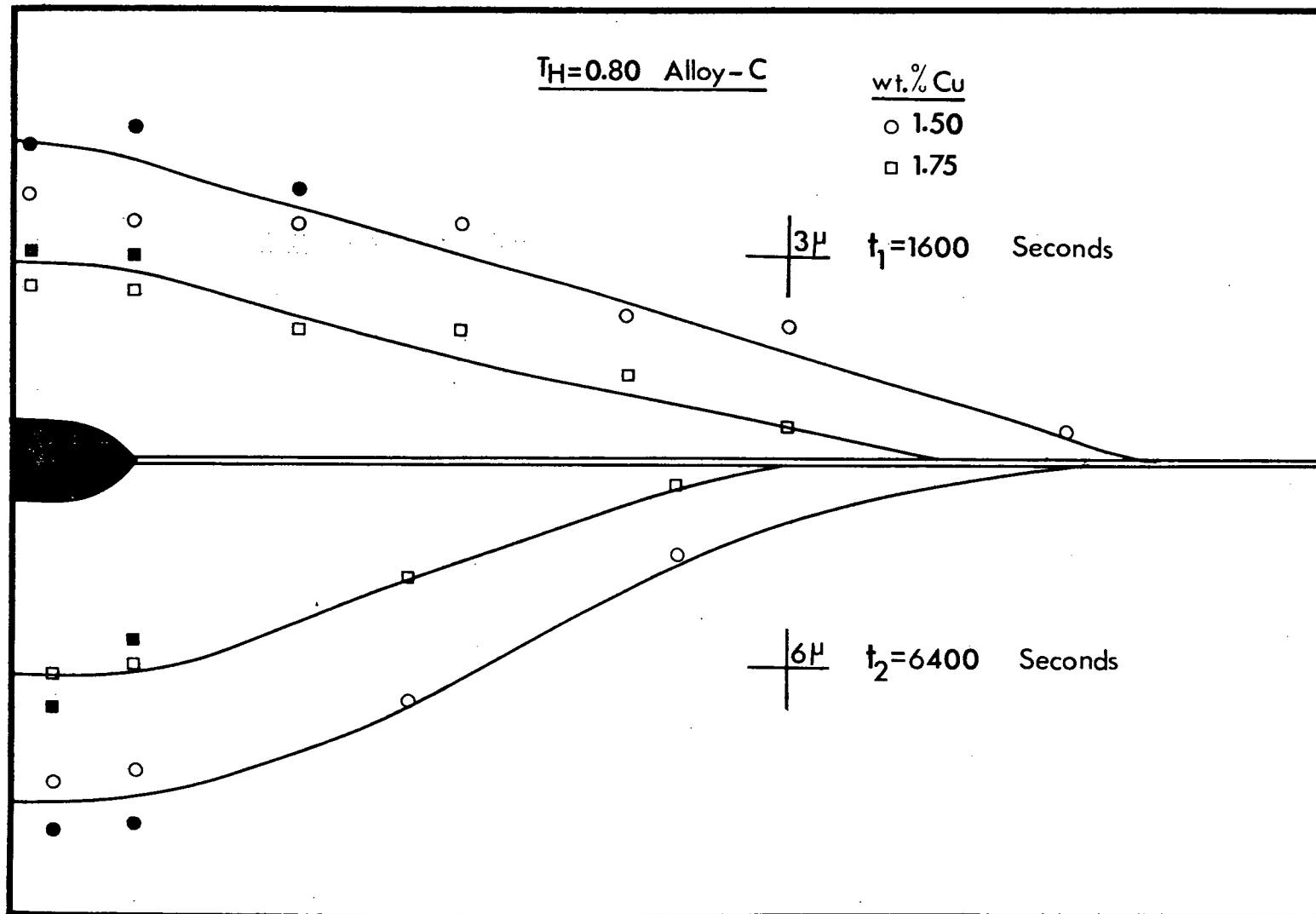


Figure 28. Isoconcentration contours for alloy C at $T_H = 0.80$.

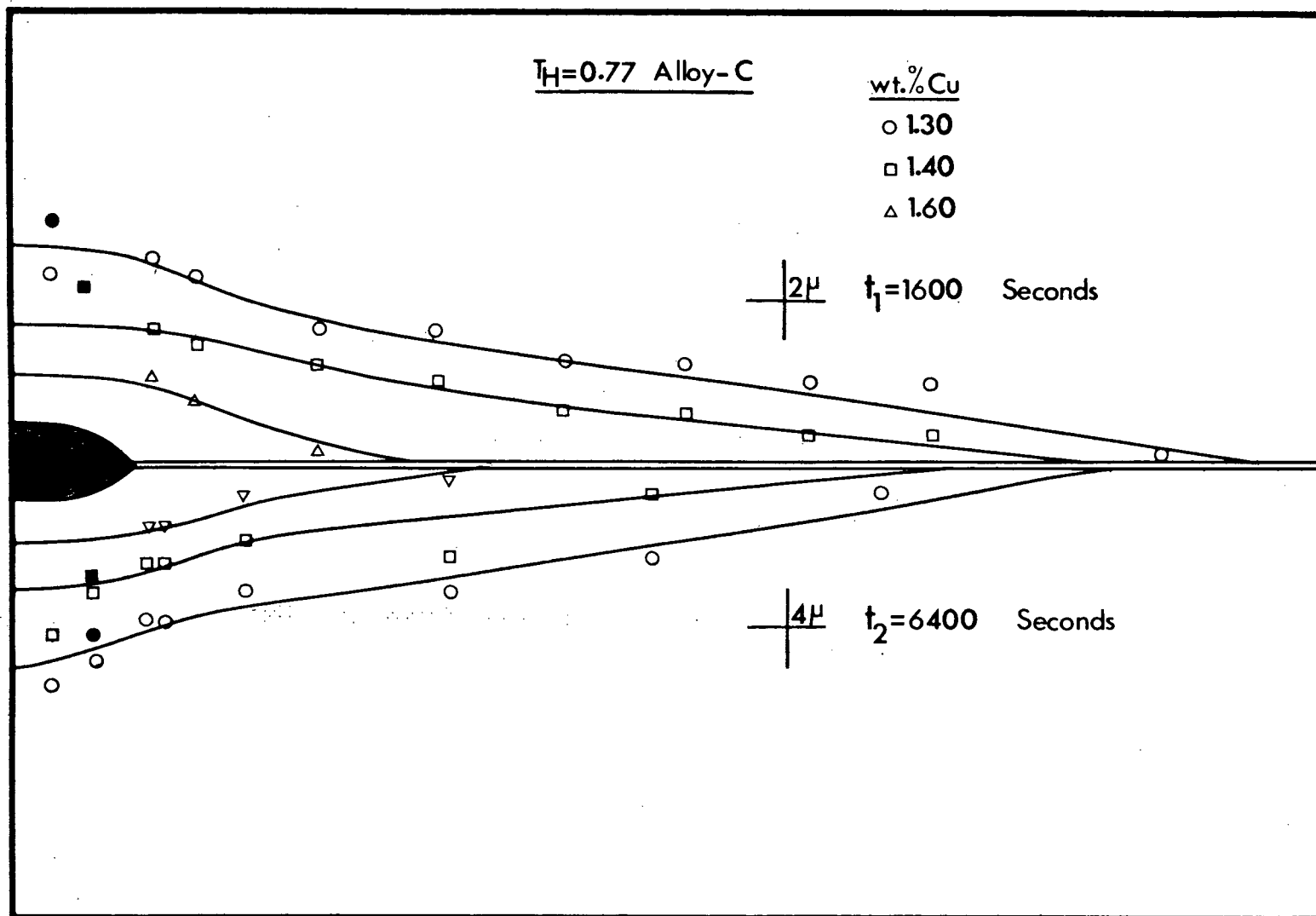


Figure 29. Isoconcentration contours for alloy C at $T_H = 0.77$.

perpendicular to its flat surface. As the homologous temperature decreases, this effect becomes more pronounced until at the lowest temperature studied $T_H = 0.72$ (Figure 30), the diffusion fields along the grain boundaries impinge with those of adjacent allotriomorphs before there is enough volume diffusion from the precipitate to be resolved by the electron probe.

The grain boundary diffusion contribution to growth was estimated experimentally using statistical techniques, by Goldman et al.²¹ Their results indicate that below $T_H = 0.78$ solute transport should be due solely to grain boundary diffusion. No experiments were done above $T_H = 0.78$. However, between $T_H = 0.79$ and 0.90, they postulate volume diffusion should become progressively more dominant, and above $T_H = 0.91$ they predict transport should be entirely by volume diffusion.

Hawbolt and Brown,⁶ in their studies of the growth of grain boundary allotriomorphs in Ag-5.64 wt.% Al, find that at $T_H = 0.92$, growth is entirely volume diffusion controlled. At $T_H = 0.90$, however, there is some evidence in their results for grain boundary diffusion enhancing the growth rate of precipitates. The present results show quite conclusively that volume diffusion completely dominates the dissolution process above a homologous temperature of between 0.92 and 0.93. It is further shown that at $T_H = 0.77$, the effect of volume diffusion on dissolution is negligible, and that there is essentially total grain boundary diffusion control at $T_H = 0.72$. Thus the present allotriomorph dissolution results are in excellent agreement with the work of both Goldman et al.²¹ and Hawbolt and Brown⁶

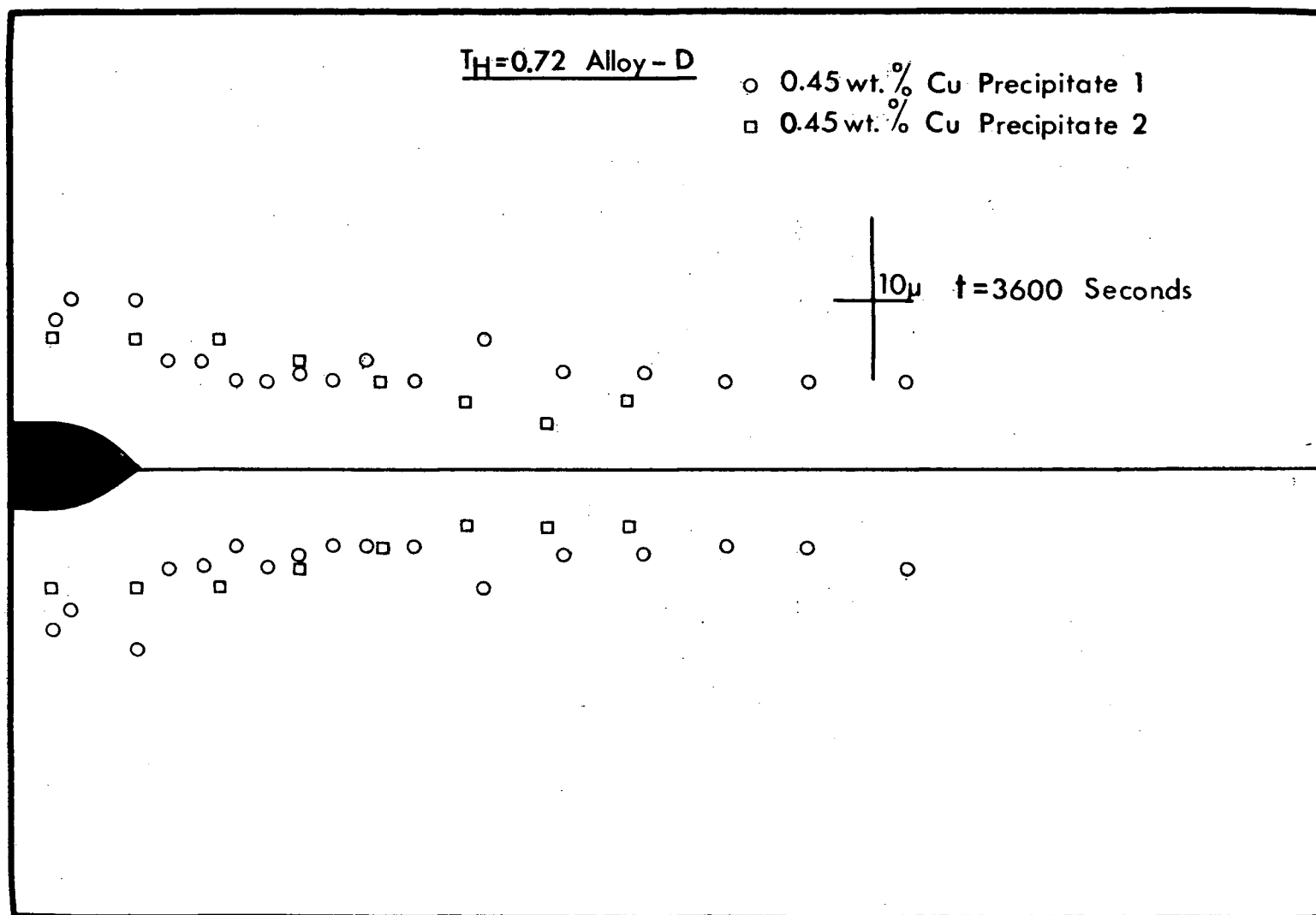


Figure 30. Isoconcentration contour for alloy D at $T_H = 0.72$.

regarding the transition from complete volume diffusion control to complete grain boundary diffusion control for the growth of allotriomorphs. The relative importance of volume diffusion to grain boundary diffusion, in the transition region between complete volume diffusion control and complete grain boundary diffusion control, is also well illustrated for the first time experimentally in these results. In the following section the volume diffusion coefficient D_V is calculated using the concentration profiles parallel to the minor axis of the grain boundary allotriomorph, where enhancement by grain boundary diffusion can be neglected. Values of C_I , the allotriomorph interface composition, are also determined.

3.4.1 Calculations of D_V and C_I

Evaluations of D_V and C_I are made to test the accuracy of the concentration contour experiments. The following assumptions were made in determining D_V and C_I .

(1) D_V is independent of concentration. This is based on the diffusion couple results (Section 3.1.1) which indicate that the volume diffusion coefficient is independent of concentration over the complete solid solubility range of the α -phase.

(2) The allotriomorph-matrix interface is essentially flat at the minor axis, so that a one-dimensional solution to the diffusion equation can be used with distances measured perpendicular to the centre of the flat surface of the allotriomorph. (Figure 20 indicates an error function profile in this direction).

(3) There is very little movement of the interface relative to

the diffusional distance. The precipitate interface is considered stationary relative to the diffusion distances considered during dissolution. A calculation for the prevailing experimental conditions, by Hall and Hayworth,³¹ indicates a diffusion distance which is approximately two orders of magnitude greater than the displacement of the interface.

Subject to these assumptions, the solution to Fick's law reduces to:

$$\frac{C_{(x,t)} - C_M}{C_I - C_M} = 1 - \operatorname{erf} \cdot \frac{x}{2\sqrt{D_V t}} \quad 1$$

C_I could not be measured experimentally due to the finite size of the electron beam in the electron probe, therefore, both C_I and D_V have unknown values in equation 1.

Values of D_V and C_I were obtained from equation 1 using the following graphical analysis.

(1) For three values of x ($x = 10 \mu, 15 \mu, 20 \mu$), the corresponding experimental values of $C_{(x,t)}$ were obtained from the iso-concentration lines in Figure 25 and were used in conjunction with a range of $(D_V t)^{1/2}$ values to solve equation 1. The graph of C_I vs. $(D_V t)^{1/2}$ (Figure 31) consists of three curves which cross at a point corresponding to approximate values of C_I and $(D_V t)^{1/2}$.

(2) A plot of $C_{(x,t)}$ versus $\operatorname{erf} \cdot \left[\frac{x}{2(D_V t)^{1/2}} \right]$ was made using the value of $(D_V t)^{1/2}$ obtained from Figure 31. This is a linear plot which is consistent with equation 1. When extrapolated to $\operatorname{erf} \cdot \left[\frac{x}{2(D_V t)^{1/2}} \right] = 0$ a more accurate value of C_I is obtained as shown

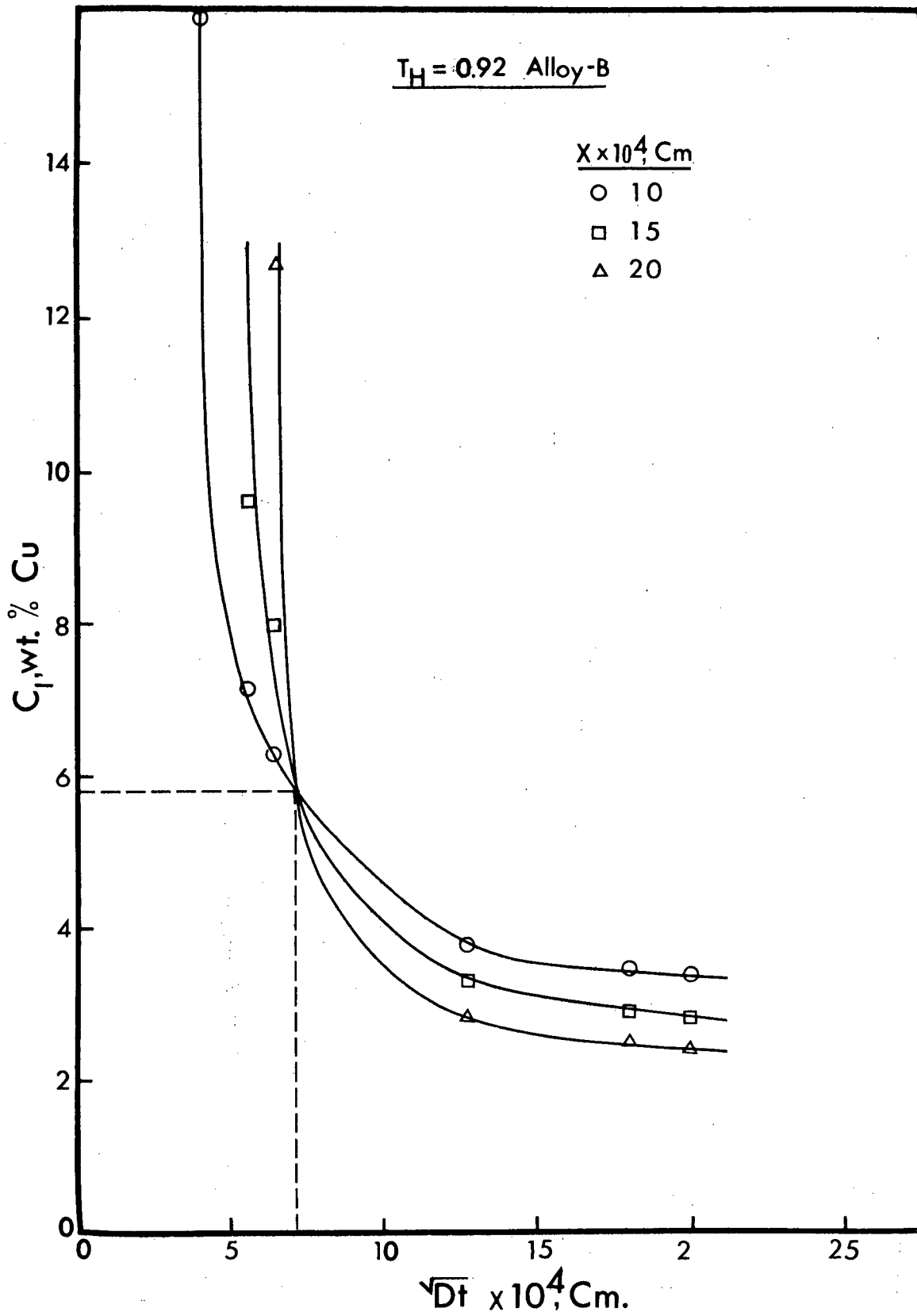


Figure 31. Interface concentration C_I versus \sqrt{Dt} for alloy B at $T_H = 0.92$.

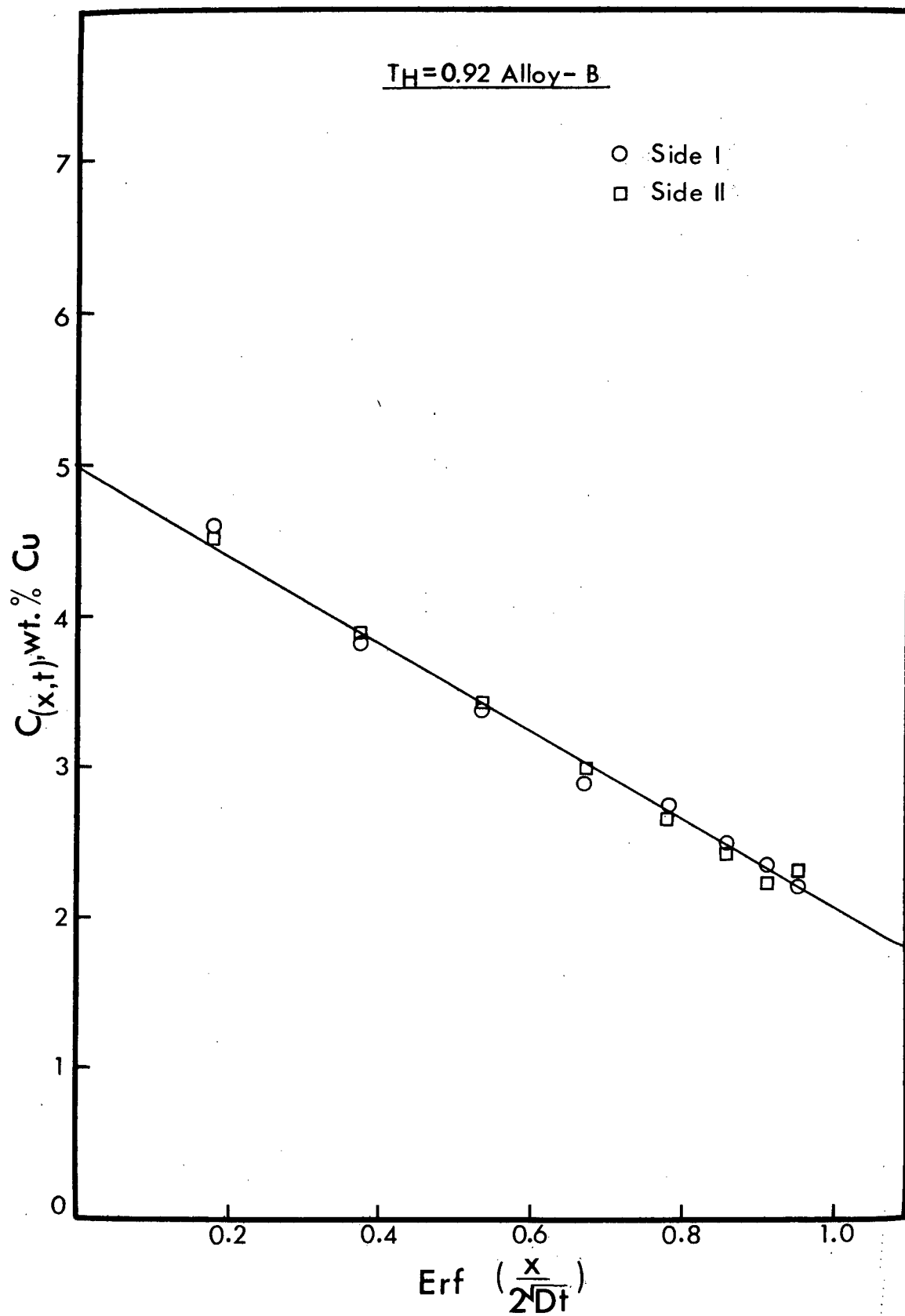


Figure 32. C versus $\text{erf} \left(\frac{x}{2\sqrt{Dt}} \right)$ for alloy B at $T_H = 0.92$.

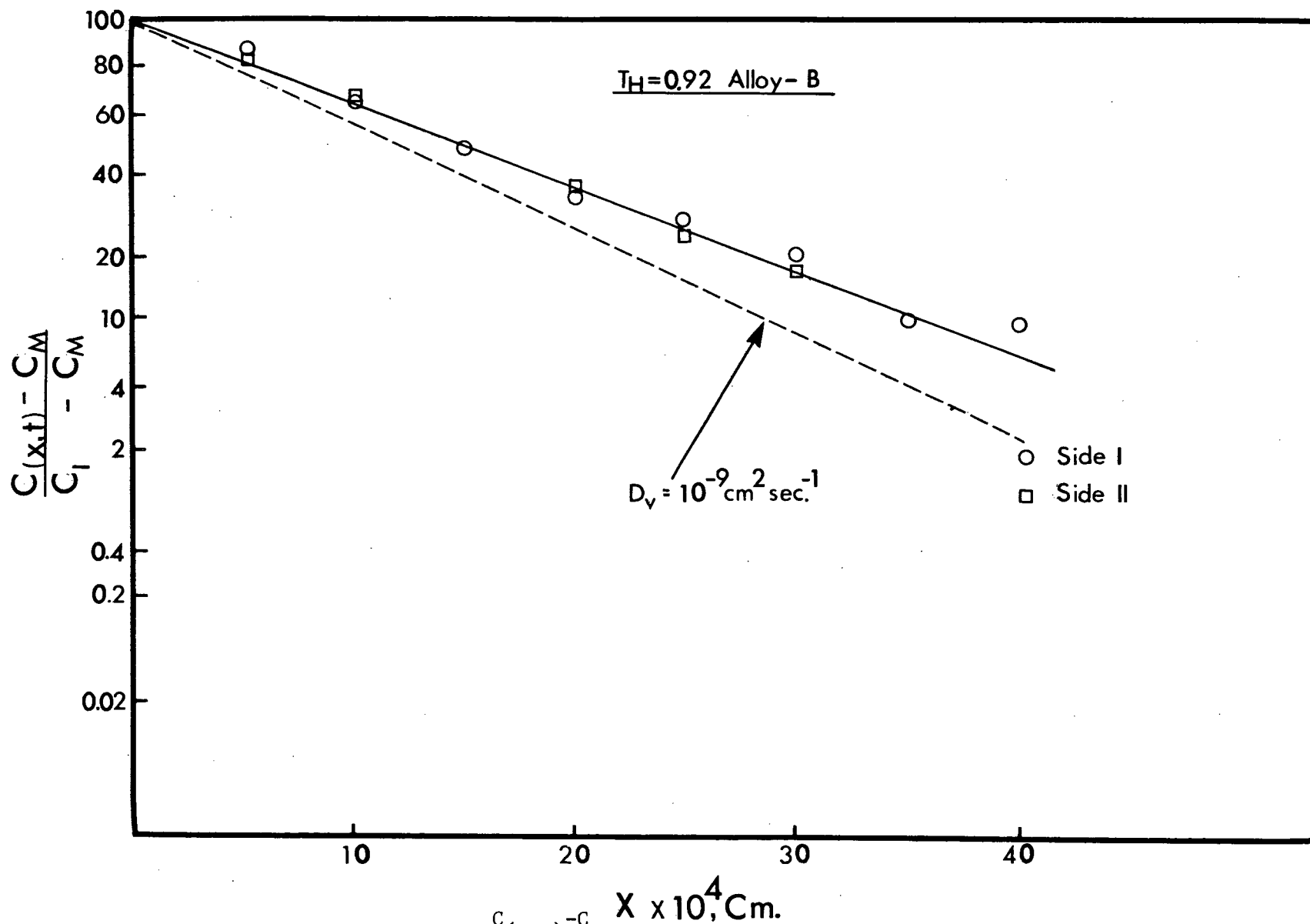


Figure 33. Probability plot of $\left[\frac{C(x,t) - C_M}{C_I - C_M} \right]$ versus diffusion distance (x) for alloy B at $T_H = 0.92$.

in Figure 32.

(3) Accurate values of D_V were obtained by plotting $\frac{C(x,t) - C_M}{C_I - C_M}$ versus x on probability paper. D_V can be calculated from the slope of the line in Figure 33, which is equal to $\frac{1}{2(Dt)^{1/2}}$.

(4) Iteration of (2) and (3) could be used to determine even more accurate values of D_V and C_I . This was, however, considered unnecessary considering the good agreement between the D_V and C_I values calculated and the literature values. Table V gives a comparison of the experimentally determined C_I values with the equilibrium phase diagram values.^{36,37} There is, in most cases, excellent agreement between the experimental and the literature values, which is consistent with the assumption that the dissolution process is diffusion controlled.

Table V. Interface Concentration (C_I) and Volume Diffusion Coefficients (D_V) for Contour Experiments.

Alloy	A		B						C	
Experimental values	5.60	4.76	5.62	4.97	4.57	4.27	3.60	2.85	2.40	2.15
C_I wt.% Cu										
Equilibrium diagram values	5.6	4.6	5.7	5.1	4.6	4.3	3.4	2.8	2.5	1.9
T_H	.97	.92	.940	.92	.90	.885	.86	.83	.80	.77
Experimental $D_V \times 10^{10} \text{ cm}^2 \text{ sec}^{-1}$	12.0	12.6	13.3	11.6	11.6	8.2	5.1	4.8	4.5	2.3
Murphy's values of D_V	13.2	9.5	13.2	10.5	9.5	6.1	3.0	1.9	1.5	0.6
Temperature °C	545	517	545	532	517	500	480	448	442	418

The probability plots for the evaluation of D_V were all found to be linear and thus indicated a concentration-independent diffusion coefficient, confirming the diffusion couple results.

Table V also gives the calculated values of D_V . The volume diffusion coefficients determined from the profile studies are in good agreement with the literature values at the high experimental temperatures. The experimental conditions at the low temperatures, resulted in:

- (1) smaller concentration gradients in the matrix,
- (2) shorter diffusion distances, and,
- (3) a greater possibility of a surface diffusion contribution to dissolution. This effect would enhance the dissolution rate but would leave the shape of the profiles unaffected. All these factors may be instrumental in the less accurate D_V values obtained at low temperatures.

The activation energy for volume diffusion has not been evaluated from the results, as the good correlation between individual volume diffusion coefficients and literature values, as well as the excellent agreement between calculated C_I values and equilibrium phase diagram values, is adequate demonstration of the consistency and accuracy of the concentration contour experiments.

3.5 The Effect of Supersaturation (k) and Volume Diffusion Coefficient (D_V)

In any one alloy, changing the temperature changes both the volume diffusion coefficient (D_V) and the supersaturation (k). This makes

it difficult to estimate the individual contributions of these two variables. They will therefore be considered in one section, and an attempt will be made to show the effect of each of these factors on the shape of the isoconcentration contours.

In order to determine the effect of k on the shape of the isoconcentration lines, measurements were carried out at $T_H = 0.92$ for alloy A with $k = 0.035$. The results are shown in Figure 34, which can be compared to Figure 25, in which the homologous temperature is the same but k is appreciably higher ($k = 0.094$). The dissolution temperatures were different in the two cases (517°C for Figure 34 and 532°C for Figure 25). Comparing the two figures, it is evident that although the actual concentration values and diffusion distances are quite different the overall shape of the isoconcentration contours is the same.

In the above experiment both the temperature and the supersaturation were different. An evaluation of the influence of these two variables will be attempted by making a comparison between pairs of experiments in which either T , k or T_H are kept constant. Five sets of such experiments are listed in Table (VI), three sets have T_H constant, one set has T constant and one has k approximately constant. All three sets of isoconcentration lines having a constant T_H have the same shape. In both the cases of a constant volume diffusion coefficient and constant k , but different T_H , there is no similarity in the shape of the isoconcentration contour pairs. One may safely conclude that the influence of homologous temperature on the shape of the isoconcentration contours is independent of both the volume

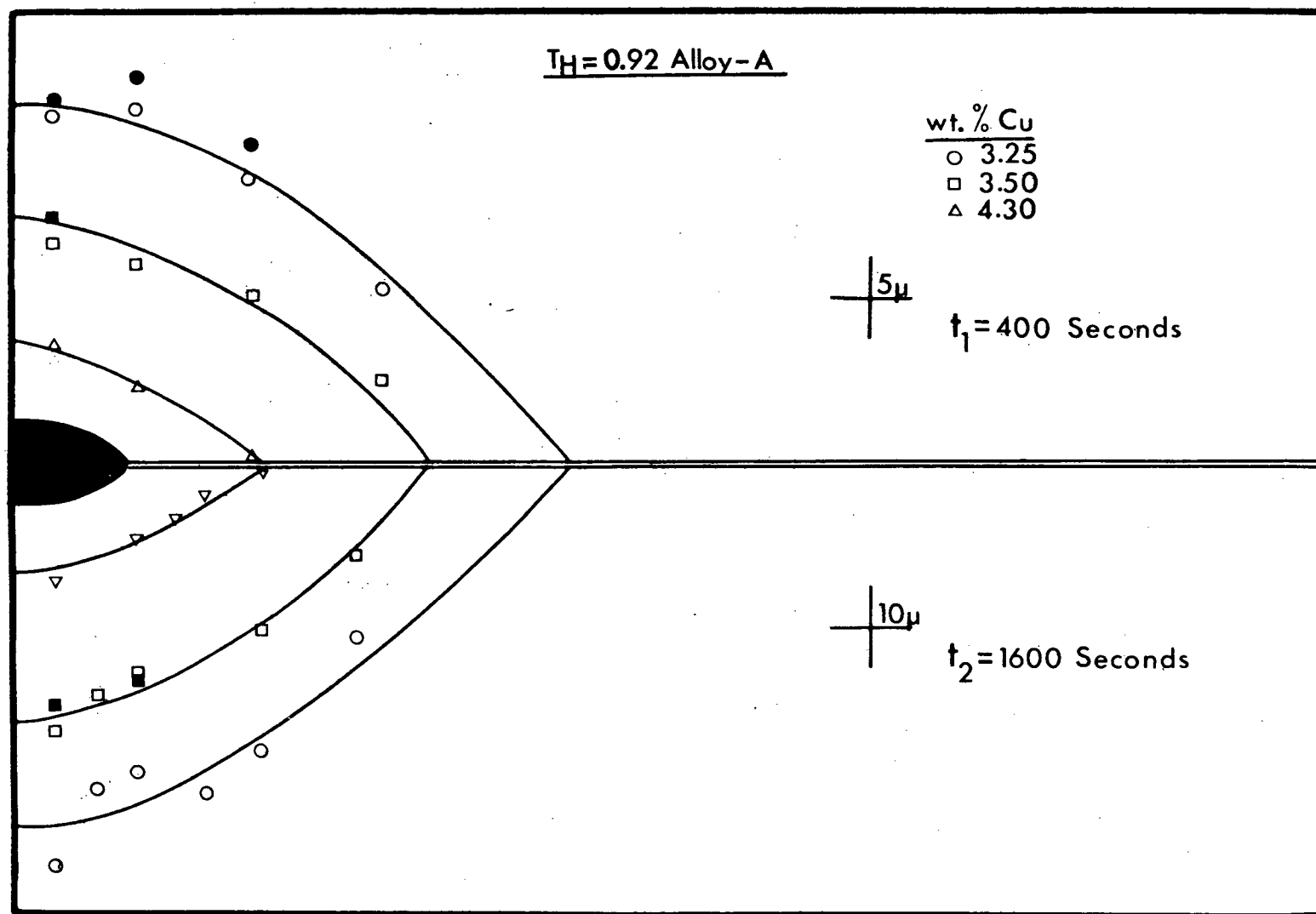


Figure 34. Isoconcentration contours for alloy A at $T_H = 0.92$.

Table VI. Comparison of the Effects of k , T and T_H on the Shape of Isoconcentration Contours.

Alloy	Temp. °K	T_H	$D \times 10^{10}$ $\text{cm}^2 \text{sec}^{-1}$	$S/\text{sat.}$ k	Shape of Contours	Fig. No.
A	790	.92	7.3	.035	same	34
B	805	.92	10.7	.094		25
A	790	.92	7.3	.035	different	34
B	790	.905	7.3	.078		26
Al-Ag	823	.93	50	.597	same	43
A	800	.93	9.4	.045		21
Al-Ag	786	.885	22	.341	same	42
B	777	.885	5.4	.0653		45
A	818	.97	7.3	0.515	different	23
B	753	.86	2.8	0.511		27

diffusion coefficient and the supersaturation.

3.6 The Effect of Grain Boundary Misorientation (R)

The Al-15.75 wt.% Ag alloy had a micro-structure with a significant number of low angle grain boundaries. These were identified using the Clark ⁴ classification of precipitate morphology in this system.

On one grain boundary it was found that nearly all the precipitates were in the form of primary side plates and sawteeth ($R \sim 9.5^\circ$). However, two precipitates on this boundary resembled allotriomorphs. Composition contours were measured around these and were compared with composition contours obtained from an allotriomorph on a high angle grain boundary at the same temperature. In Figure 35 the profiles clearly show that grain boundary diffusion effects are not important for low angle grain boundaries, whereas in Figure 36 there is a significant grain boundary contribution to dissolution for a high angle grain boundary.

Investigations of the effect of grain boundary misorientation on the grain boundary diffusion coefficient ^{43,44} have shown that beyond a misorientation of $R \sim 20^\circ$ there is very little significant variation of $D_{g.b.}$. Since grain boundary allotriomorphs generally form on grain boundaries with a misorientation $R > 17^\circ$, the grain boundary contribution would not be expected to vary significantly from allotriomorph to allotriomorph. The experimental results appear to confirm this because the diffusion distances along the grain boundary vary by no more than 15% from precipitate to precipitate in any one system, for any one set of experimental conditions.

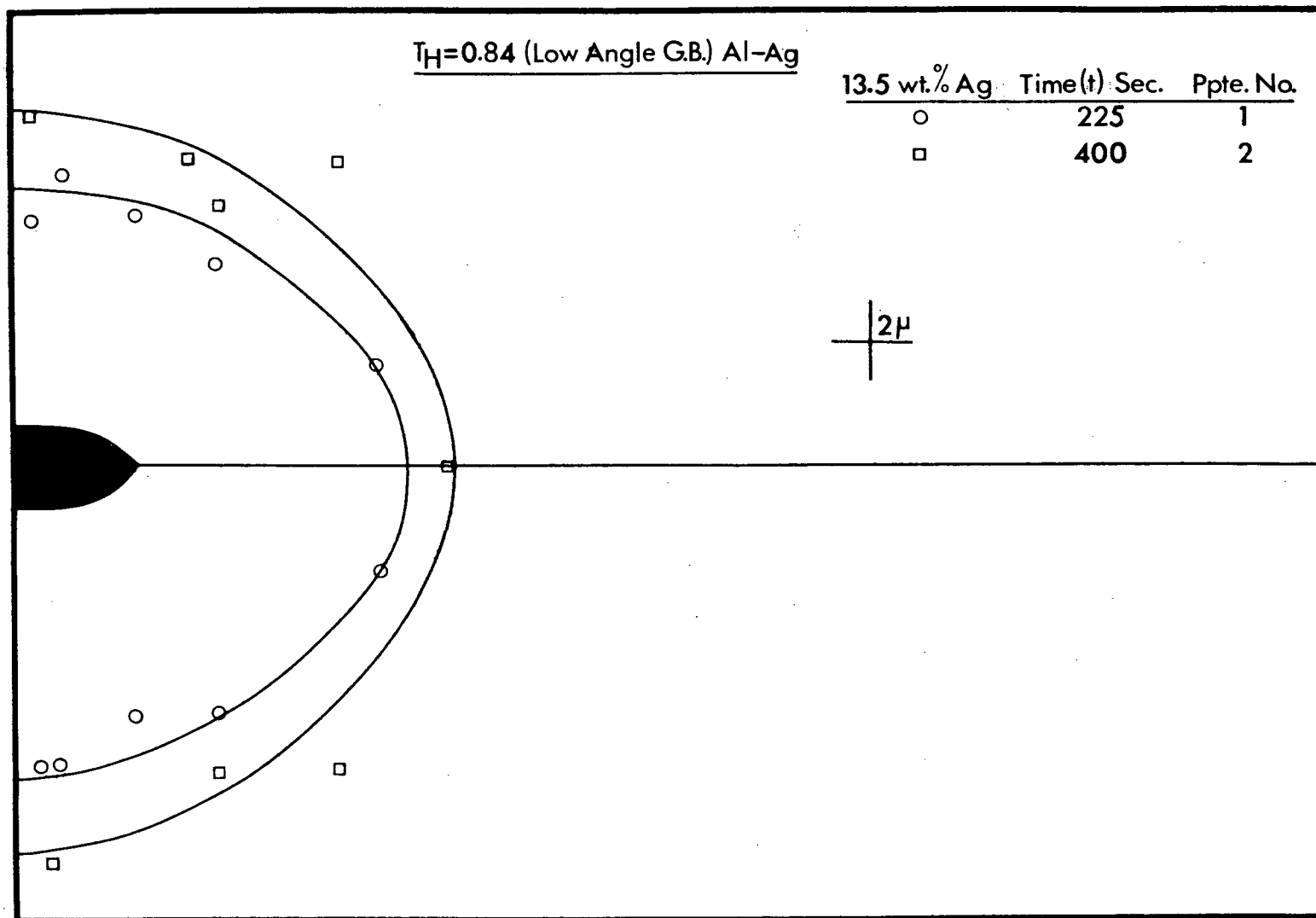


Figure 35. Isoconcentration contours of two allotriomorph shaped precipitates situated on a low angle grain boundary for the Al-Ag alloy at $T_H = 0.84$.

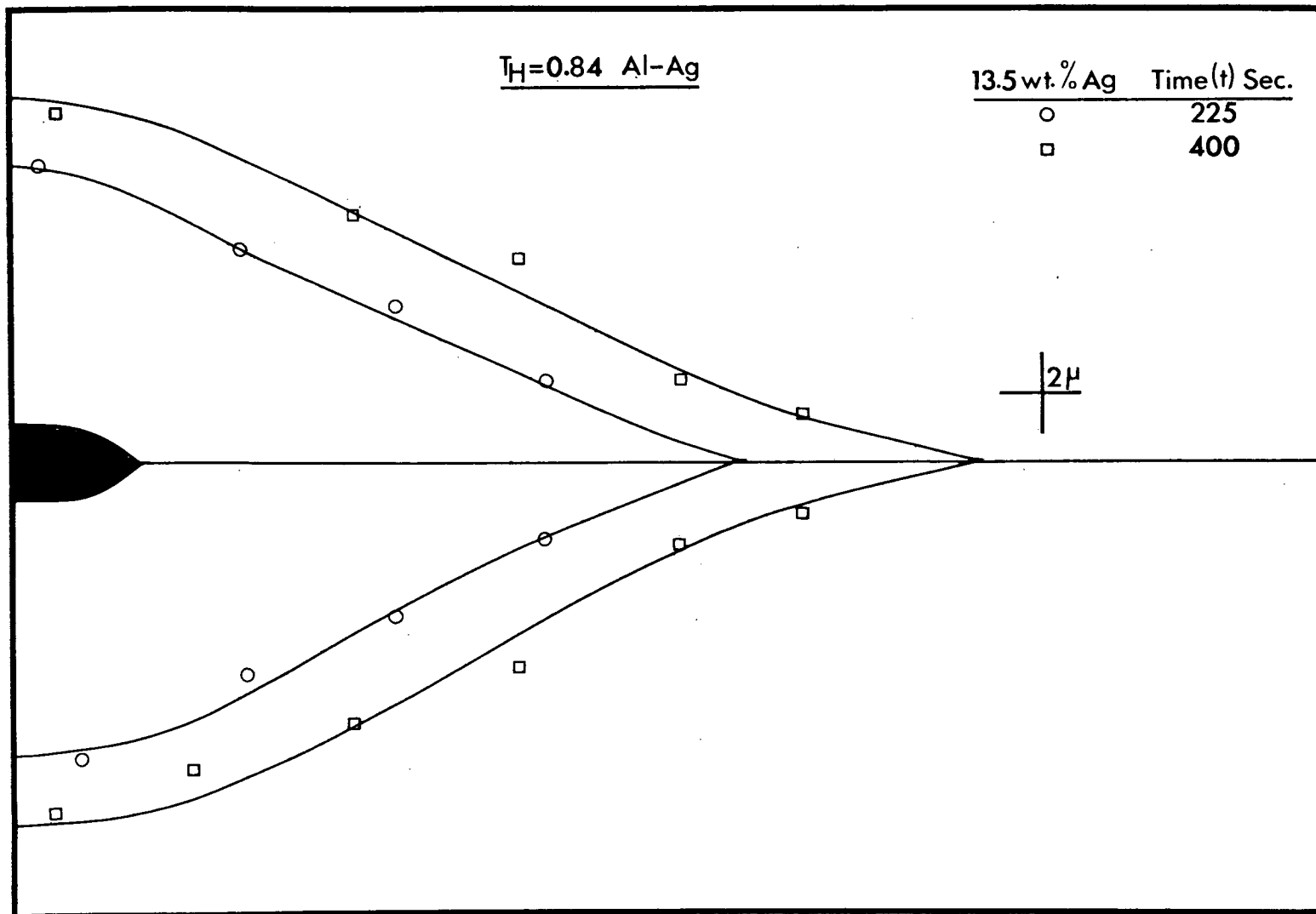


Figure 36. Isoconcentration contours for the Al-Ag alloy at $T_H = 0.84$.

3.6.1 Evaluation of the Grain Boundary Diffusion Coefficient ($D_{g.b.}$)

A model developed by Shewmon⁴⁵ for surface diffusion was used to evaluate $D_{g.b.}$ in the present work. In Shewmon's model, solute is considered to quickly diffuse out along a surface from a cylindrical source. From the surface the solute then diffuses into the bulk of the material by a volume diffusion process. Shewmon's model is the cylindrical analogue of Fisher's model⁴⁶ for one-dimensional surface diffusion (see Figure 37). It suffers from the same approximations as used by Fisher; viz: that diffusion occurs in the bulk only in the direction perpendicular to the surface and that steady state conditions on the surface are established early in the diffusion process. However Turnbull et al.⁴⁷ in a critical evaluation of the Fisher Model and the more sophisticated Whipple⁴⁸ Model, found that $D_{g.b.}$ values calculated from the different models differed only by a few percent. The Shewmon model is immediately applicable to dissolution from circular precipitates by diffusion along the grain boundaries and has been used in this connection by Brailsford and Aaron.²⁰ In this case the solution takes the form:

$$C(\rho, z, \tau) = C_{g.b.}(\rho, \tau) \operatorname{erfc}(z/2\sqrt{D_V \tau}) \quad 1$$

where

$$C_{g.b.}(\rho, \tau) = C_M + (C_I - C_M) [K_O(\alpha \cdot \rho) / K_O(\alpha \cdot b)] \quad 2$$

$$\alpha^2 = 2D_V / D_{g.b.} \delta(\pi D_V \tau)^{1/2} \quad 3$$

τ is the annealing time,
and b is the source radius.

and the boundary conditions on $C_{g.b.}(\rho, \tau)$ are

$$C_{g.b.}(b, \tau) = C_I$$

$$C_{g.b.}(\infty, \tau) = C_M$$

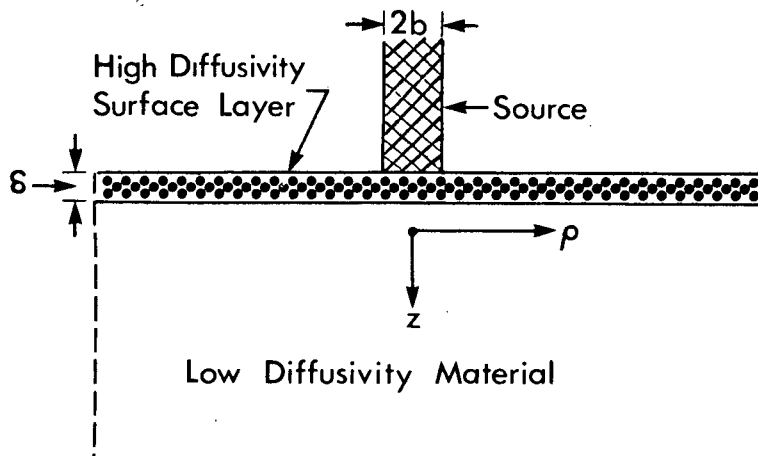


Figure 37. Schematic diagram for Shewmon surface diffusion model (after P.G. Shewmon).

The concentration contours at low temperatures in the present work were used to determine $D_{g.b.}$ from equations (2) and (3). In these contours there was little direct volume diffusion contribution to the gradient along the grain boundary. Figure 38 represents the calculations of $D_{g.b.}$. The theoretical profiles along the grain

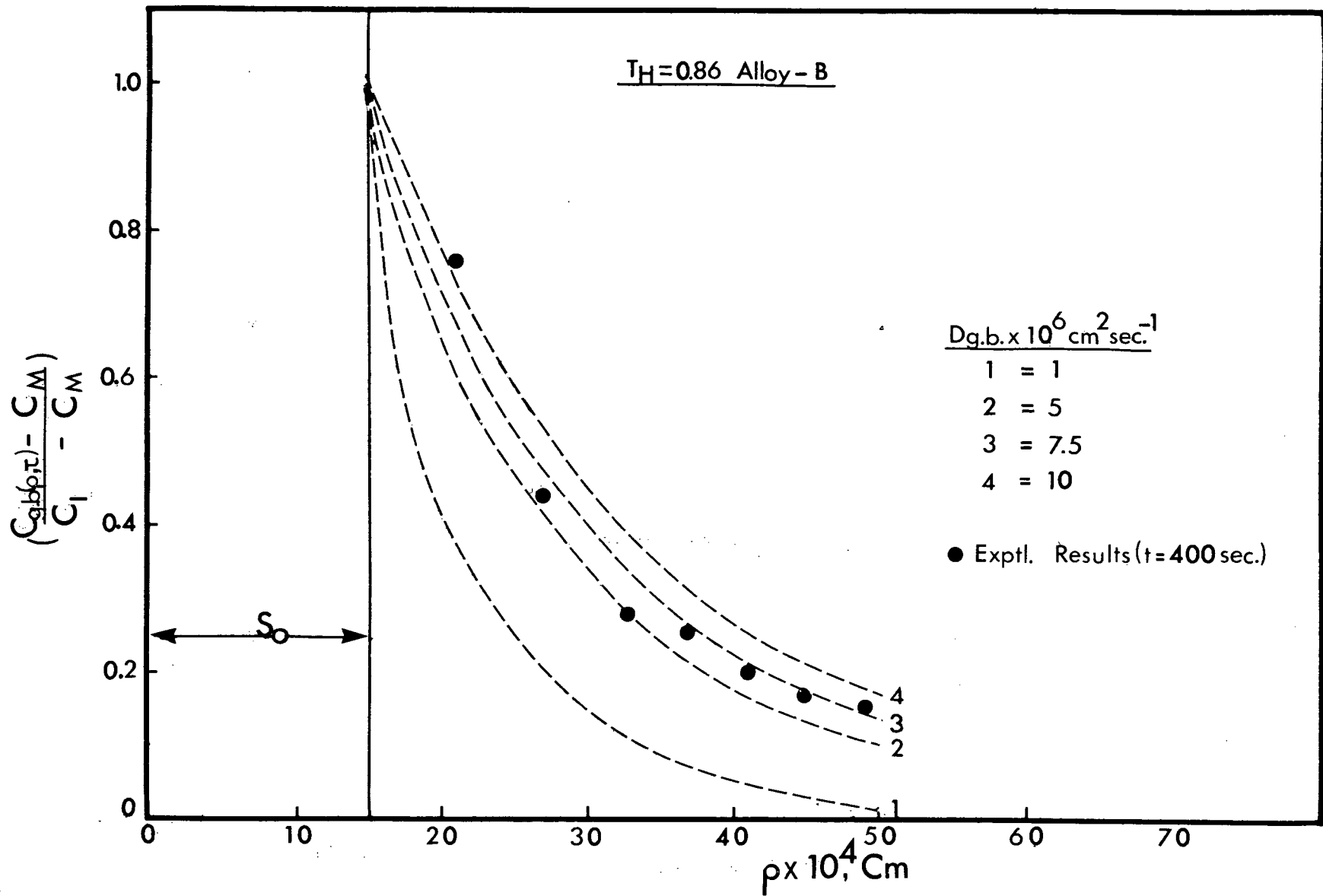


Figure 38. Evaluation of $D_{g.b.}$ for alloy B at $T_H = 0.86$.

boundary were calculated for various values of $D_{g.b.}$ and the best fit with the experimental data of the dissolution of alloy B at a homologous temperature $T_H = 0.86$ (see Figure 27) was taken as the experimental value of $D_{g.b.}$ (see Figure 38). Grain boundary diffusion coefficients were determined for several temperatures, the results being shown in Table VII. An approximate grain boundary diffusion coefficient has also been calculated assuming:

$$Q_{g.b.} = \frac{1}{2} Q_{volume}$$

$$D_0^{g.b.} = D_0^{vol.} = 0.29 \text{ cm}^2/\text{sec}$$

The activation energy for volume diffusion is taken as $Q_{volume} = 31.13$ kcal/g.mole.³⁹ The result is included in Table VII, for $T = 480^\circ\text{C}$.

The experimental value of $D_{g.b.}$ is in reasonable agreement with the value of $D_{g.b.}$ calculated at 480°C . However, the inconsistency of the values of $D_{g.b.}$ calculated at the other temperatures is not surprising considering: (1) the approximations made in arriving at values of $Q_{g.b.}$ and $D_0^{g.b.}$ (2) that the experimental observations show a diffusional distance along the grain boundary which obeys an almost parabolic relationship with time, whereas the Shewmon model predicts a $t^{0.25}$ relationship, and (3) the fact that the experimental technique used is not one from which accurate evaluations of $D_{g.b.}$ are to be expected. These $D_{g.b.}$ calculations are intended as peripheral information based on the experimental results.

Table VII. Grain Boundary Diffusion Coefficients ($D_{g.b.}$) Determined from Contours

$T^{\circ}C$	$D_{g.b.} \times 10^5 \text{ cm}^2 \text{ sec}^{-1}$
520	7.5 [*]
504	9.0 ^{**}
480	0.75
448	7.5
420	5.0
480 (calculated)	0.83

^{*,**} The grain boundary diffusion coefficient has been determined at these temperatures, even though the relative amount of volume to grain boundary diffusion is very large resulting in a high degree of error in the calculation of $D_{g.b.}$.

3.7 Semi-Quantitative Analysis of Isoconcentration Contours

It has generally been found in diffusion studies that no effect due to grain boundary diffusion can be seen at temperatures above $0.6 T_M$. It is rather surprising therefore that in the present work a grain boundary diffusion contribution persists to a homologous temperature greater than 0.92. One of the essential differences between the two phenomena is statistical in nature. For grain boundary diffusion in a single phase polycrystalline material, one must consider the mean time that an atom spends in the grain boundary as well as the probability of its getting onto the boundary. In dealing with the dissolution of grain boundary allotriomorphs, this statistical aspect is eliminated since the precipitate is, in fact, situated on the grain boundary.

A theoretical analysis of the relative contributions of grain boundary and volume diffusion to allotriomorph dissolution has been developed by D.E. Coates (see Appendix VI for details).

The main features of this analysis are:

(1) The use of Laplace's equation ($\nabla^2 C = 0$) to calculate the volume diffusion field about the allotriomorph. This approximation is good for low supersaturations and for longer diffusion times.

(2) The use of two extreme conditions: (i) where volume diffusion is the sole contributor to dissolution, as in Figure 22, and (ii) where grain boundary diffusion is the overwhelming contributor to dissolution as in Figure 30.

(3) A function ψ is evaluated, where ψ is the relative contribution to the total flux out of an allotriomorph due to grain boundary

diffusion and volume diffusion, viz:

$$\psi \equiv \frac{(\int_I \vec{J}_I \cdot d\vec{A})_{g.b.}}{(\int_I \vec{J}_I \cdot d\vec{A})_{vol.}} \quad 1$$

If $\psi \gg 1$ grain boundary diffusion dominates.

If $\psi \ll 1$ volume diffusion dominates.

As shown in Appendix VI, ψ is given by

$$\psi = \sqrt{\frac{e^{Q/2RT}}{2(\pi D\tau)^{1/2}}} \cdot \frac{K_1 \left[a \sqrt{\frac{-Q/2RT}{2e}} \frac{1}{(\pi D\tau)^{1/2}} \right]}{K_0 \left[a \sqrt{\frac{-Q/2RT}{2e}} \frac{1}{(\pi D\tau)^{1/2}} \right]} \cdot f(a/b) \quad 2$$

where K_1 and K_0 are modified Bessel functions of first and zero order respectively and it is assumed

$$D_{g.b.}/D_V = e^{-Q/2RT}$$

where Q is the activation energy for volume diffusion.

For a given precipitate size a and diffusion distance $(\pi D\tau)^{1/2}$

equation (2) is essentially an equation of the form $\psi = \psi(T)$. ψ is plotted in Figure 39 for the experimental conditions corresponding to three of the alloys used.

The progressive transformation from grain boundary diffusion control to volume diffusion control with increasing temperature can be

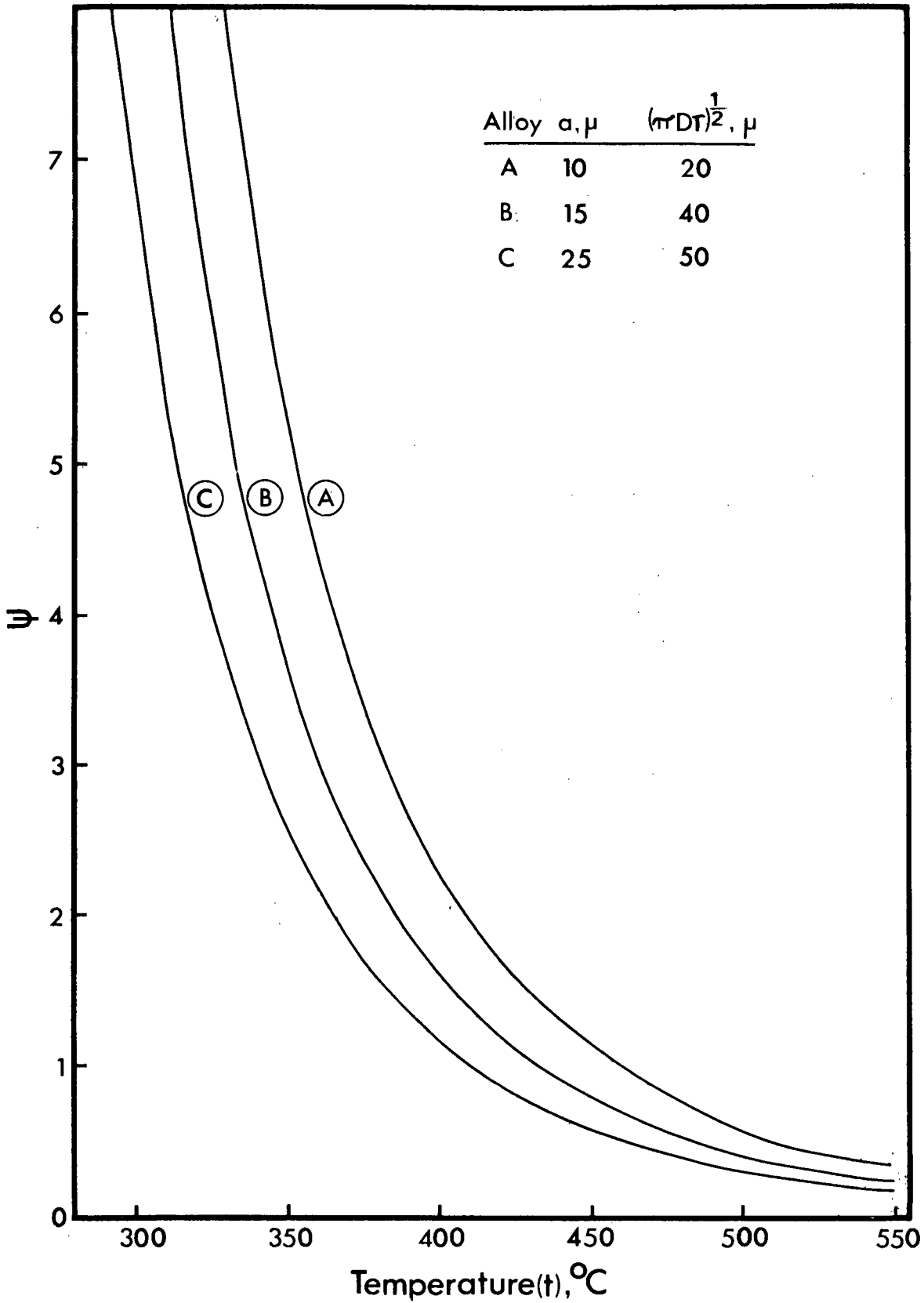


Figure 39. The function $\frac{\text{flux via grain boundary diffusion}}{\text{flux via volume diffusion}}$ (ψ) versus temperature T.

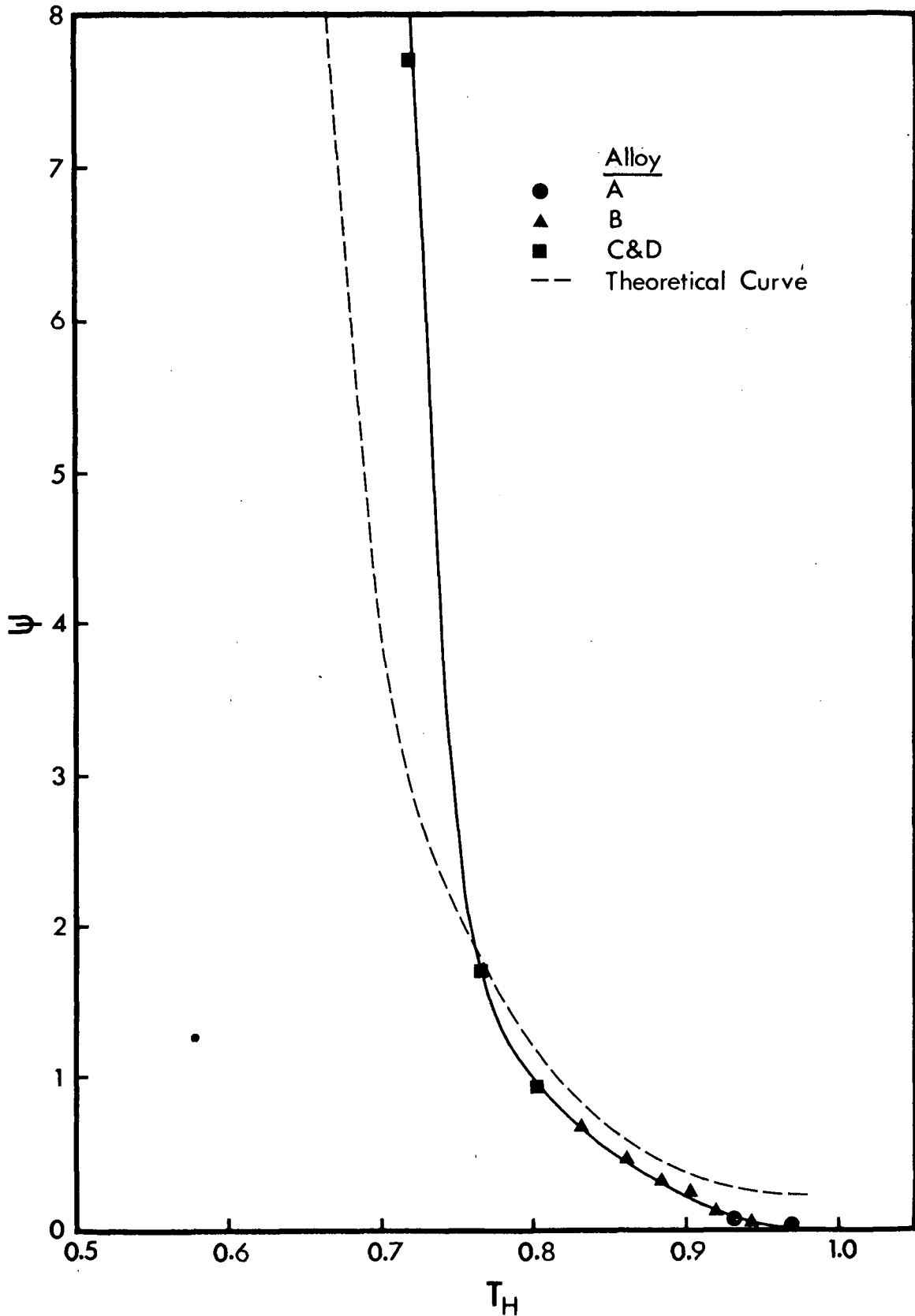


Figure 40. A comparison of theoretically derived ψ versus homologous temperature T_H with the experimental observation of solute via grain boundary diffusion solute via volume diffusion

clearly seen. The three plots are drawn as a function of homologous temperature in Figure 40, and are found to coincide giving one curve. This is a fortuitous effect, as the increase in the precipitate size (precipitate half length a) with increasing alloy content compensates for the longer experimental dissolution times $(\pi D\tau)^{1/2}$ (see equation 2). It is thus clear why for the present experimental conditions ψ is only a function of T_H , rather than a function of the actual temperature. The dissolution of grain boundary allotriomorphs solely by grain boundary diffusion occurs below $T_H = 0.72$, which is in excellent agreement with the theoretically predicted value at which grain boundary diffusion dominates. The theoretical calculations confirm the significance of the contribution of grain boundary diffusion to the total flux even at high homologous temperatures.

From the experimental data, it is possible to make an approximate calculation of the total flux due to volume diffusion and that due to grain boundary diffusion. The composition contour corresponding to volume diffusion is essentially an oblate spheroid. The extra contribution is assumed to be due to grain boundary diffusion as in Figure 41. By measuring the two areas and integrating over the solid angle corresponding to an oblate spheroid, the relative grain boundary and volume contributions to dissolution can be calculated. The experimental points in Figure 40 represent the ratio:

$\frac{\text{area due to g.b. diffusion}}{\text{area due to volume diffusion}}$, calculated as depicted schematically in Figure 41 for all the profiles measured. The experimental results are in good agreement with the theoretical values. The theoretical analysis (equation 2) predicts no effect of supersaturation and little

- 1 G.B. Allotriomorph
- 2 Solute via Volume Diffusion
- 3 Solute via G.B. Diffusion
- 4 Grain Boundary (G.B.)

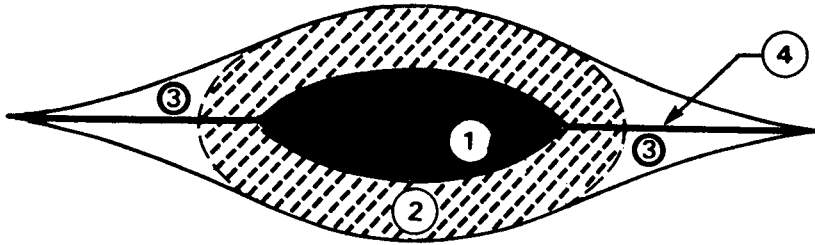


Figure 41. Schematic diagram of method used to calculate 1) solute via grain boundary diffusion, and 2) solute via volume diffusion.

effect of axial ratio, both of which are in agreement with the experimental observations (see Appendix VI).

3.8 The Al-15.75 wt.% Ag System

Figures 36, 42, and 43 show the concentration contours at three different homologous temperatures in the Al-Ag system. As can be seen by comparing these results with those in the Al-Cu system (viz: Figures 36 and 44, Figure 42 and Figure 23, Figure 43 and 45) there is excellent agreement in the shape of these contours at equivalent homologous temperatures.

In both the Al-Cu and the Al-Ag systems, allotriomorphs having a relatively complex structure are dissolving into an f.c.c. matrix. The diffusion coefficients of these alloys differ by a factor of five^{39,49} at equivalent homologous temperatures. The supersaturation

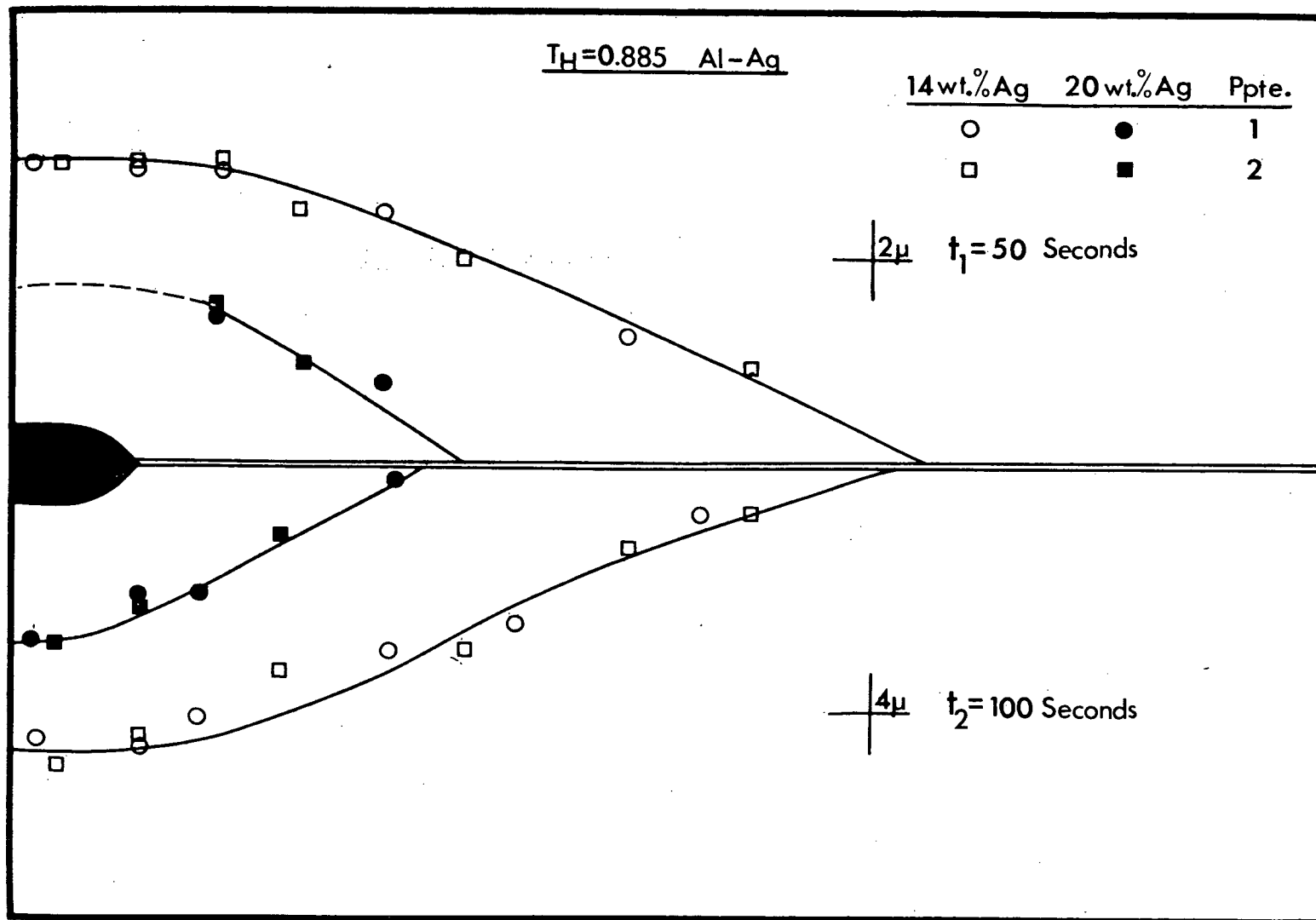


Figure 42. Isoconcentration contours for the Al-Ag alloy at $T_H = 0.885$.

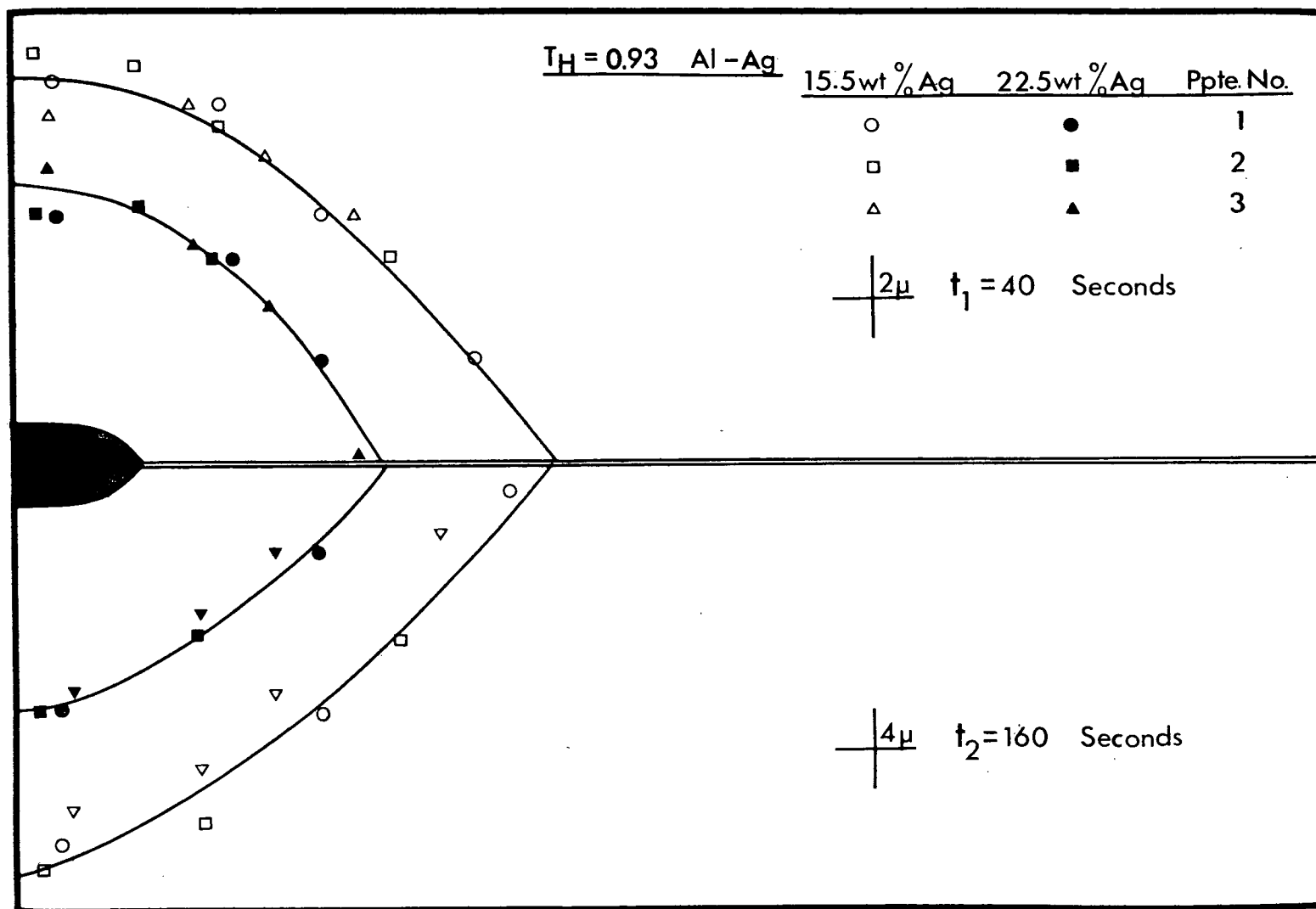


Figure 43. Isoconcentration contours for the Al-Ag alloy at $T_H = 0.93$.

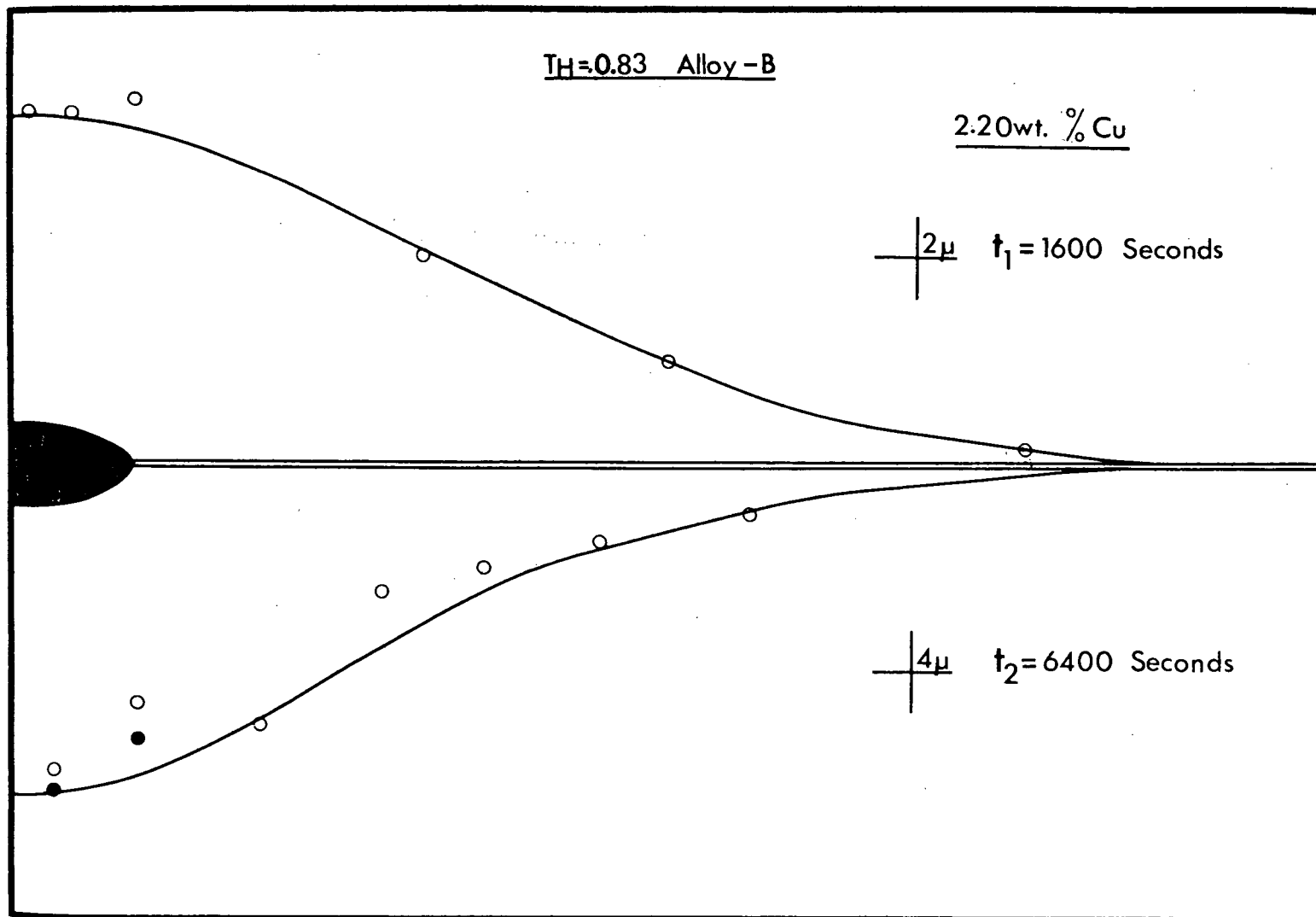


Figure 44. Isoconcentration contour for alloy B at $T_H = 0.83$.

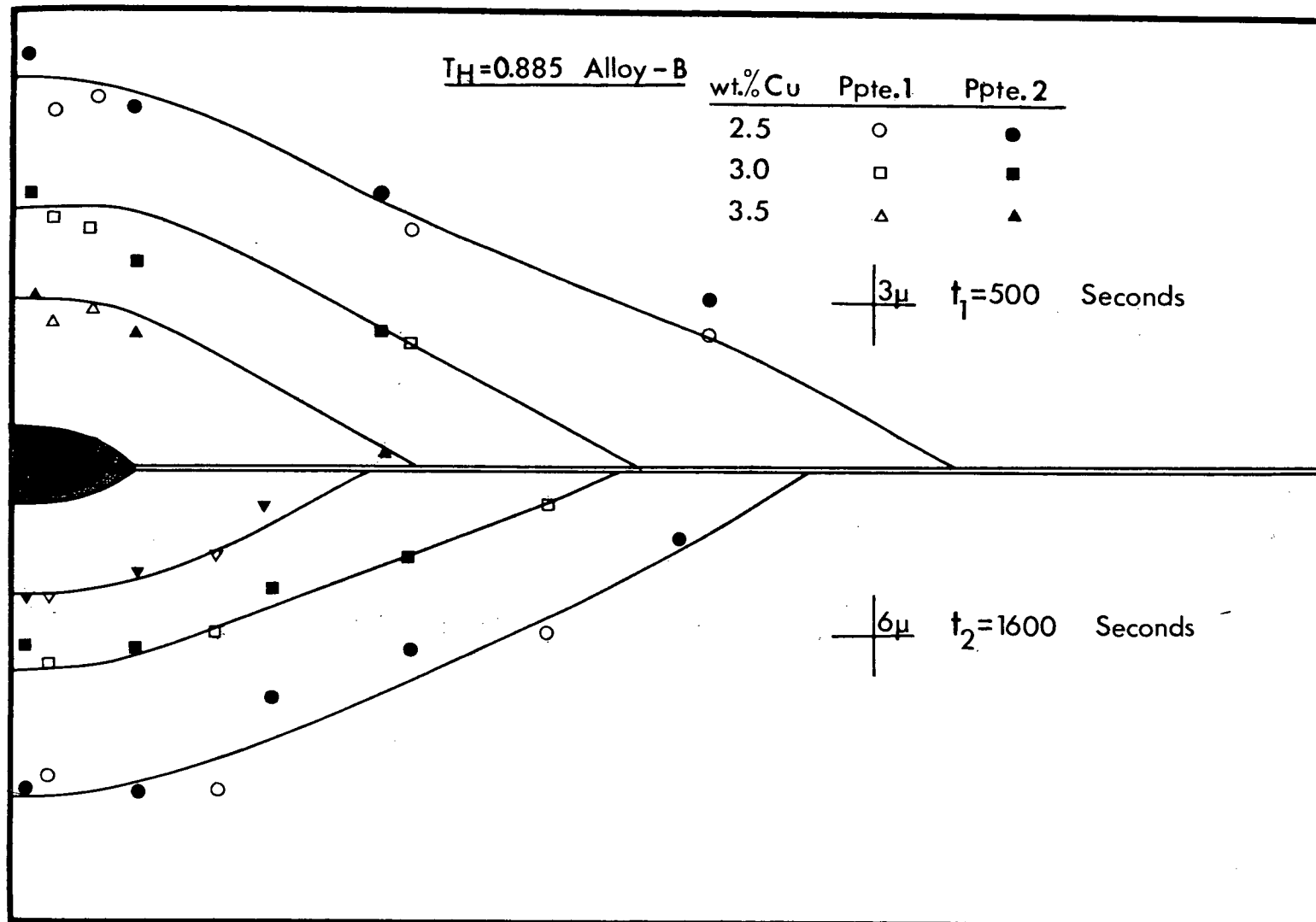


Figure 45. Isoconcentration contours for alloy B at $T_H = 0.885$.

however may vary by more than an order of magnitude (see Table V).

The observation that the isoconcentration contour shapes are comparable for comparable homologous temperatures confirms the singular importance of the homologous temperature; changing the supersaturation only alters the values for the concentration contours, not their shape.

Calculations of C_I in this system are in good agreement with phase diagram data (as in Figure 5). D_V is found to be independent of concentration over the total solid solubility range, as was found by Heuman and Böhmer.⁴⁹ Figure 46 compares values of D_V calculated from the contours with values of D_V found in the literature. The agreement is good for both individual values of D_V as well as for the calculation of the activation energy.

3.9 Applicability of Contours

It has been found that the dissolution contours in both the Al-Cu and Al-Ag systems are very similar at comparable homologous temperatures. It thus seems probable that the present results are applicable to any dissolving grain boundary allotriomorph. The diffusion coefficients in Al-Cu and Al-Ag are similar at similar homologous temperatures and so the transformation from grain boundary diffusion to volume diffusion control occurs at the same T_H in both cases. The relationship of volume diffusion coefficient to homologous temperature in other systems, will determine the T_H at which the transformation between grain boundary and volume diffusion control occurs. The basic shapes of the contours will however, be the same and can simply be translated to different T_H values.

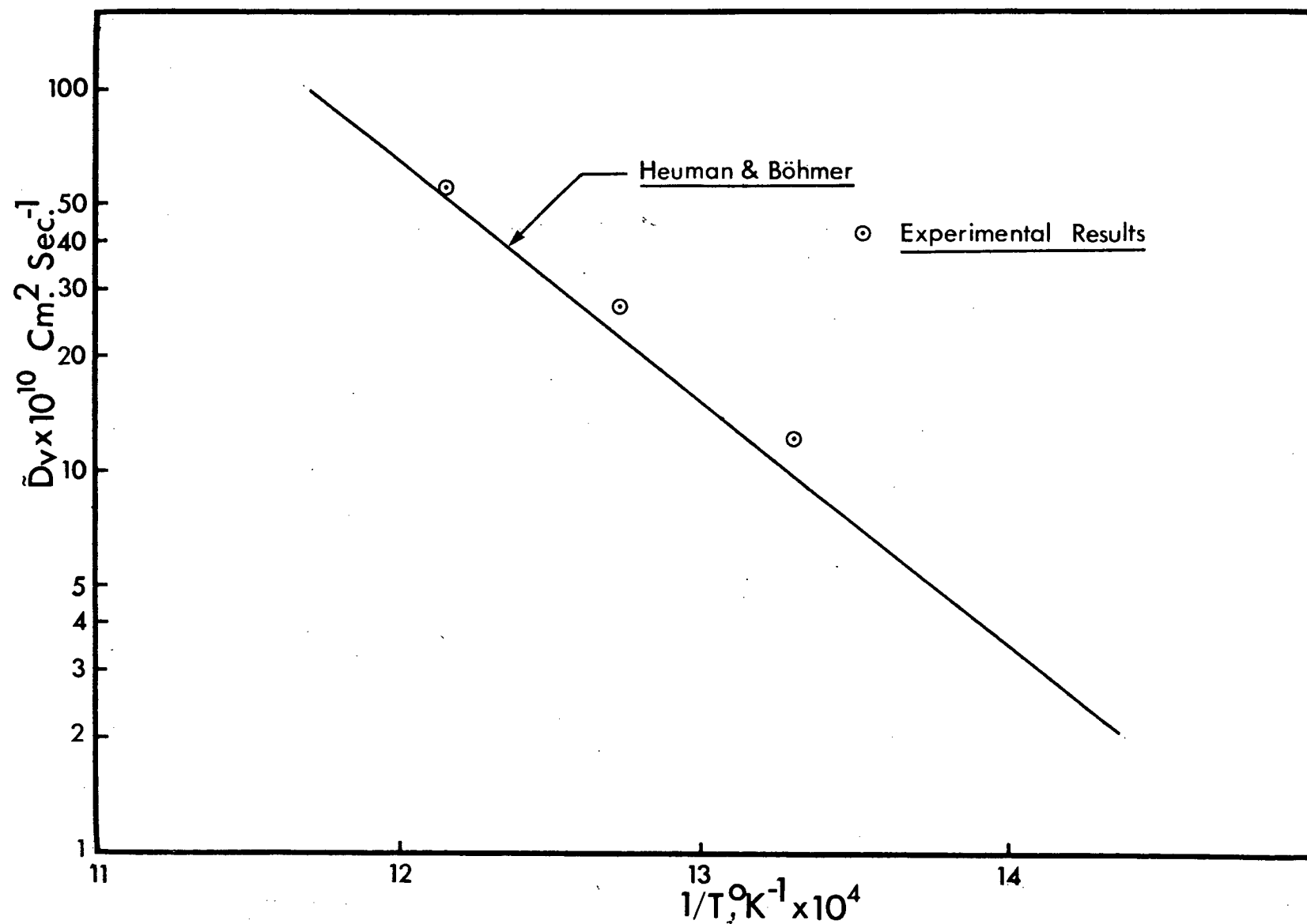


Figure 46. Arrhenius plot of D_v versus $1/T, ^\circ\text{K}^{-1}$ for the Al-15.75 wt.% Ag alloy.

4. KINETIC RESULTS AND DISCUSSION

4.1 Introduction

In this chapter, observed dissolution kinetics of grain boundary allotriomorphs are analysed. The results are discussed in terms of the most appropriate existing analytical models for allotriomorph dissolution. The latter include Whelan's spherical and planar models for precipitate dissolution^{28,29} and Aaron's planar model.⁵⁰ It is important to note that under the present experimental conditions, impingement of the diffusion fields from adjacent precipitates takes place at a very early stage in the dissolution process (see Table III). On the other hand, the three models just cited are based on the assumption that the diffusion fields of adjacent precipitates do not impinge at all (i.e., these models relate to the dissolution of a single precipitate in an infinite matrix). Accordingly it is anticipated that the correlation between these models and the present experimental results will be, at best, semi-quantitative. Thus an attempt is made to provide a firmer basis for interpretation of the results by formulating a dissolution model which accounts for impingement of the diffusion fields.

4.2 Analysis of Dissolution Kinetics Using Existing Planar and Spherical Models

Table VIII gives a resumé of all the kinetic experiments and includes the number of precipitates studied, the dissolution times and temperatures, and the supersaturation values (k).

It should be noted that the time for complete dissolution of precipitates varied from 5 minutes to 116 hours, depending on the experimental conditions.

Whelan's spherical model^{28,29} was formulated for application to the later stages of the dissolution of spherical precipitates. Diffusion field impingement is completely ignored in the derivation. For the later stages one can approximate that only the steady state diffusion field contributes to the dissolution rate (see Section 1.3.1, equation (4)).

To apply the Whelan spherical model a plot of R^2 versus t was made for each precipitate studied. If the model is valid, such plots should be linear. In fact, these plots were not linear, indicating the model is not consistent with the present data (see Figure 47). It should be noted however that whereas the plots of R^2 versus t are not linear for the full extent of the dissolution heat treatment. There is a tendency at the later stages of the dissolution process for the relationship R^2 versus t to become linear, indicating at least a qualitative agreement with Whelan's experimental observations.²⁹

Whelan's planar²⁹ and Aaron's⁵⁰ planar models are formulated for planar precipitates and for the early stages of dissolution before impingement takes place, and are thus not applicable to the present set

Table VIII. Kinetic Experiments.

Alloy	Number of Precipitates	T_H	Super- saturation (k)	$T^\circ\text{C}$	Time
D	2	0.76	0.014	424	0,10,20,37,65,125,180,125, 307,442,560,686,816,1003 min
Al-Ag	6	0.84	0.123	460	116,220,320,457,678,1123 min
C	6	0.79	0.036	450	0,55,110,220,440,700 min
B	4	0.83	0.032	460	0,1/3,1,3,4,6 1/2,9,12 1/2, 16,20,25,34,44,51,62,89, 116 hrs.
D	6	0.84	0.039	489	0,5,8,11,15,24,36,50,69, 82 min
D	5	0.86	0.092	500	0,1/2,1 1/2,3,6,12 min
B	8	0.88	0.065	500	0,1 1/2,6,24,48,72,96,144 min
B	6	0.86	0.059	489	15,30,45,60,80,100,156,212, 297 min
D	5	0.89	0.116	534	0,1/2,1,2,3,5 min
Al-Ag	4	0.88	0.328	500	5,17,38,60,90 min
B	5	0.90	0.078	513	1 1/2,6,12,18,24,48 min
Al-Ag	6	0.92	0.597	534	1/2,1 1/2,3,5,7 1/2 min
A	5	0.95	0.048	520	1,4,16,66 min
A	9	0.97	0.052	534	5,10,20,30,50 min
B	5	0.92	0.09	534	3,6,10,15,20 min

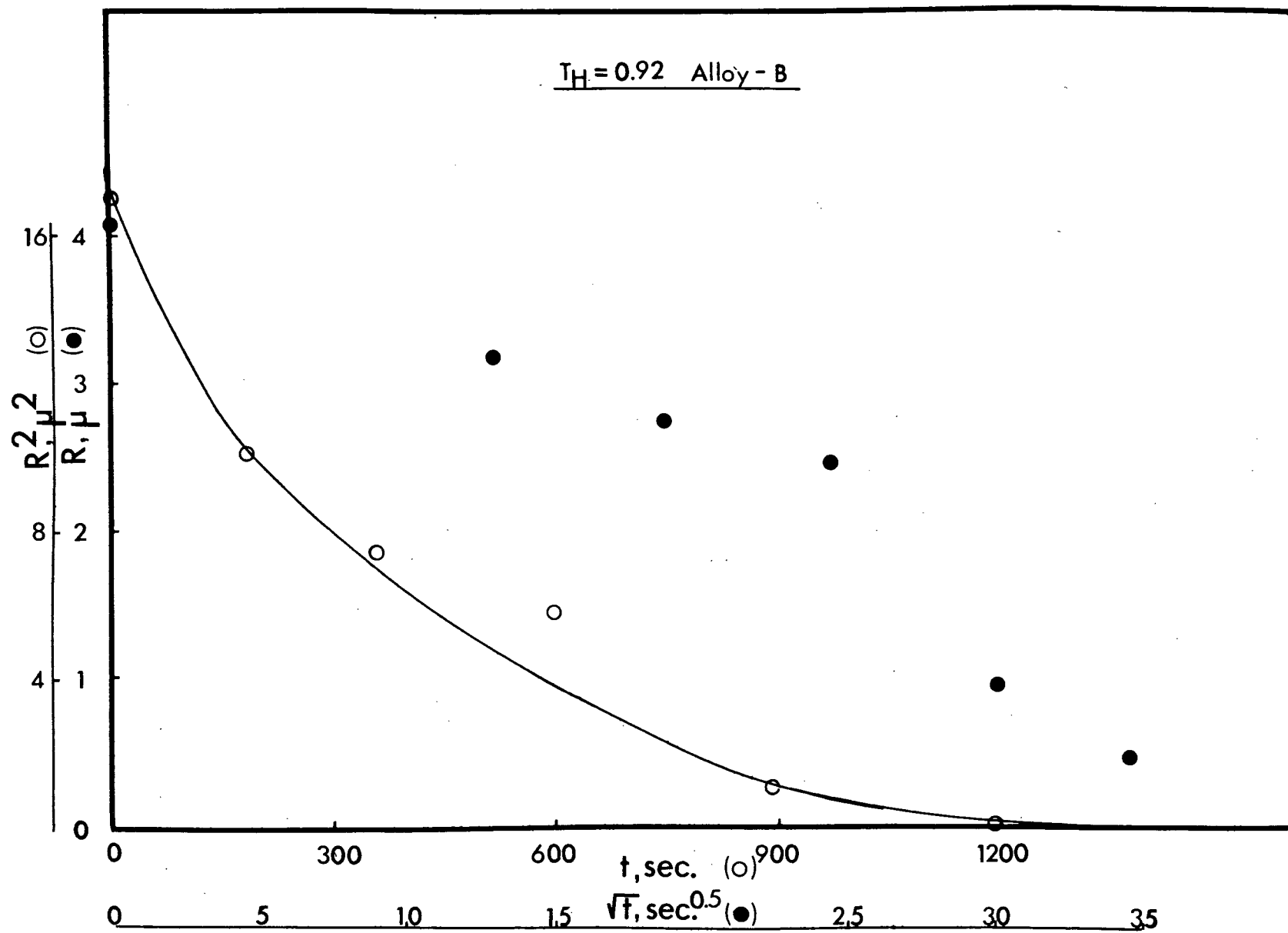


Figure 47. A plot of R^2 versus t and R versus \sqrt{t} for alloy B at $T_H = 0.92$.

of experimental data.

Whelan's planar model²⁹ (see Section 1.3.1) differs from Aaron's planar model⁵⁰ by a factor of $\sqrt{\pi}/2$ in the constant k of equation (7) in Section 1.3.1.

A plot of R versus \sqrt{t} for the experimental results should give a linear relationship if this model is valid.

The experimental results for some precipitates give a linear relationship for the total amount of dissolution observed, with a significant amount of scatter. A linear fit is observed in the case of a few precipitates for only the earlier dissolution times (see Figure 47). However, no conclusion can be drawn as to the applicability of this model to the early stages (that is before impingement), as the majority of the observations were made after a certain amount of impingement had occurred.

In an attempt to find the best correlation between R and t, the data was plotted in the form $\log R/R_0$ versus t and, to a good approximation, a linear relationship was obtained.

Figures 48 to 52 are typical examples of $\log R/R_0$ versus t and $\log S/S_0$ versus t plots for the homologous temperature range from $T_H = 0.97$ to $T_H = 0.76$. The observed linear relationship indicates that a relationship of the form

$$R = R_0 e^{-k_1 t} \quad 1$$

is applicable to the change in half thickness and

$$S = S_0 e^{-k_2 t} \quad 2$$

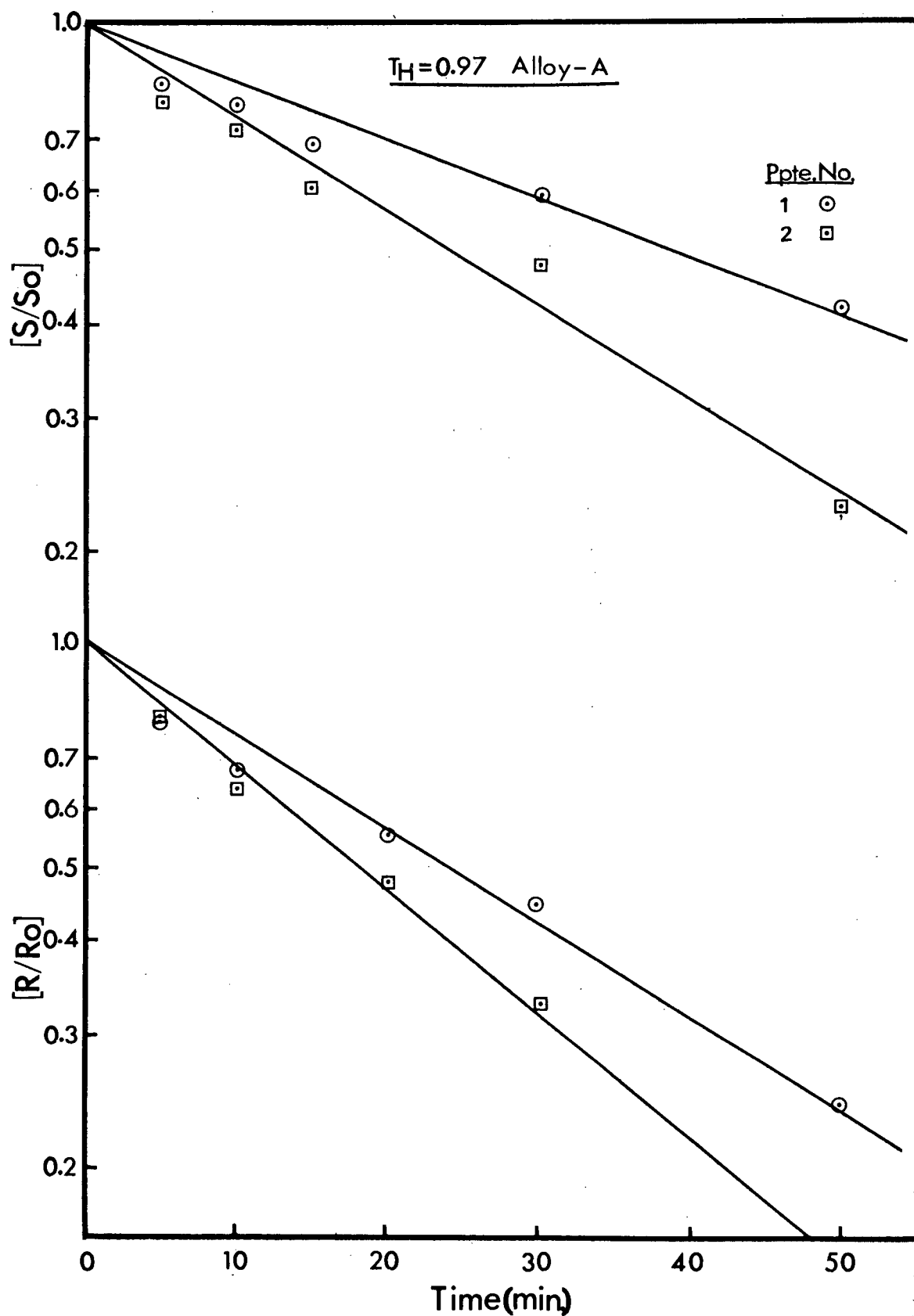


Figure 48. Log $[S/S_0]$ versus t and log $[R/R_0]$ versus t for alloy A at $T_H = 0.97$.

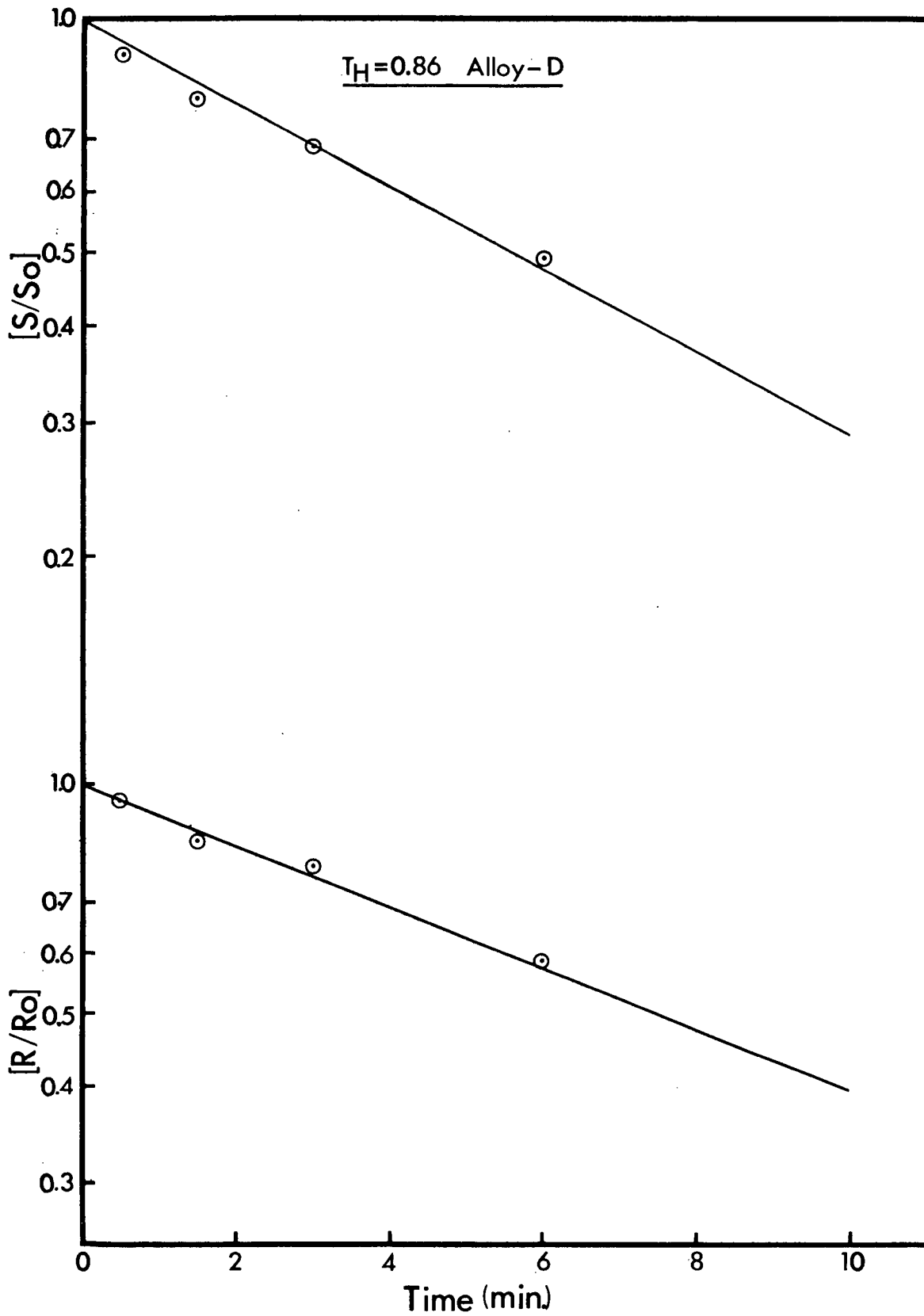


Figure 49. $\log [S/S_0]$ versus t and $\log [R/R_0]$ versus t for alloy D at $T_H = 0.86$.

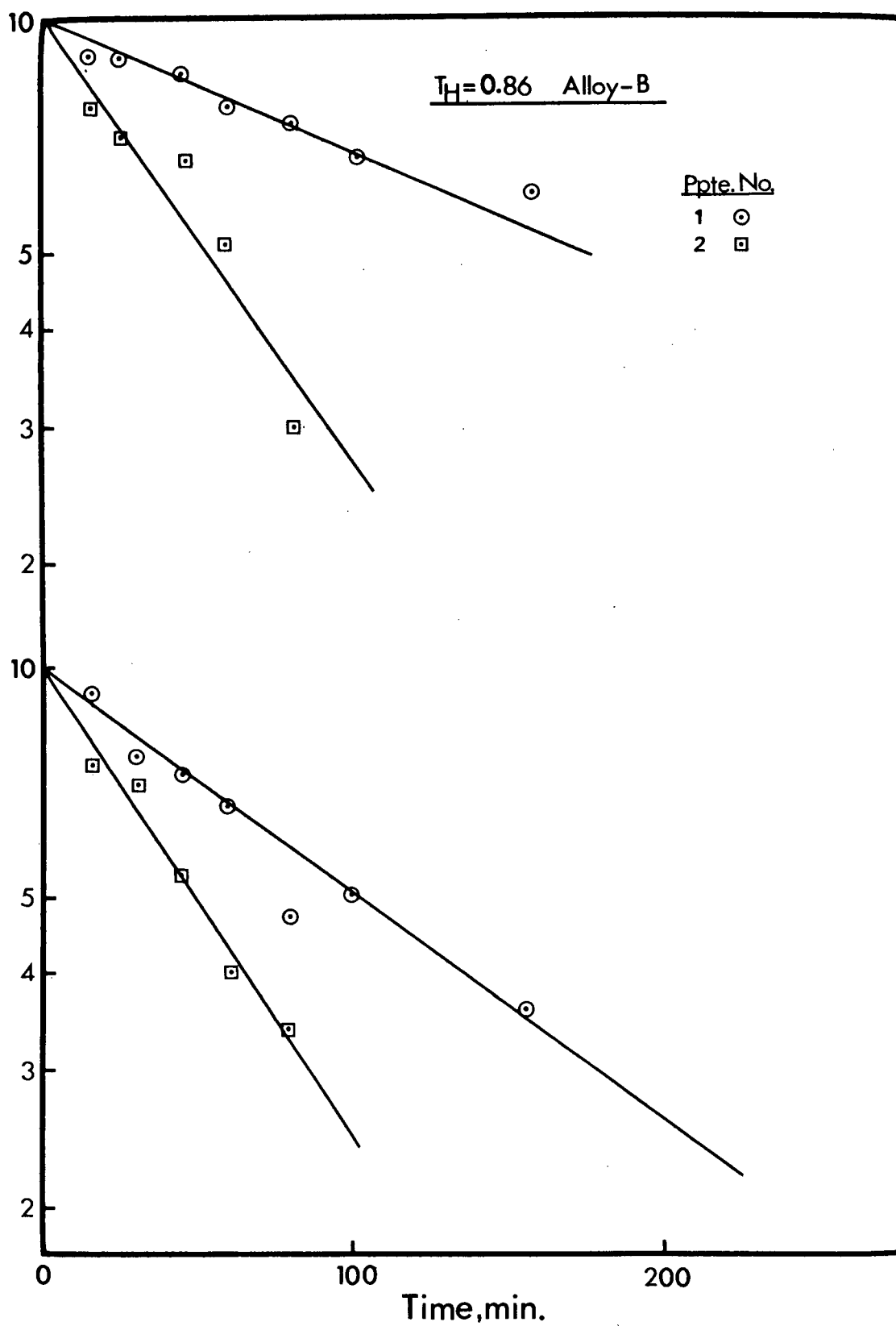


Figure 50. $\text{Log } [S/S_0]$ versus t and $\text{log } [R/R_0]$ versus t for alloy B at $T_H = 0.86$.

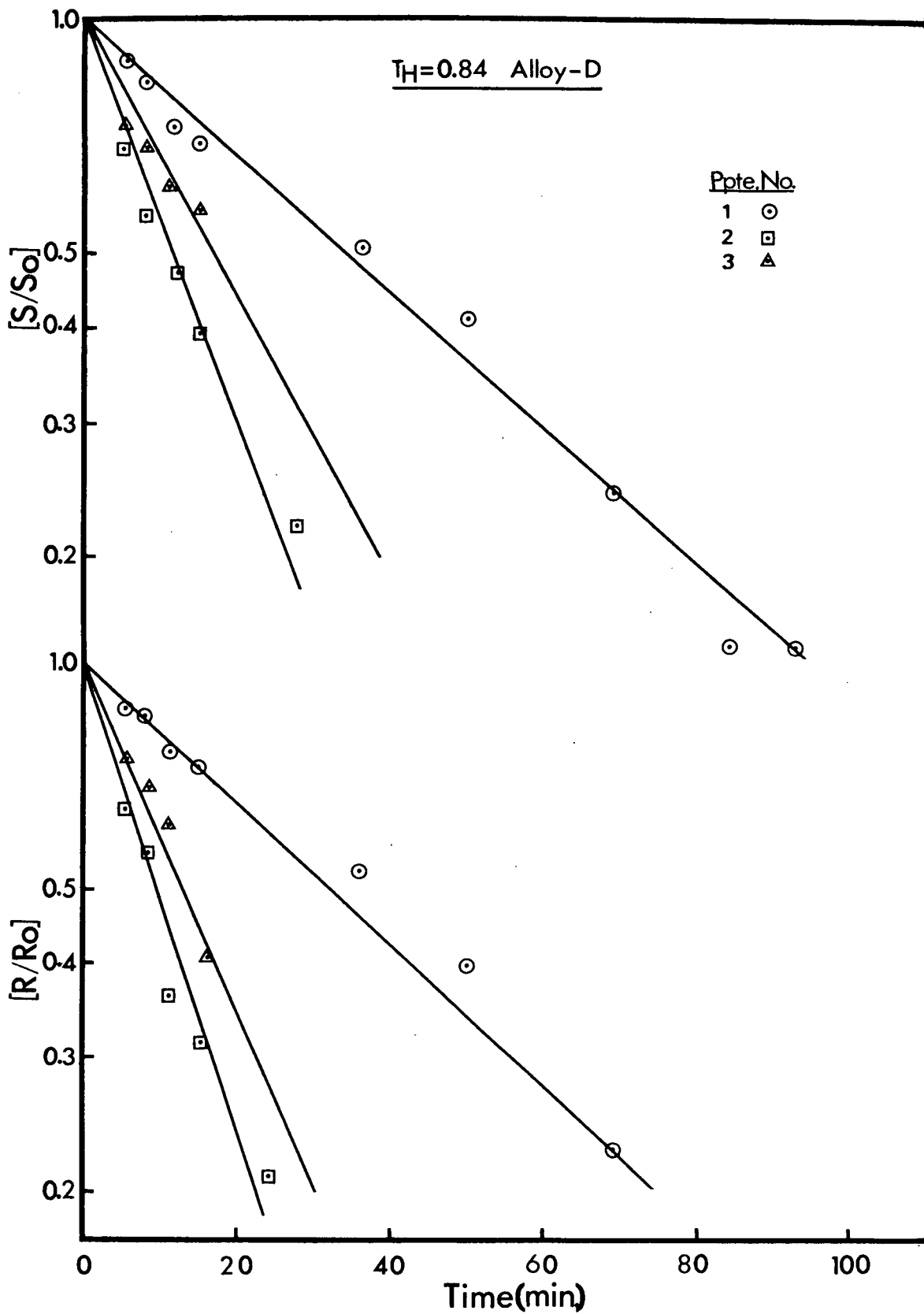


Figure 51. $\log [S/S_0]$ versus t and $\log [R/R_0]$ versus t for alloy D at $T_H = 0.84$.

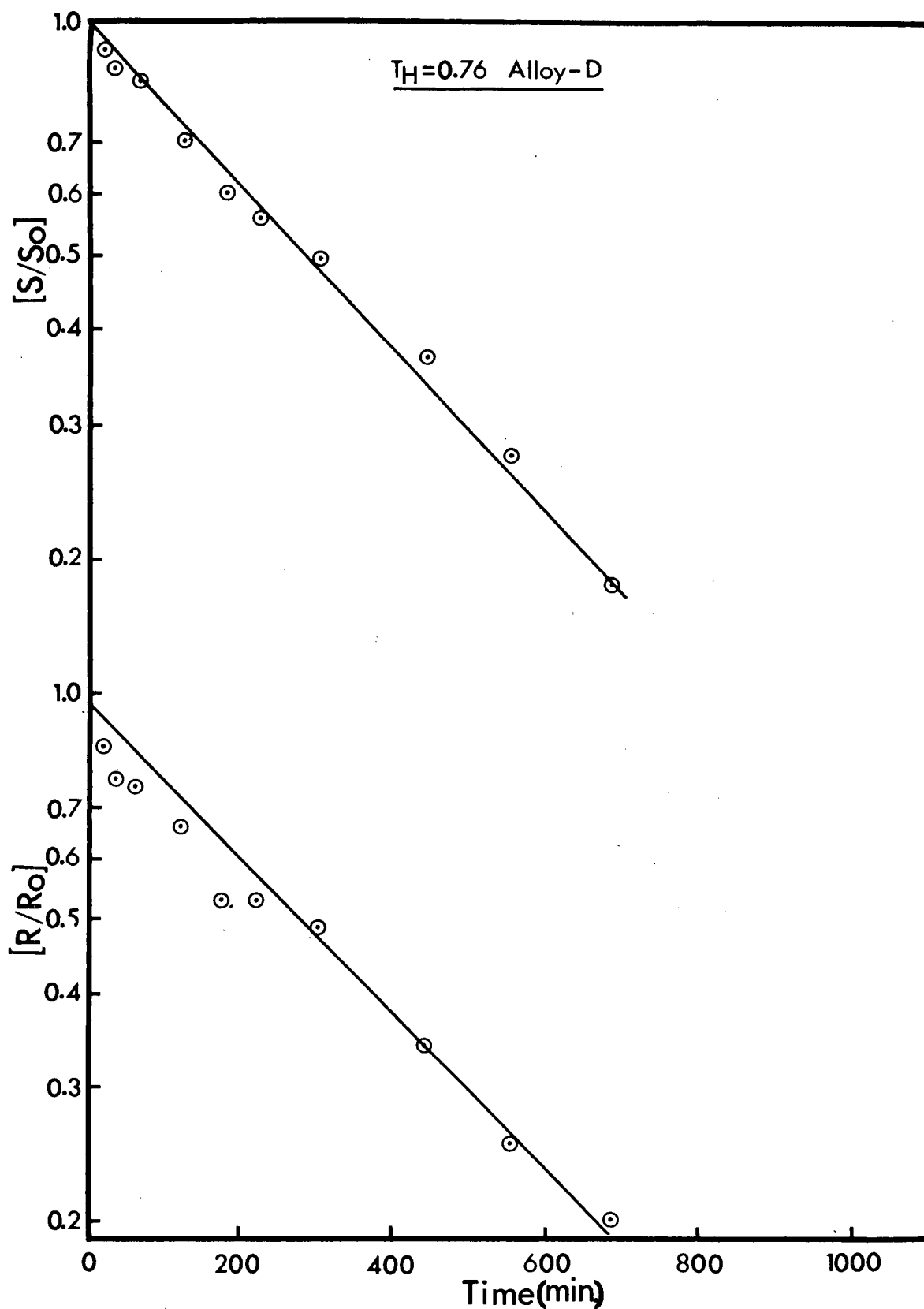


Figure 52. Log $[S/S_0]$ versus t and log $[R/R_0]$ versus t for alloy D at $T_H = 0.76$.

is valid for the change in half length.

In the following section, the observed exponential nature of the dissolution kinetics is rationalized on the basis of an analytical model which accounts for diffusion field impingement. The model assumes planar symmetry.

4.3 An Exponential Model for Planar Dissolution Kinetics

It was shown in section 3.4.1 that for the present experimental conditions, impingement of the diffusion fields occurs early in the dissolution process, before there is any significant movement of the interphase boundary. In view of this fact, it was decided to use an approximate solution to the diffusion equation for a finite system, assuming that the movement of the phase boundary can be neglected (i.e., the stationary interface approach is adopted).

The initial situation for this geometrical model is shown in Figure 53(a).

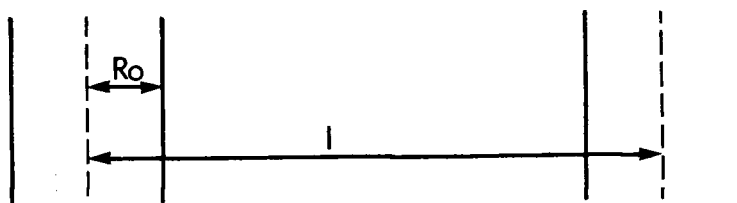


Figure 53(a) Geometrical model of a particle with half-thickness R_0 in a matrix with interparticle spacing l . where R_0 is the initial particle half thickness and l is the interparticle distance. It is assumed throughout this derivation that $R_0 \ll l/2$. The appropriate phase diagram is shown in Figure 53(b).

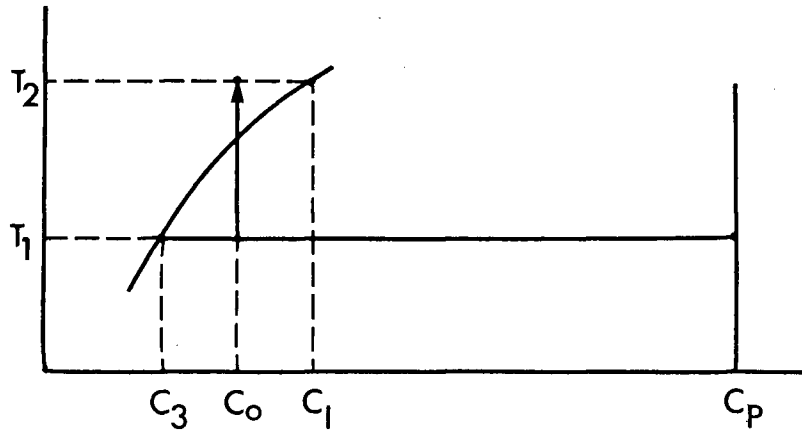


Figure 53(b) An appropriate phase diagram with growth of precipitates taking place at T_1 and dissolution at T_2 .

T_1 is the annealing temperature for growth and T_2 is the dissolution temperature. From the lever rule it follows that

$$\frac{R_o}{l/2} = \frac{C_o - C_3}{C_p - C_o} \quad 1$$

since the sample is assumed to be completely equilibrated at temperature T_1 (i.e., prior to upquenching to the dissolution temperature T_2).

Assume that the dissolution process has commenced at T_2 . Prior to impingement, the concentration distributions are as shown in Figure 53(c).

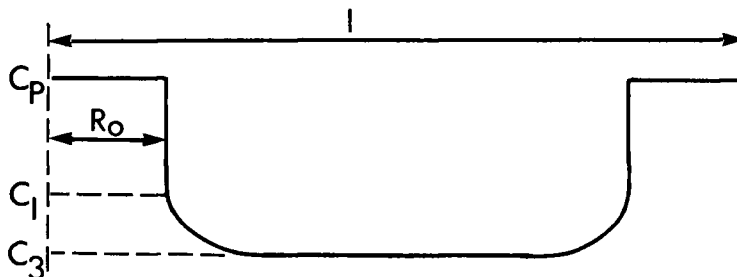


Figure 53(c) Dissolution profile prior to impingement.

During the impingement period, the distributions are as shown in Figure 54(a). Ultimately the alloy will have a uniform composition C_0 .

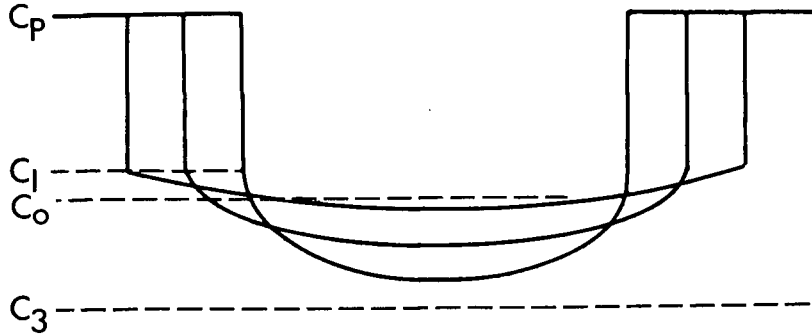


Figure 54(a) The concentration distributions during dissolutions after impingement takes place.

Hence the concentration at the centre of the impingement region ($\ell/2$) will gradually approach C_0 , but will attain it only after the second phase has completely disappeared and the concentration gradients in the matrix have been eliminated.

There exists no analytical solution to the diffusion equation for the impingement situation. Therefore an approximate solution is used in conjunction with the assumption that there is a constant concentration

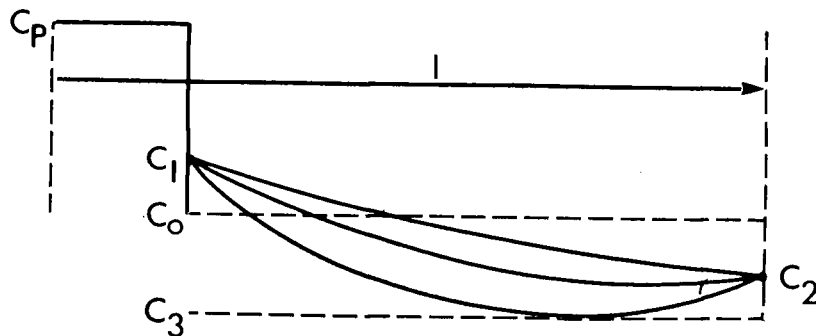


Figure 54(b) Schematic diagram of model used with a constant concentration C_2 , at $x = \ell$.

C_2 , at $x = \ell$, which over a reasonably long time period yields concentration contours near the interface which approximate those due to impingement as shown in Figure 54(b). A reasonable value for this concentration is

$$C_2 = 2C_o - C_I$$

as this yields a concentration of C_o (the bulk composition) at $\ell/2$ for infinite time. The present model is deficient in that it predicts a finite gradient at $\ell/2$ for all times, whereas there should be no flux across this point. However, it is emphasized that we are concerned with the gradients at $x = 0$ (the interface) and, therefore, the approximation should involve little error. The solution to the diffusion equation for a plate of thickness ℓ , faces of constant concentration C_I and $C_2 = 2C_o - C_I$, and an initial concentration C_3 is given in Crank⁵¹ (page 47). This solution involves a series expansion. For the present problem it is assumed that the leading term in this series dominates. This assumption requires that

$$e^{-\frac{n^2 D \pi^2 t}{\ell^2}} \ll 1 \quad (n = 2, 3, \dots) \quad 2$$

Under these conditions the solution is

$$C = C_I + 2(C_o - C_I)x/\ell - \frac{4}{\pi} (C_o - C_3) \sin \frac{\pi x}{\ell} e^{-\frac{D \pi^2 t}{\ell^2}} \quad 3$$

On differentiating and setting $x = 0$, one obtains

$$\left. \frac{\partial C}{\partial x} \right|_{x=0} = 2 \frac{(C_o - C_I)}{\ell} - 4 \frac{(C_o - C_3)}{\ell} e^{-\frac{D\pi^2 t}{\ell^2}} \quad 4$$

This gradient is substituted into the interface mass balance

$$-(C_p - C_I) \frac{dR}{dt} = -D \left. \frac{\partial C}{\partial x} \right|_{x=0} \quad 5$$

to give

$$-\frac{dR}{dt} = \frac{D}{\ell} \left[2 \frac{(C_I - C_o)}{(C_p - C_I)} + \frac{(C_o - C_3)}{(C_p - C_I)} \right] e^{-\frac{D\pi^2 t}{\ell^2}} \quad 6$$

The ratio $(C_I - C_o)/(C_p - C_I)$ is f_d , the supersaturation for dissolution (Figure 53(b)). In the second term the ratio

$$\frac{C_o - C_3}{C_p - C_I} \approx \frac{C_o - C_3}{C_p - C_o} \quad 7$$

since $C_p \gg C_I, C_o$ (i.e., for low supersaturation)

In view of Equation (1), it follows that

$$\frac{C_o - C_3}{C_p - C_I} \approx \frac{R_o}{\ell/2} \quad 8$$

Using Equation (8) and the definition of f_d , Equation 6 becomes

$$-\frac{dR}{dt} = \frac{D}{\ell} \left[2f_d + \frac{8R_o}{\ell} e^{-\frac{D\pi^2 t}{\ell^2}} \right] \quad 9$$

This is integrated from $t = 0$ ($R = R_o$) to $t(R)$, to give

$$R_o - R = \frac{2Df_d t}{\ell} - \frac{8R_o}{\pi^2} \left(e^{-\frac{\pi^2 D t}{\ell^2}} - 1 \right) \quad 10$$

Assuming $8/\pi^2 \approx 1$, Equation 10 becomes

$$R = R_o e^{-\frac{\pi^2 D t}{\ell^2}} - 2 \frac{D f_d t}{\ell} \quad 11$$

If one substitutes values of the parameters D , t , ℓ and f_d which are typical of the present experimental conditions, it is found that the linear term $\frac{2Df_d t}{\ell}$ only becomes important in the later stages of dissolution (see Figure 55). Thus for a considerable (intermediate) portion of the dissolution period the kinetics should follow the equation

$$R = R_o e^{-\frac{\pi^2 D t}{\ell^2}}$$

$$\text{i.e.} \quad \ln R/R_o = -\frac{\pi^2 D t}{\ell^2} \quad 12$$

which is in agreement with the experimental results (Figures 48-52).

An attempt was made to generalize the above treatment to spherical symmetry.

Unfortunately, in order to obtain an equation of the same form as

Equation (12), so many assumptions were required that the derivation

was lacking in analytical rigor and was therefore deemed unacceptable.

It was felt that it would be worthwhile to check the validity

of the exponential relationship with dissolution kinetics obtained by

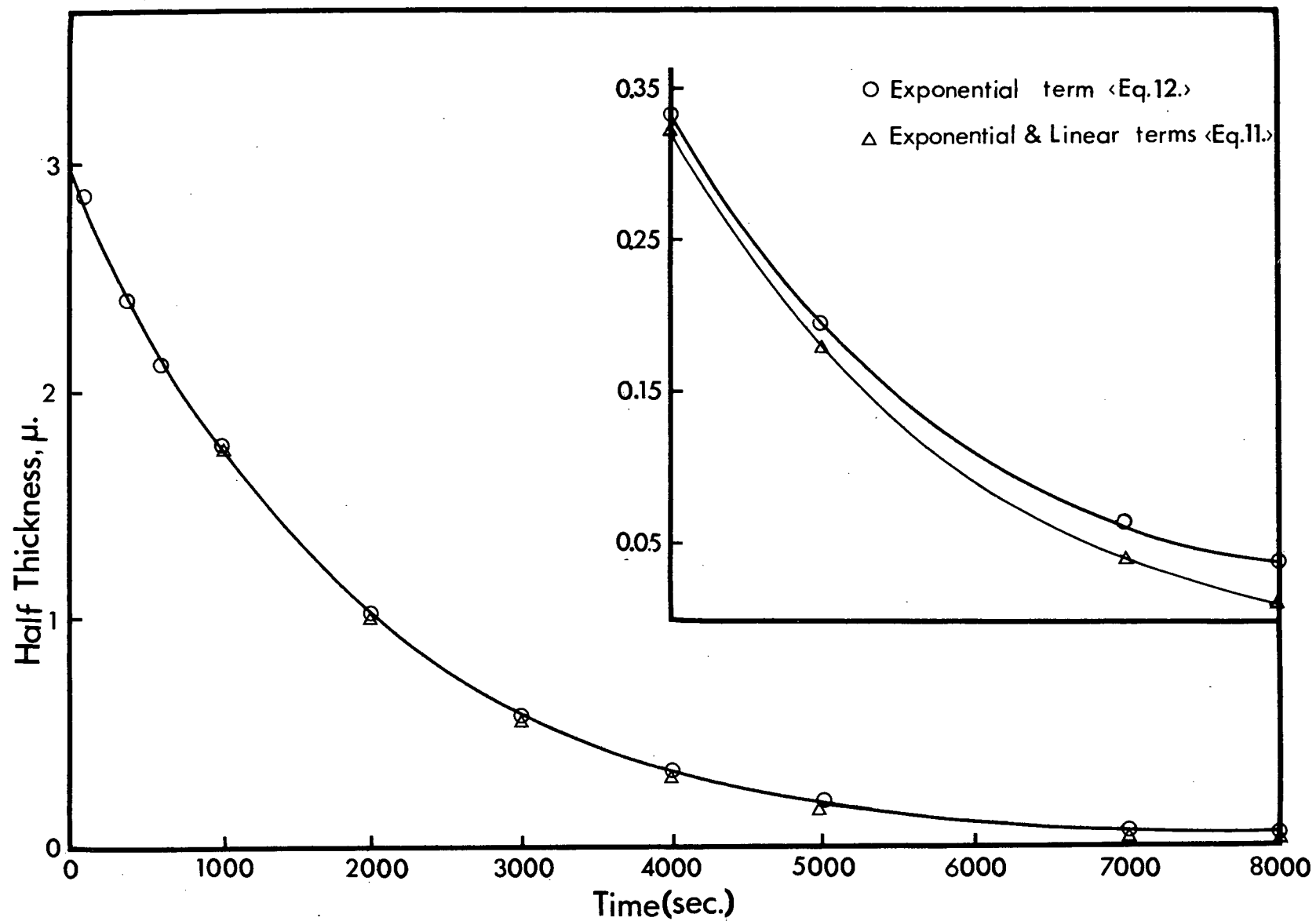


Figure 55. R versus t for equations 11 and 12.

Baty et al.⁵² They used a statistical method to follow the dissolution of CuAl_2 precipitates in an Al-4wt.% Cu system at 520°C. Using their data, a plot of $\log R/R_0$ versus t is shown in Figure 56 and a reasonably linear fit is obtained. Further support for the exponential model is shown in Figure 57 where the numerically calculated solution by Tanzilli and Heckel²⁵ for dissolution of planar precipitates in a finite system is plotted in logarithmic form. The supersaturation ($k = 0.22$) is much greater in this instance than for most of the present experimental work. Equation 12 was derived using a stationary interface assumption, the reliability of which increases with decreasing supersaturation. That a reasonably linear fit was obtained from the numerically derived solution which involves a relatively high supersaturation is very encouraging. The experimental results obey the exponential relationship as established in Equation 12, for the whole range of homologous temperatures observed. The greatest deviation from linearity in the plots of $\ln R/R_0$ versus t is in most cases found during the early stages of dissolution, before impingement. This is to be expected as the model does not account for dissolution kinetics prior to impingement.

The values of D_v calculated using equation 12 are consistently higher than the literature values as may be seen in Figure 58. All other things being equal, the dissolution rate of a curved surface is faster than that of a planar surface. The surfaces of the allotriomorphs are in fact curved. Thus the application of a planar dissolution model to the dissolution of a curved surface will of necessity yield D_v values which are higher than the actual values. Furthermore the omission of the

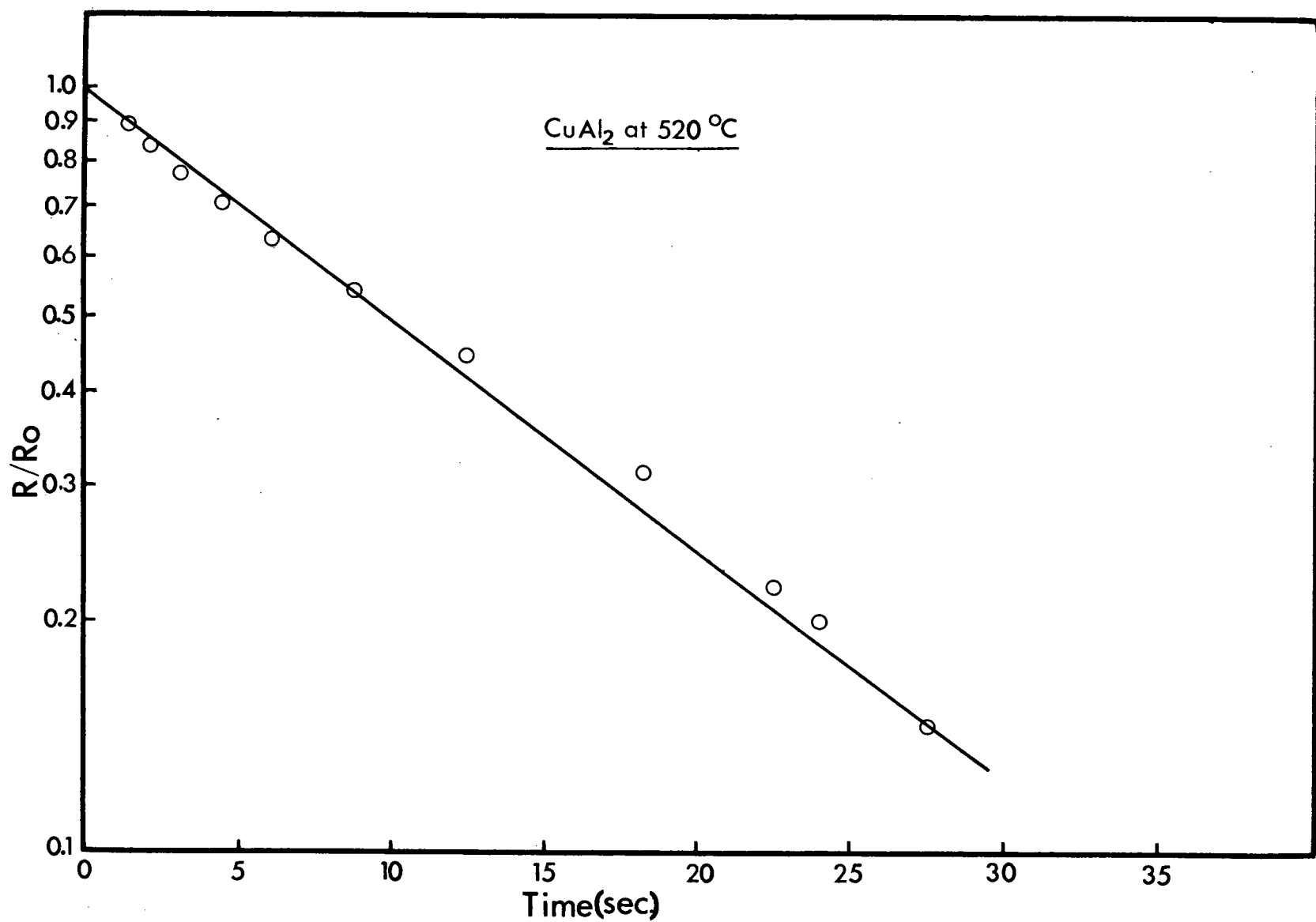


Figure 56. Log $[R/R_0]$ versus t for dissolution of precipitates in an Al-4 wt.% Cu system at 520°C.

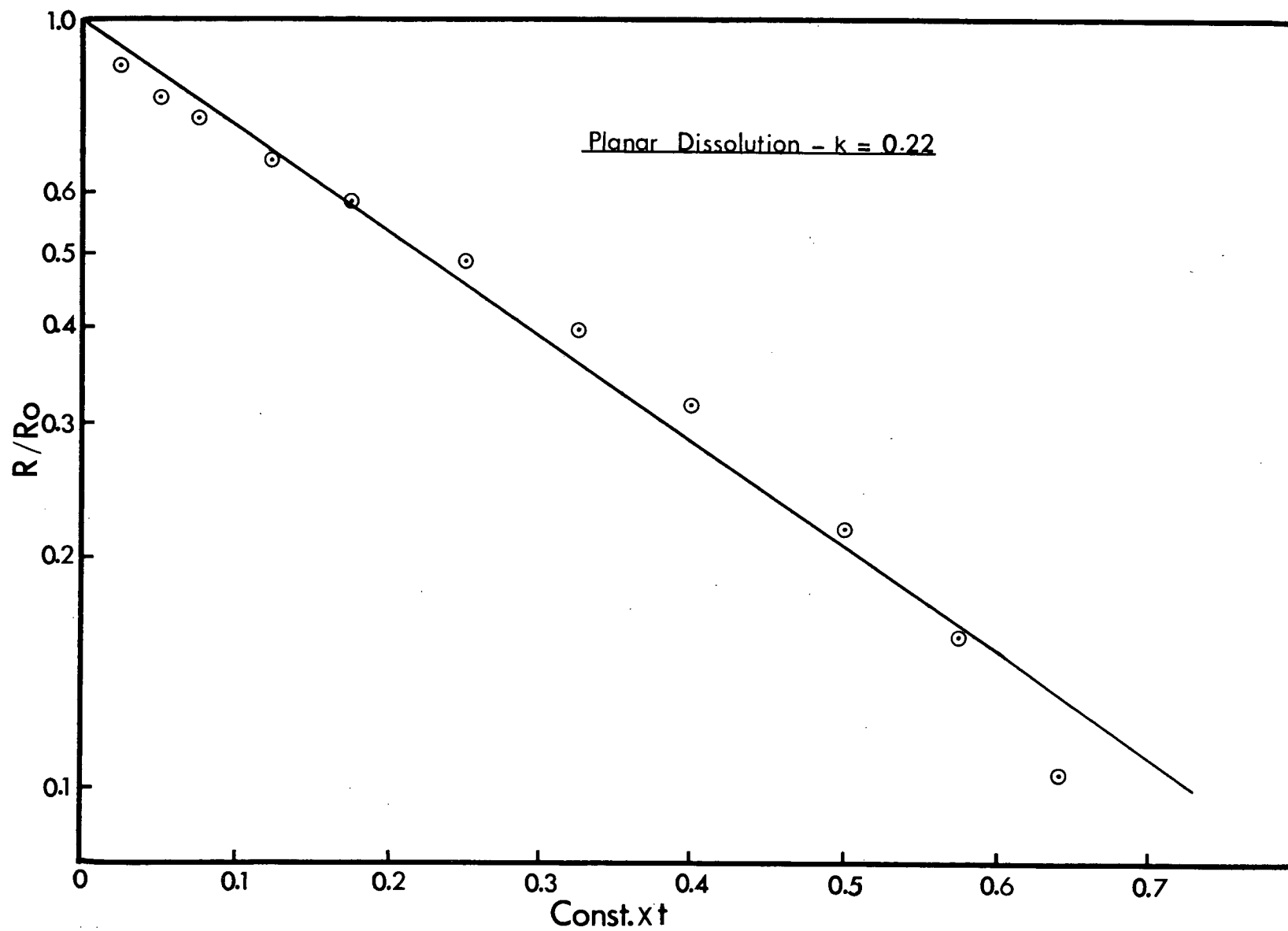


Figure 57. $\text{Log } [R/R_0]$ versus t for the dissolution of planar precipitate in a finite system with $k = 0.22$.

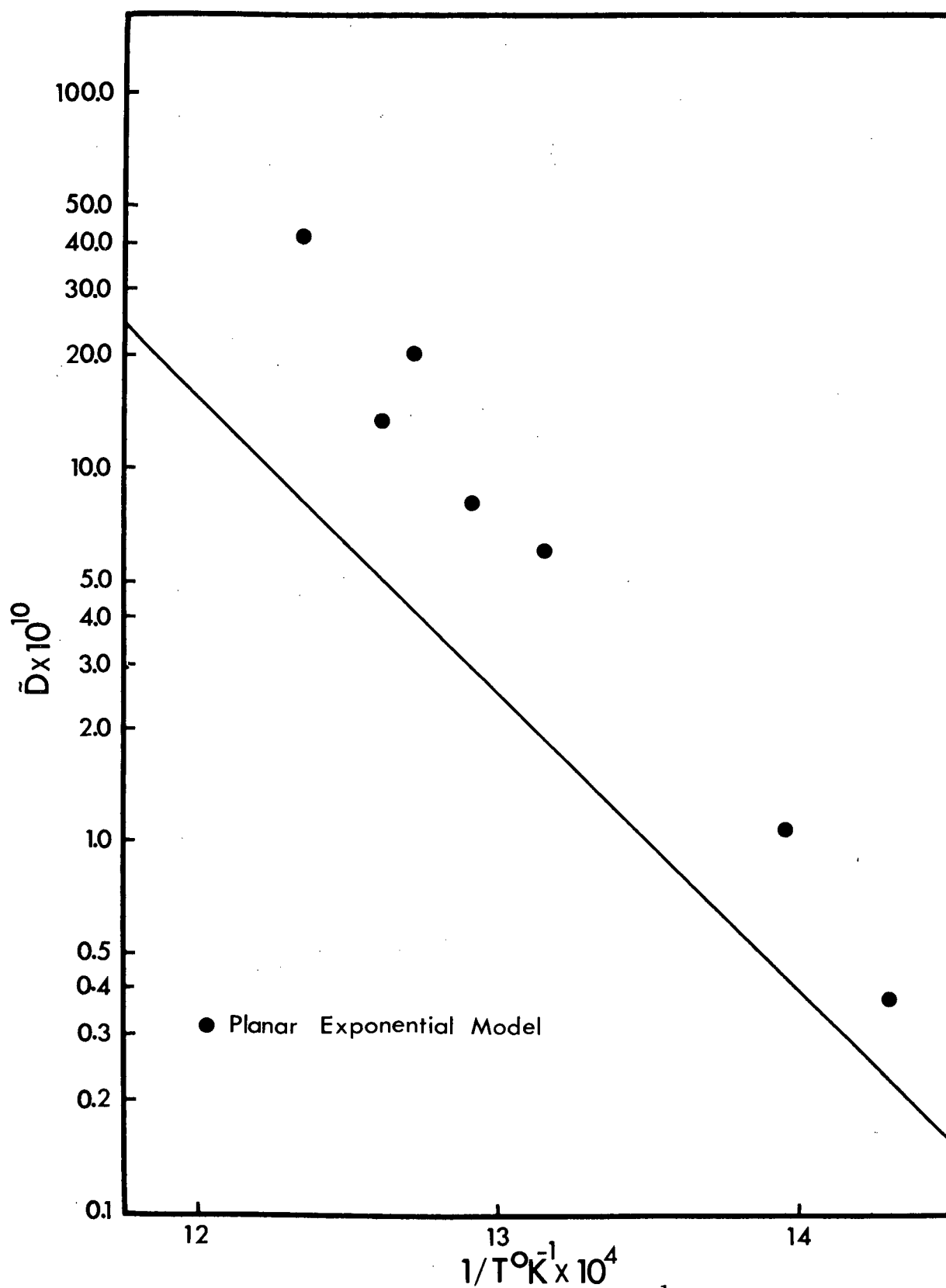


Figure 58. Arrhenius plot of D_v versus $1/T^\circ K^{-1}$ for the kinetic results.

linear term $(2 \frac{D_f t}{\ell^2})$ in the final form of the exponential equation (equation 12) will also result in higher calculated D_V values.

Finally, any surface diffusion effect present will increase the observed D_V value. It should be noted, however, that a surface diffusion effect if present would become more important at lower temperatures tending to give higher $[D_V^{\text{calculated}}/D_V^{\text{literature}}]$ ratios at low homologous temperatures. If anything the results show the opposite trend.

4.4 Precipitate Shape Change During Dissolution

In general it was observed that a constant axial ratio S/R was not maintained during dissolution. Indeed, in certain cases the final axial ratio, S_F/R_F , was significantly different from the initial axial ratio, S_O/R_O . The present section deals with this observed change in axial ratio. Figures 59-63 are examples of situations in which

$$S_O/R_O \approx S_F/R_F, \quad S_O/R_O > S_F/R_F \text{ and } S_O/R_O < S_F/R_F$$

It was shown in Section 3.4 that the shape of the concentration profiles during dissolution and hence the mode of dissolution, for a certain homologous temperature is independent of supersaturation.

Figure 64 is a plot of supersaturation versus the fraction (F) of precipitates in a given experiment showing an increase in axial ratio of greater than 10%, i.e., the fraction of precipitates for which

$$\frac{(S_F/R_F)}{(S_O/R_O)} > 1.1$$

This procedure is crude for several reasons.

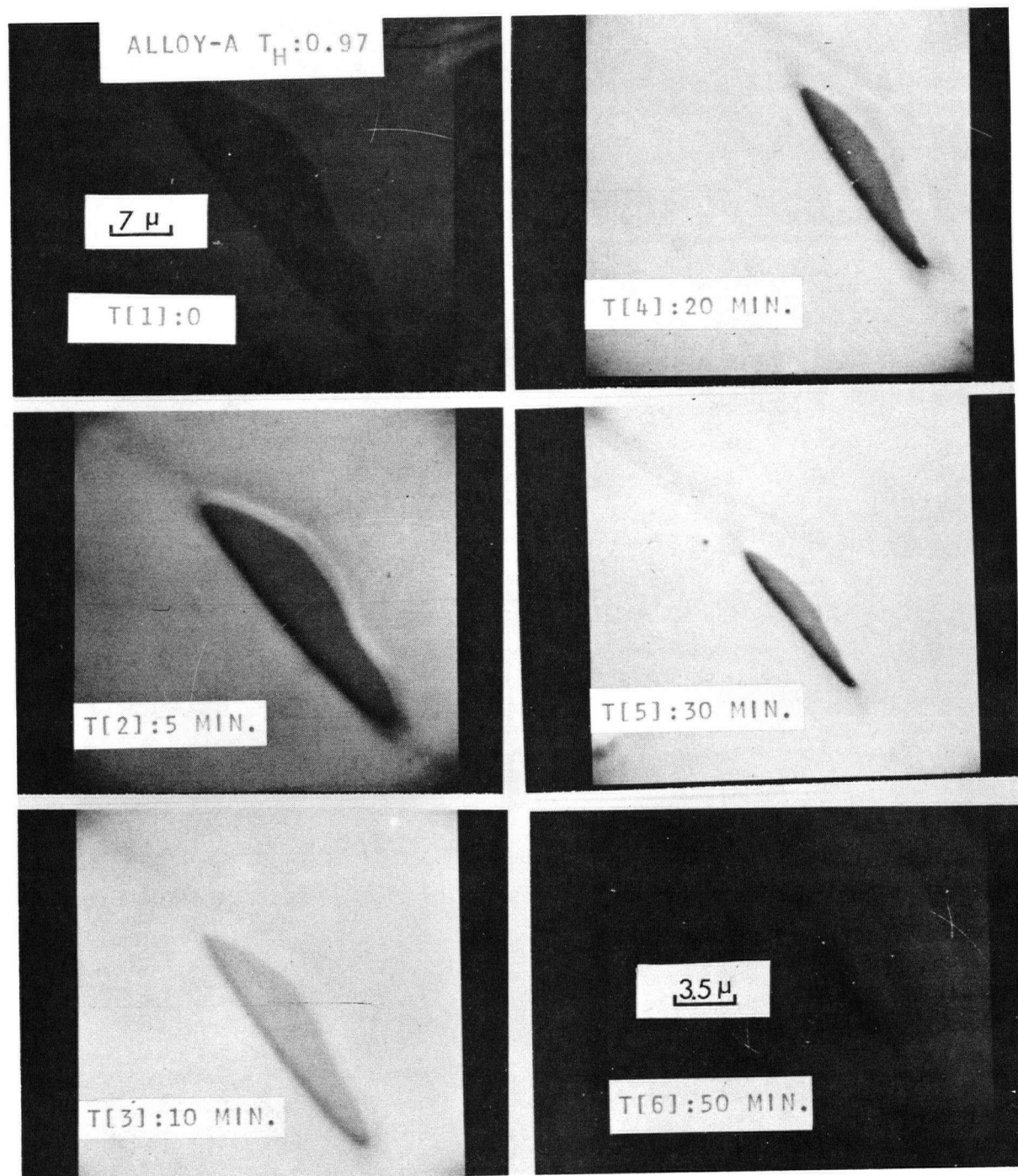


Figure 59. Back scattered electron image micrographs, used to observe the dissolution kinetics of an allotriomorph at $T_H = 0.97$ for alloy A.

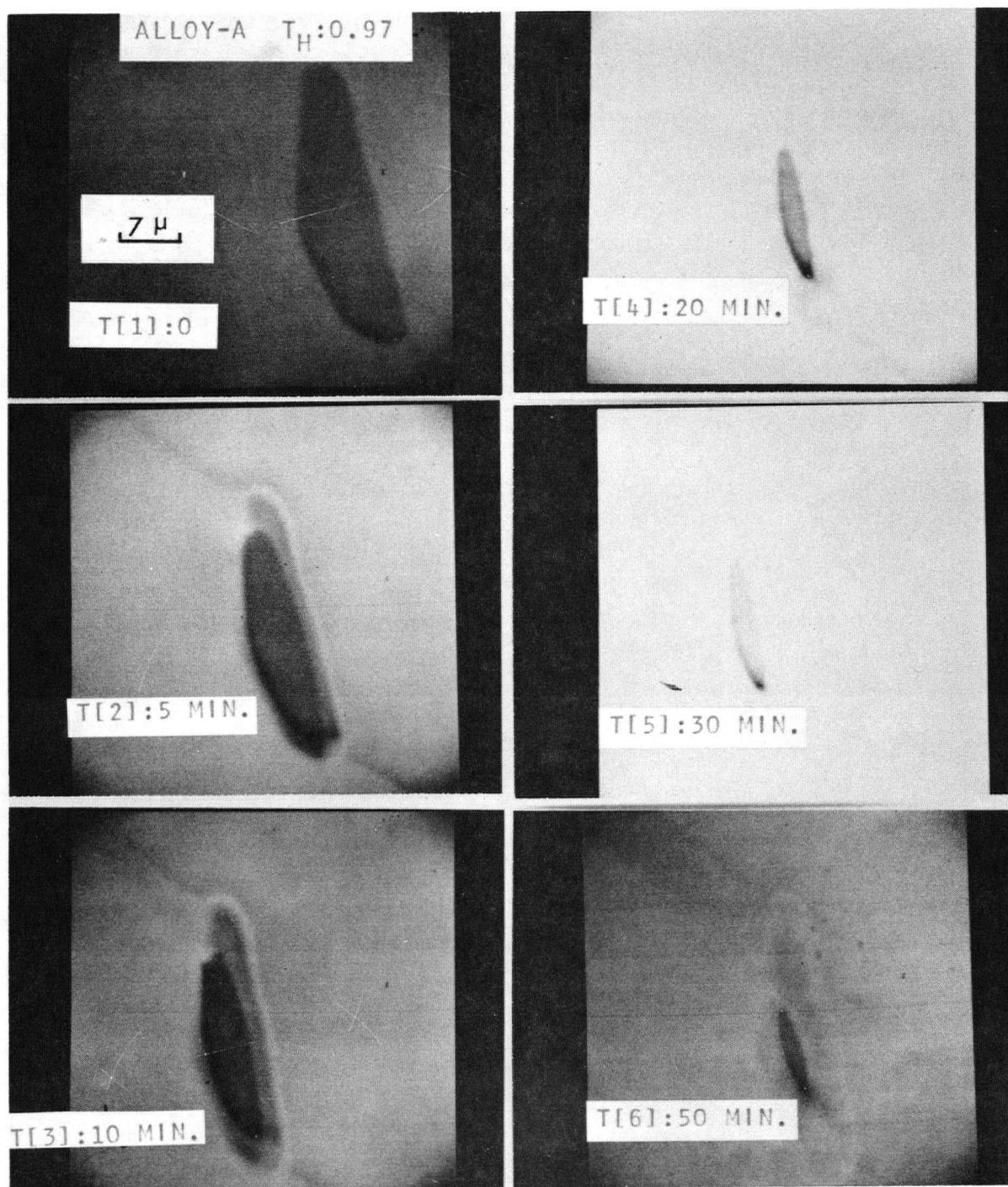


Figure 60. Back scattered electron image micrographs, used to observe the dissolution kinetics of an allotriomorph at $T_H = 0.97$ for alloy A.

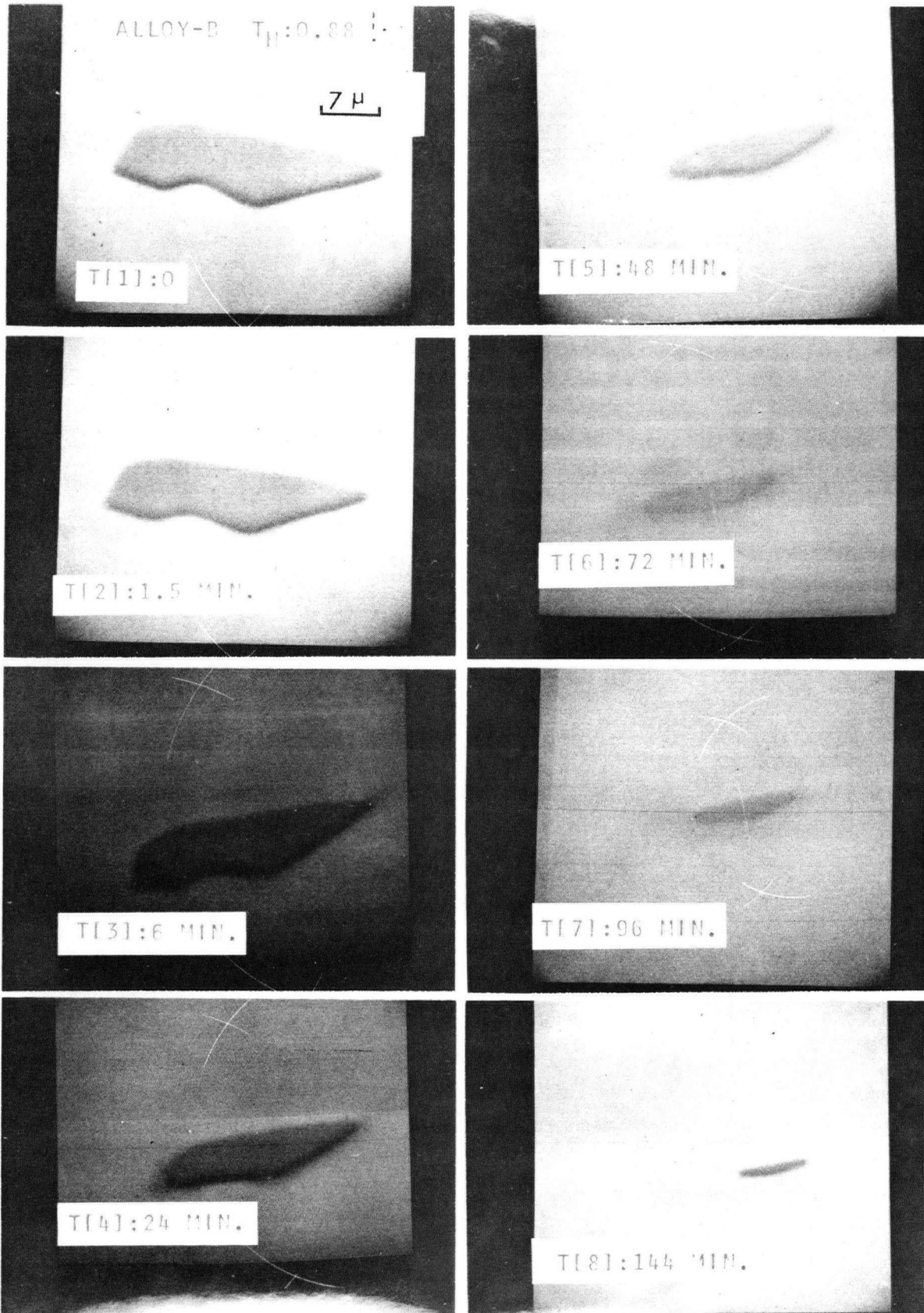


Figure 61. Back scattered electron image micrographs, used to observe the dissolution kinetics of an allotriomorph at $T_H = 0.88$ for the Al-Ag alloy.

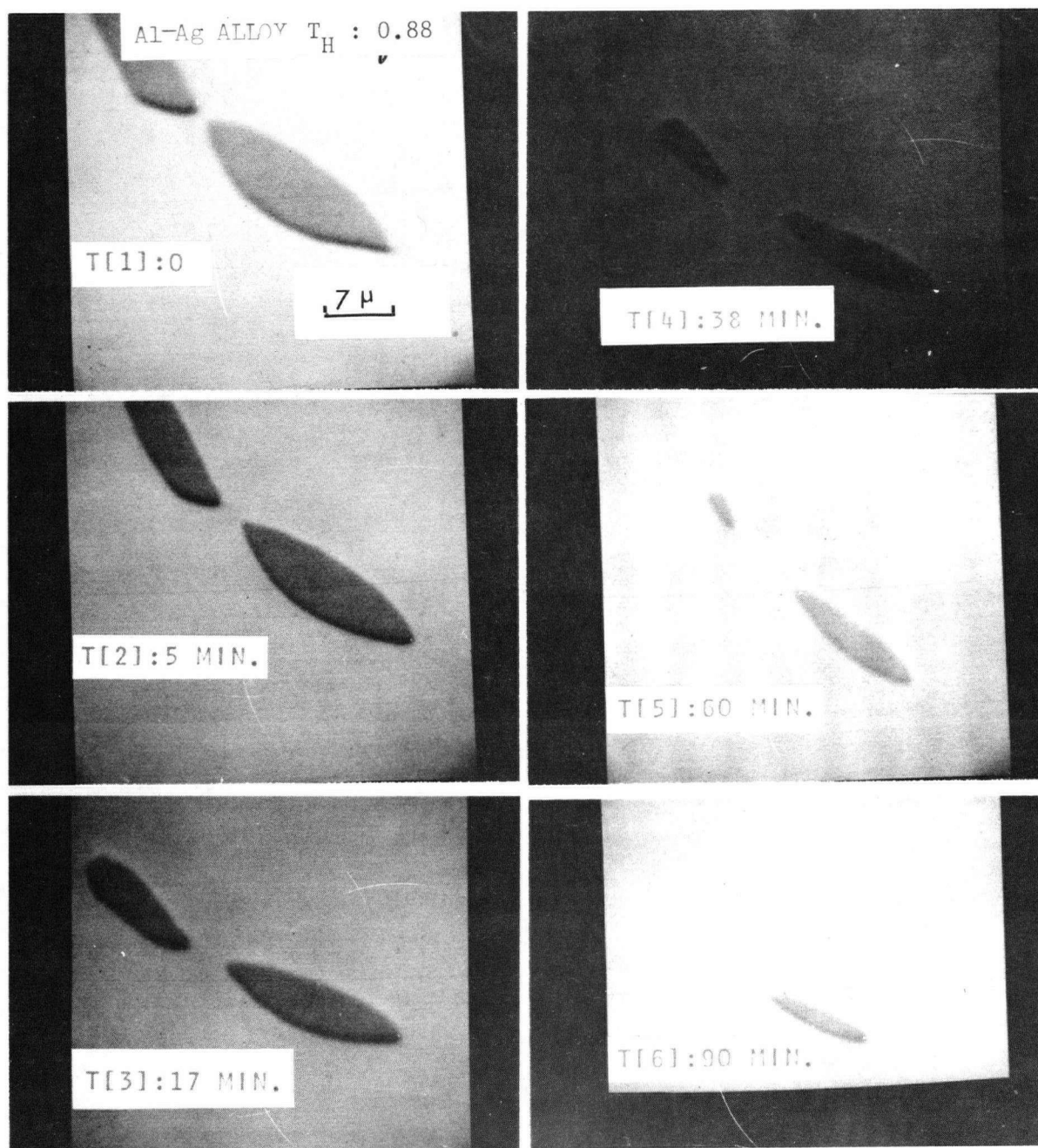


Figure 62. Back scattered electron image micrographs, used to observe the dissolution kinetics of an allotriomorph at $T_H = 0.88$ for alloy B.

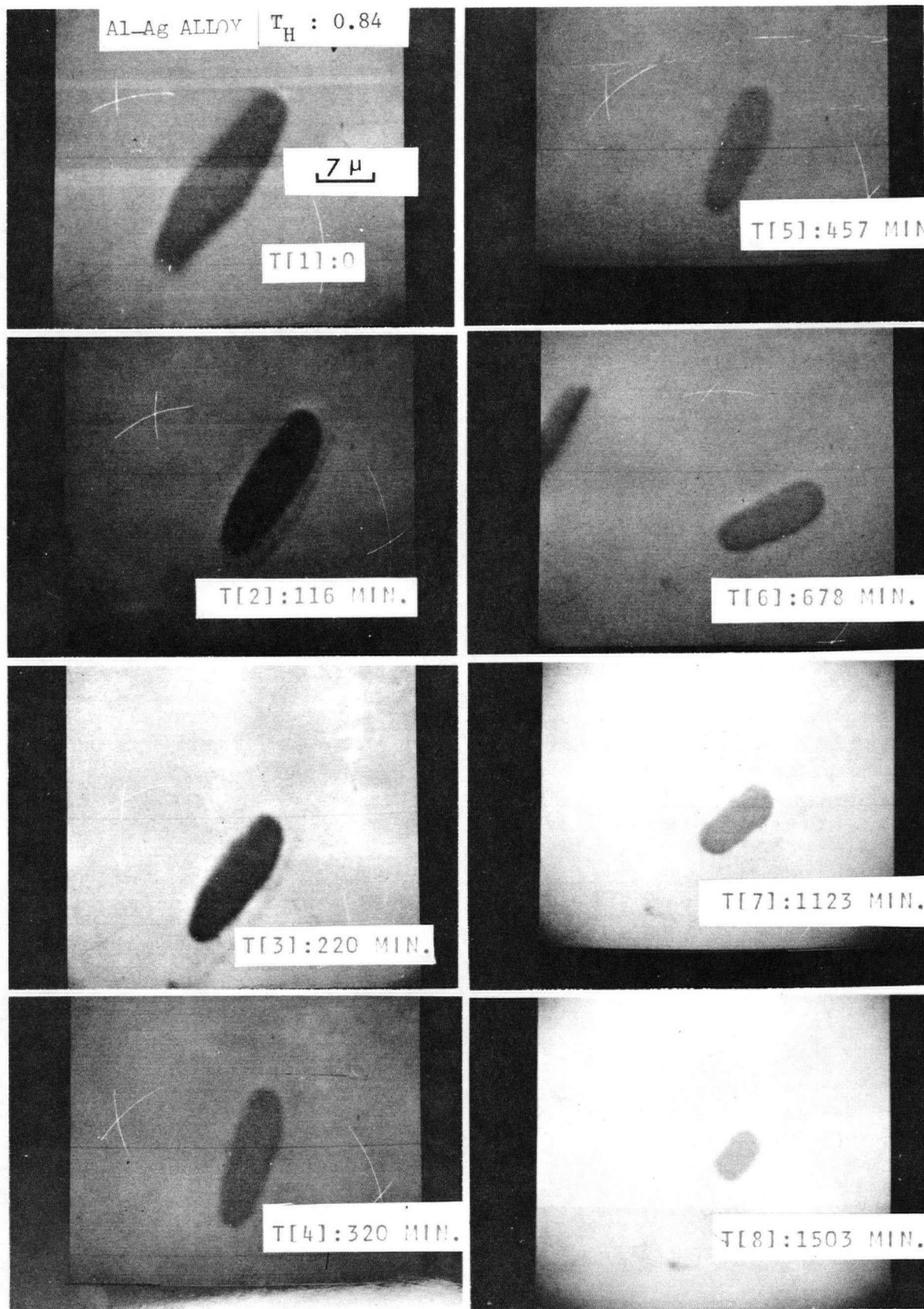


Figure 63. Back scattered electron image micrographs, used to observe the dissolution kinetics of an allotriomorph at $T_H = 0.84$ for the Al-Ag alloy.

1. The use of 10% as the fiducial axial ratio increase is admittedly arbitrary.

2. The comparison is made on the basis of the last axial ratio measurement taken. However, there may have been further changes in axial ratio before the precipitate completely dissolves. This however could not be observed due to the resolution of the technique used.

3. The number of precipitates studied in any experiment was typically 3-10, which is insufficient for unquestionably meaningful statistical studies. In spite of these deficiencies Figure 64 indicates that at a given T_H , the change in axial ratio is independent of supersaturation which is in agreement with the concentration contour studies.

In Figure 65 the same function (F), as in Figure 64, is plotted versus the homologous temperature. This plot shows a definite increase in F with increasing homologous temperature. At high homologous temperatures, $T_H > 0.95$, all the precipitates studied show an increase in their axial ratio during dissolution (see Figures 59 and 60). About half of the precipitates examined at $0.95 > T_H > 0.80$ show an increase in axial ratio and at low homologous temperatures $T_H < 0.80$ the precipitates either show no change or else a slight decrease in axial ratio (see Figure 63). These observations can be explained in the following manner.

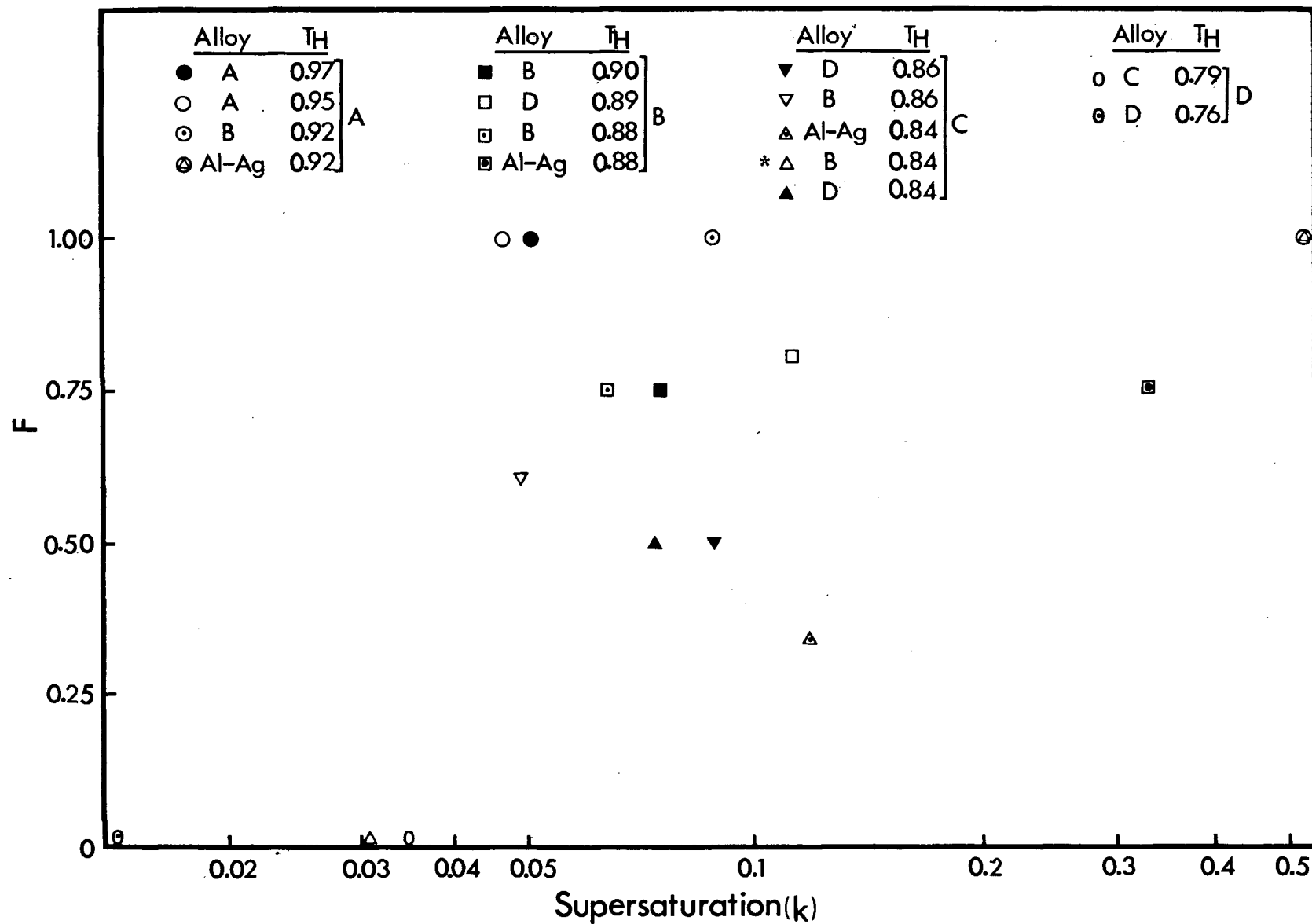


Figure 64. Fraction of precipitates showing an increase in axial ratio greater than 10% (F) versus supersaturation (k). * Dissolution experiment below the solvus, resulted in spheroidisation (see Figure 70).

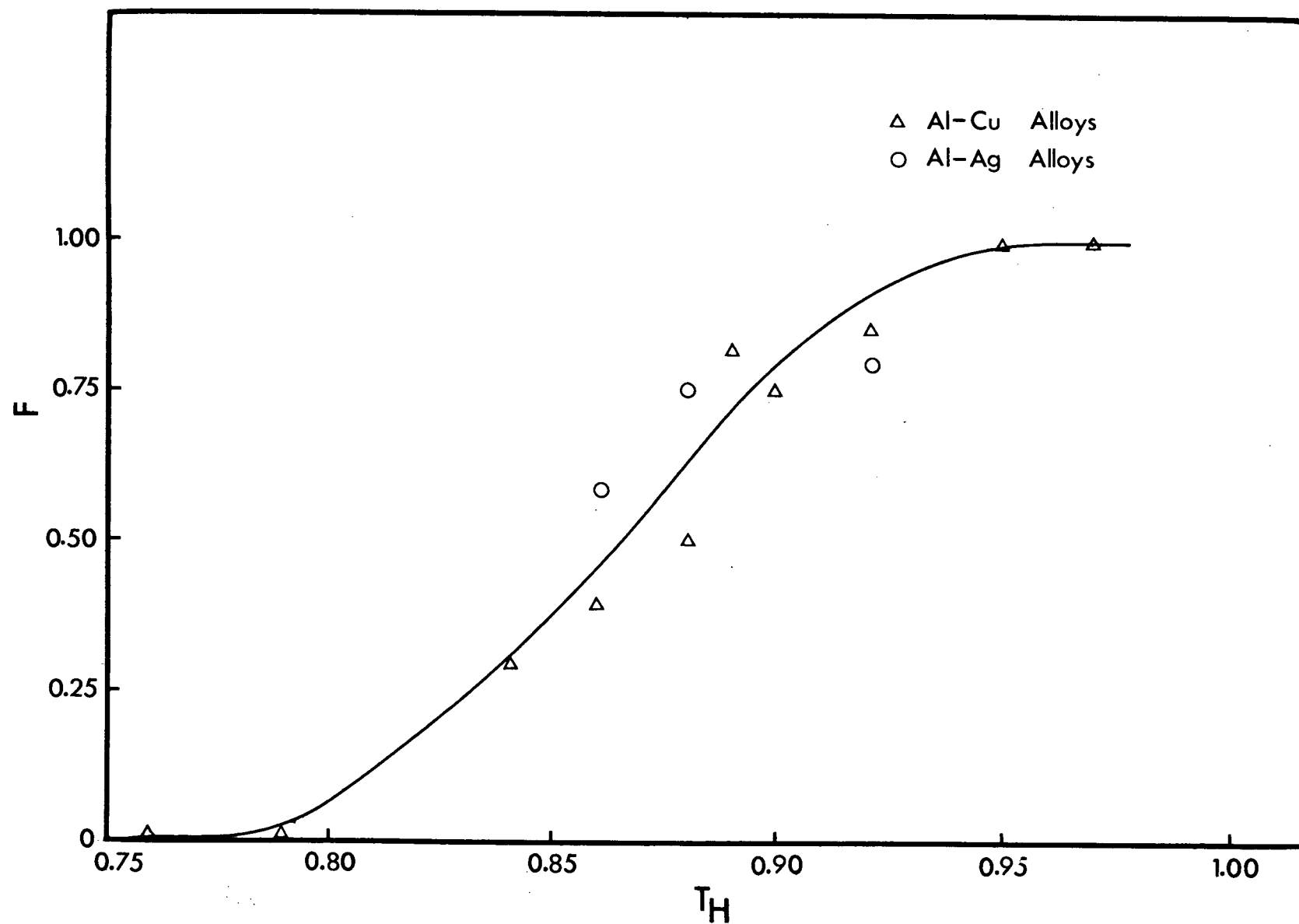


Figure 65. Fraction of precipitates showing an increase in axial ratio greater than 10% (F) versus T_H .

4.4.1 High Homologous Temperatures

At high homologous temperatures ($T_H > 0.92$), the contribution of grain boundary diffusion to the dissolution process may be neglected and the precipitate may be considered to be an oblate spheroid dissolving by volume diffusion into the matrix. Figure 66(a) is a schematic diagram of the distribution of precipitates with an axial ratio of approximately 4 to 1 and an interparticle spacing of $L = 10 \times R_0$. These values are consistent with most of the experimental work. Figure 66(b) gives a schematic representation of the concentration fields around these precipitates during the initial stages of dissolution. Because only bulk diffusion contributes, these contours are confocal spheroids. In view of the fact that a particular precipitate particle has a symmetrical distribution of other particles about it, it is reasonable to assume that the diffusion field from surrounding precipitates has approximately spherical symmetry as shown in Figure 66(c).

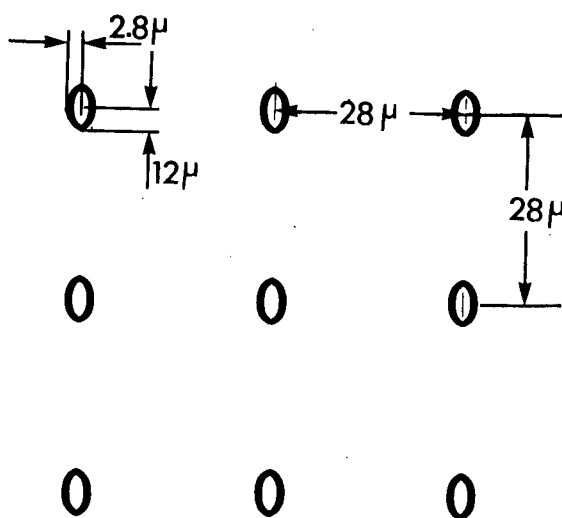


Figure 66(a) Symmetrical distribution of precipitates with $[S_0/R_0] = 4$.

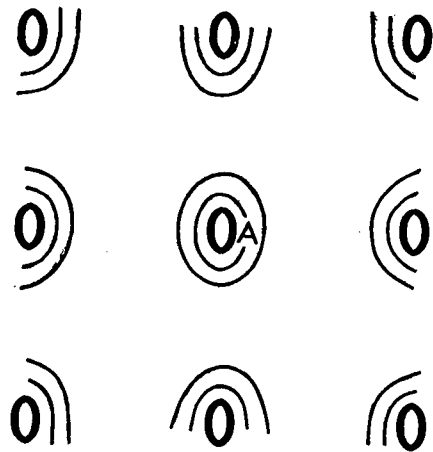


Figure 66(b) Schematic representation of concentration fields around a symmetrical array of precipitates.

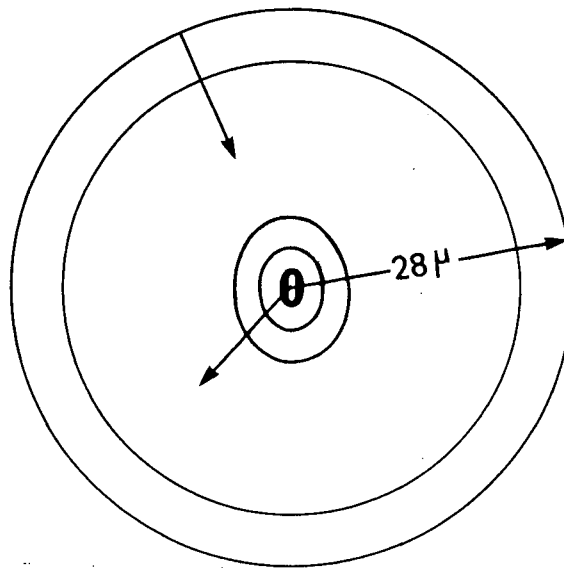


Figure 66(c) Diagram of spherically symmetrical field surrounding a grain boundary allotriomorph.

However, even if one assumes a random distribution of precipitates about any one precipitate, the diffusion field from these latter precipitates is on the average radially symmetrical with respect to the precipitate in question. Accordingly, as a crude approximation the concentration contours arising from neighbouring precipitates can be "smeared" into confocal spherical contours with respect to the precipitate in question. Figure 66(c) shows clearly that impingement first

takes place at the tip rather than the faces of the allotriomorph. The tips are therefore expected to dissolve more slowly resulting in an increase in S/R .

Because the precipitates in question are grain boundary allotriomorphs, the assumption of a random distribution of precipitates about a particular precipitate is open to question. However, any asymmetry would be due to the presence of a number of precipitates on the same grain boundary being in closer proximity to the precipitate under observation than the Widmanstätten plates in the adjacent matrix. Such a distribution will further enhance the likelihood of impingement first taking place in the equatorial plane (i.e., the plane of the grain boundary). The impingement profile is assumed to be a superposition of the confocal spheroids of the central precipitate and the surrounding spherical field (see Appendix VII for details). Figure 67 gives the calculated profiles after 500 seconds. Significant interaction of the diffusion fields in the equatorial plane is evident. In Figure 68(a) it can be seen that on section Ob (from Figure 67), which is along the minor axis, the diffusion field adjacent to the precipitate is hardly affected by diffusion inward from the spherical field (i.e., from the adjacent precipitates). In Figure 68(b), however, the magnitude of the gradients in section Oa, which is the equatorial plane, are reduced significantly by diffusion inward from the spherical surface. The concentration contours will not actually be confocal spheroids but will have somewhat higher axial ratio. This will result in impingement along the equator at earlier times and will tend to accentuate the above effect.

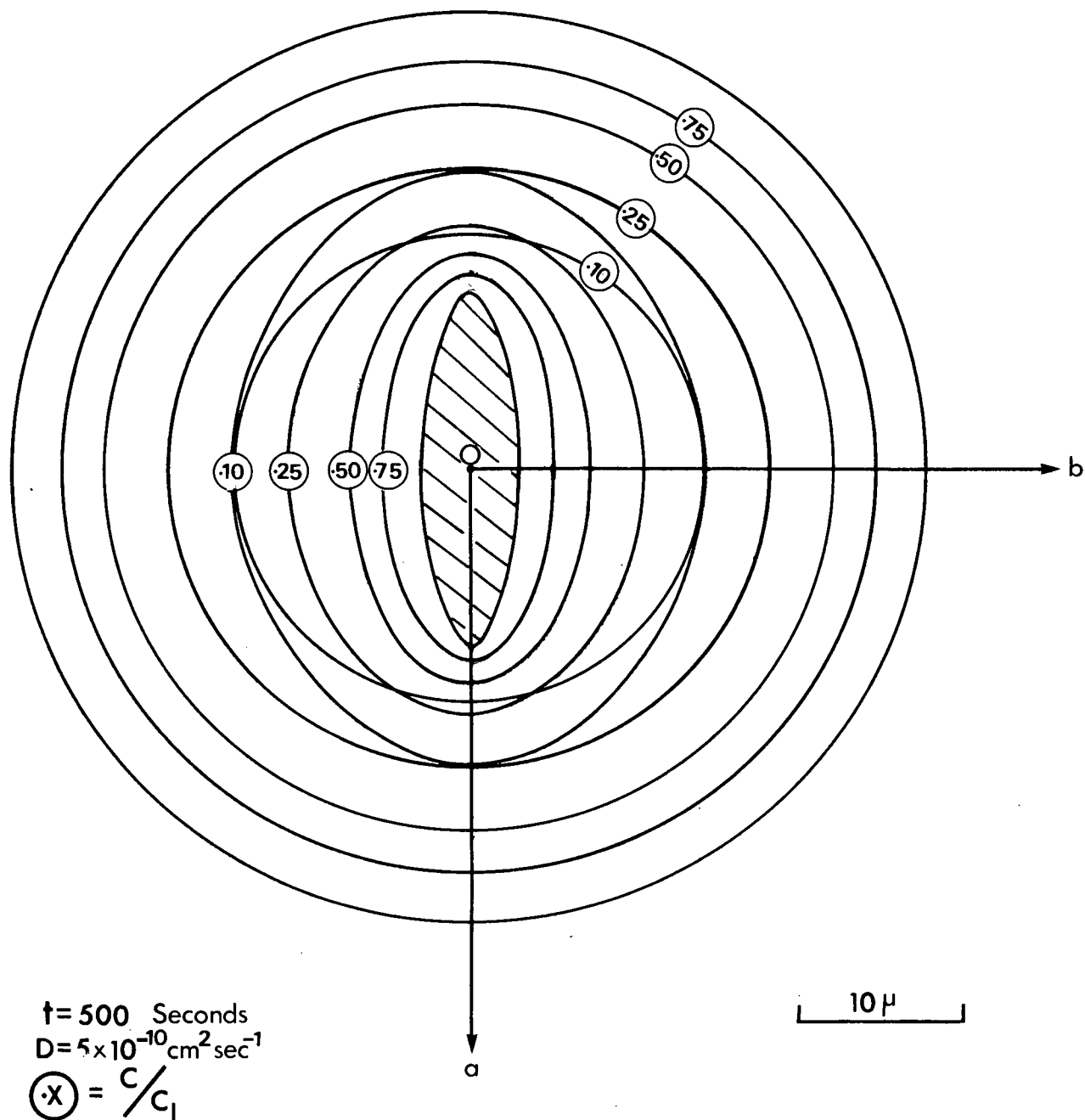


Figure 67. The resulting impingement between the confocal spheroid isoconcentration contours about an allotriomorph and the contours of the surrounding spherical field after $t = 500$ seconds for various $[c/c_I]$.

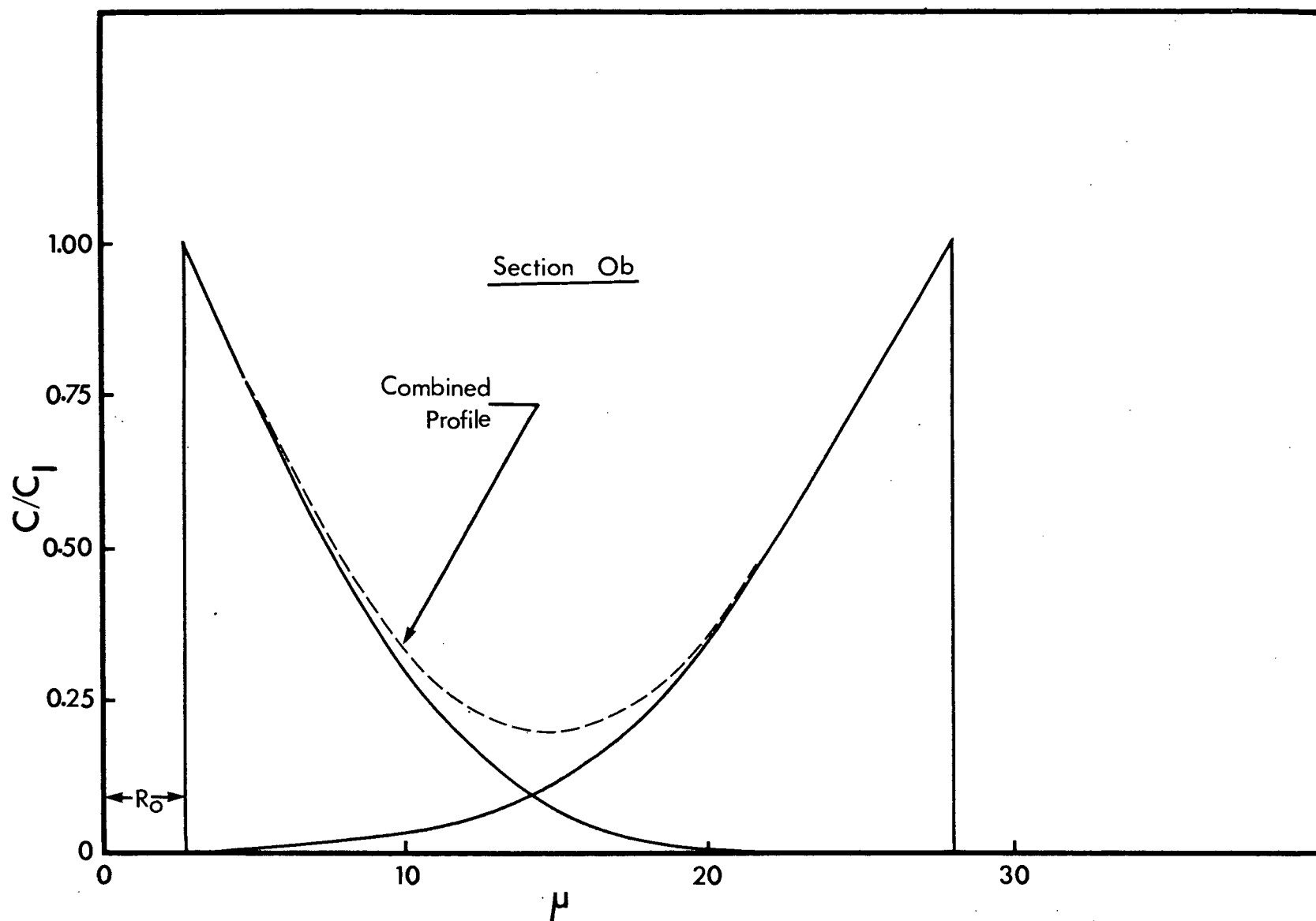


Figure 68(a). $[C/C_I]$ versus x for the minor axis Ob.

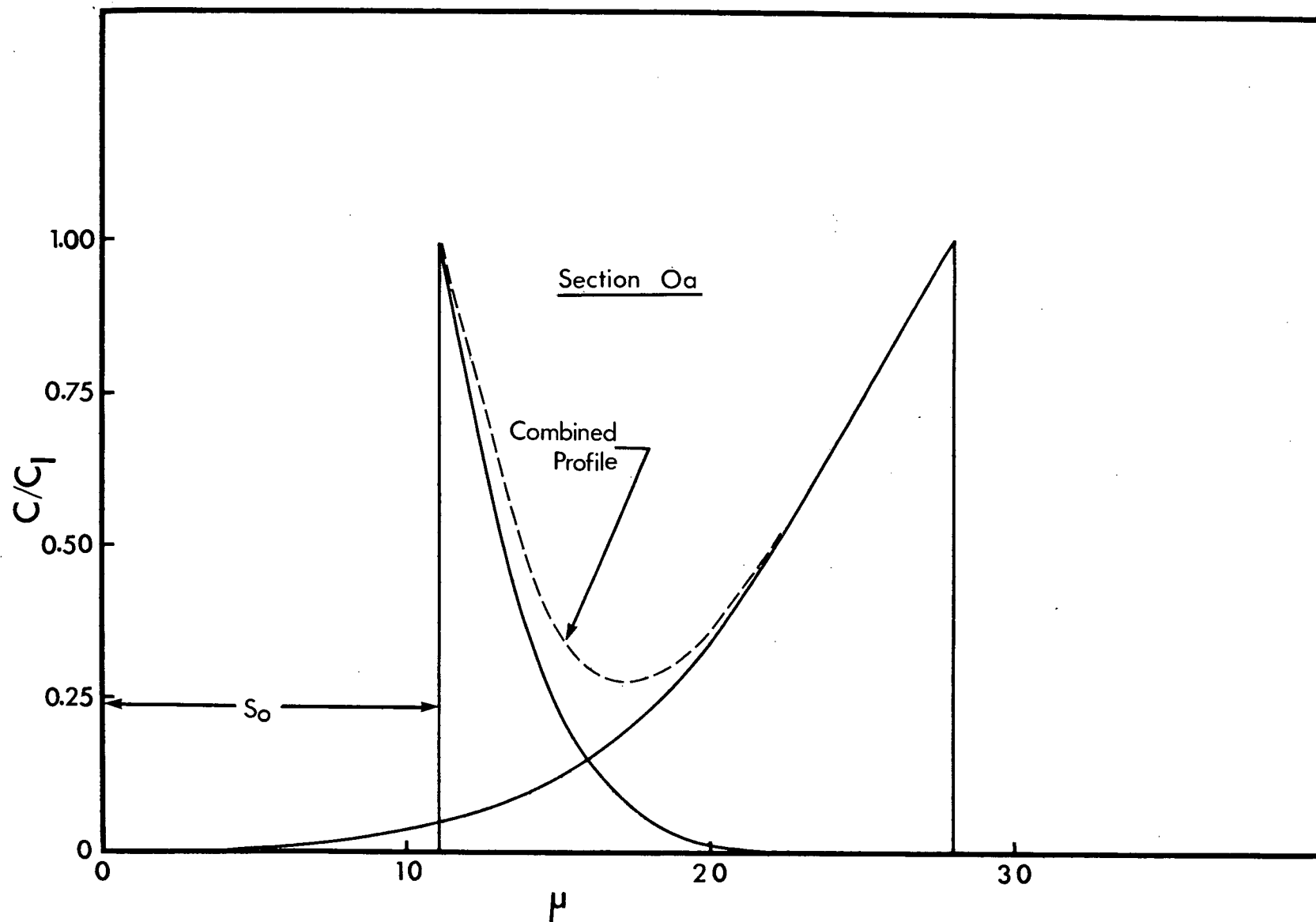


Figure 68(b). $[C/C_I]$ versus x for the equatorial plane Oa .

Thus if during the early stages of impingement, the low curvature surfaces are dissolving at a rate such as to maintain the axial ratio, then because of impingement, the high curvature equatorial region is dissolving at a rate slower than that required to maintain the axial ratio. The net result is therefore an increase in axial ratio. This effect will continue even after significant impingement.

4.4.2 Low Homologous Temperatures

At low homologous temperatures, the grain boundary diffusion coefficient is so much higher than the volume diffusion coefficient, that the grain boundary is effectively supersaturated with solute before any significant dissolution takes place, (see Figure 30, for concentration profiles at low T_H). This results in a solute concentration along the grain boundary which is equal to the interface solute concentration C_I .

Thus the tip of the allotriomorph tends to dissolve preferentially, with the corresponding solute moving along the grain boundary and dispersing from here into the matrix. This model for dissolution suggests a spheroidizing process with the tip dissolving much faster than the low curvature faces of the precipitate. However this tendency is probably reduced by interfacial diffusion⁵³ along the precipitate-matrix interface which would tend to feed solute to the grain boundary from other areas over the precipitate surface. A slight spheroidizing tendency is observed at low homologous in the present work.

4.4.3 Intermediate Homologous Temperatures

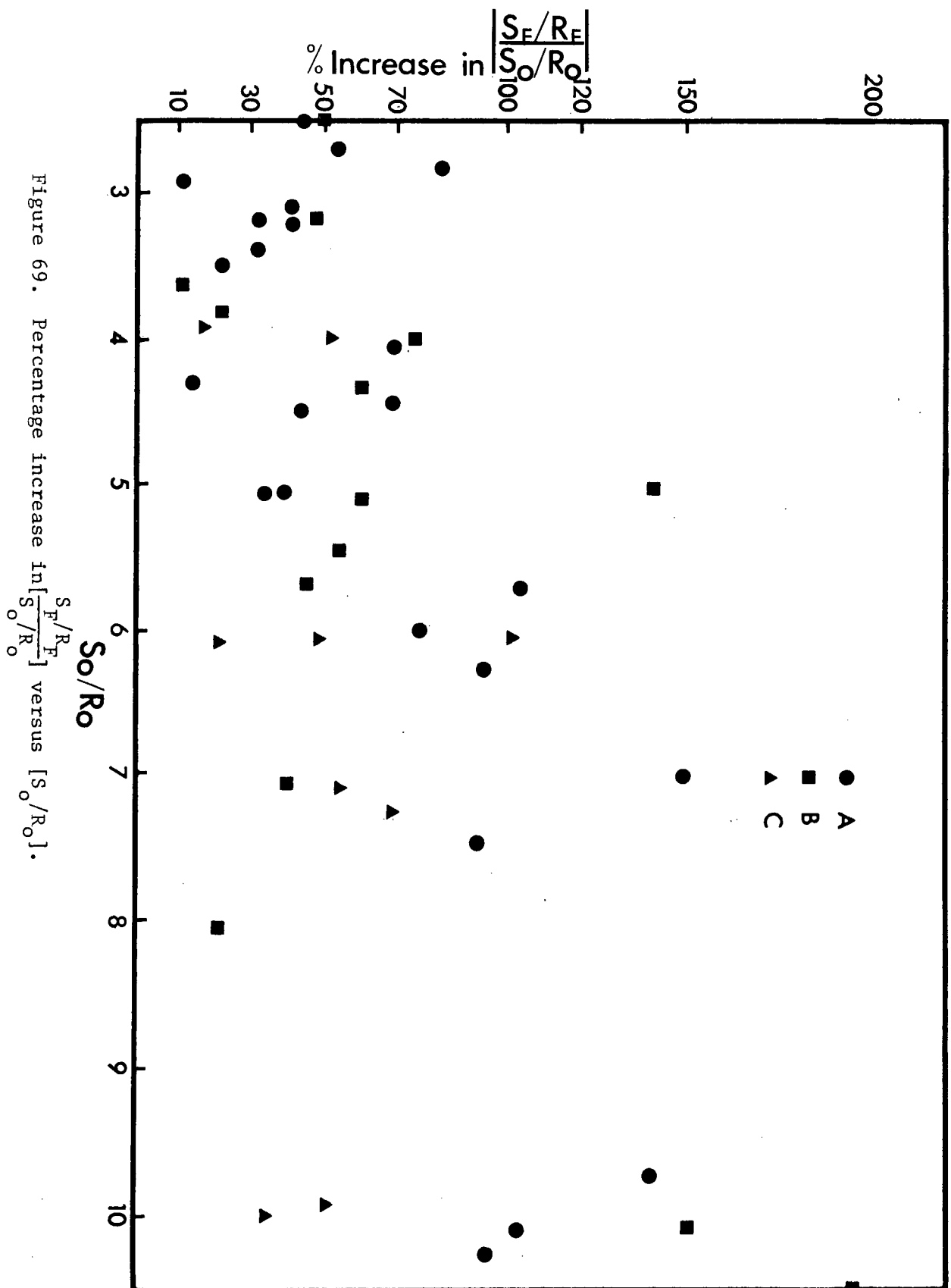
At intermediate homologous temperatures the tendencies applicable to both high and low homologous temperatures are probably operative. The relative importance of these tendencies is determined, among other things, by:

(1) The interparticle spacing on the grain boundary: For instance, it was qualitatively observed that in cases where a grain boundary precipitate was situated between two other grain boundary precipitates, the rate of change in half length S was reduced significantly.

(2) The initial axial ratio (S_o/R_o): This ratio is important in determining the degree to which earlier impingement of diffusion fields takes place at the tip as opposed to the sides of the allotriomorph. The model for high homologous temperatures indicates that the higher the initial axial ratio, (S_o/R_o), is, the earlier impingement of diffusion fields at the tip takes place, and therefore the greater is the expected increase in axial ratio.

In Figure 69 the percentage change in axial ratio ($S_F/R_F/S_o/R_o$) is plotted against (S_o/R_o). There is a definite trend towards a larger change in (S/R) with higher initial axial ratios, a result which is consistent with the preceding discussion.

A plot of $\log R/R_o$ versus t , (for a dissolution experiment at a temperature below the solvus line for an intermediate homologous temperature ($T_H = 0.83$ for alloy B)) in Figure 70(a), shows a good fit for the early stages of dissolution. A plot of $[S/R]$ versus t in Figure 70(b) shows a slight overall decrease in $[S/R]$ for the corresponding early stages of dissolution. All four precipitates



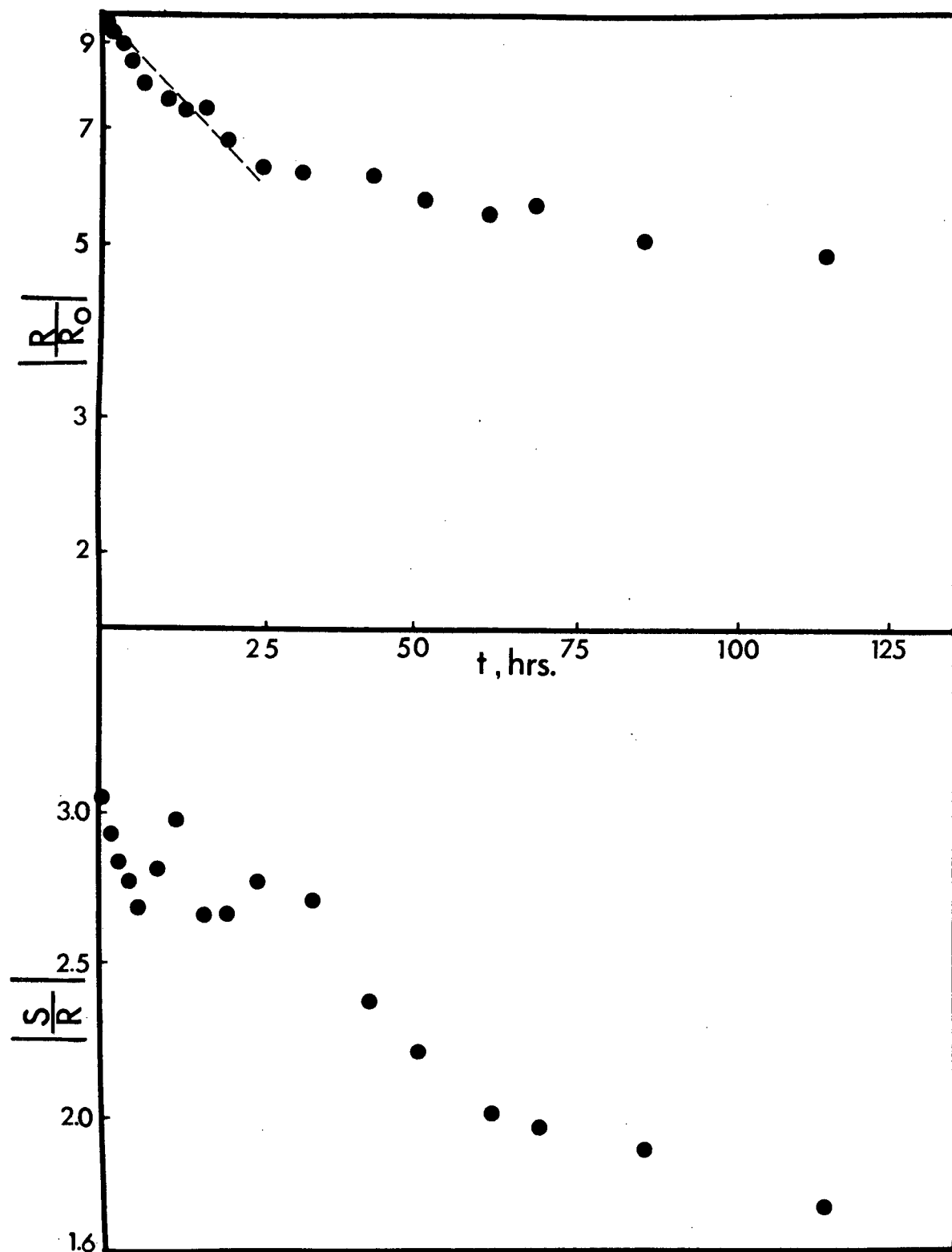


Figure 70. (a) $\log [R/R_0]$ versus t .

(b) $[S/R]$ versus t .

in this experiment show a small change in $[S/R]$ for the initial stages of dissolution. This is in good agreement with the predicted change in $[S/R]$ with homologous temperature shown in Figure 65.

It should be noted that the point of departure of the results from the exponential relationship in Figure 70(a) coincides reasonably well with the point in Figure 70(b) where rapid spheroidization begins to take place.

5. CONCLUSIONS

The results of the present study of the dissolution behaviour of grain boundary allotriomorphs in the Al-Cu and Al-Ag systems yield the following conclusions.

1. Isoconcentration contours around dissolving grain boundary allotriomorphs can be accurately determined by the use of electron probe microanalysis.
2. For allotriomorphs in an effectively infinite matrix, the shape of the isoconcentration contours is dependent only on the homologous temperature, T_H .
3. At a particular T_H , the relative contribution of grain boundary diffusion to volume diffusion can be obtained directly from the isoconcentration contours.
4. The dissolution of grain boundary allotriomorphs is dominated by volume diffusion above $T_H = 0.92$ and by grain boundary diffusion below $T_H = 0.72$. For the intermediate range $T_H = 0.92-0.72$, the grain boundary diffusion contribution increases continuously as T_H decreases.
5. Enhanced dissolution due to grain boundary diffusion is limited to precipitates on high angle grain boundaries. Grain boundary allotriomorphs are therefore the only precipitate morphology that will exhibit this phenomenon.
6. The dissolution kinetics of an individual grain boundary allotriomorph can be established from its back scattered electron image on the electron probe microanalyzer.
7. The dissolution kinetics of grain boundary allotriomorphs, under conditions in which impingement of diffusion fields from adjacent

precipitates takes place early in the dissolution process, are found to satisfy the following equations:

$$R = R_o e^{-\frac{\pi^2 Dt}{\ell^2}}$$

for the change in half thickness and

$$S = S_o e^{-\frac{\pi^2 Dt}{\ell^2}}$$

for the change in half length.

8. At high homologous temperatures, where volume diffusion dominates, an increase in the axial ratio of the allotriomorphs is observed as dissolution proceeds. On the other hand, at low homologous temperatures where grain boundary diffusion dominates, a slight decrease in axial ratio (i.e., slight spheroidization) is observed. A continuous change in behaviour from one extreme to the other is observed over the range of intermediate homologous temperatures.

BIBLIOGRAPHY

1. Dubé, C.A., Aaronson, H.I. and Mehl, R.F., *Rev. Mét.*, 55, 201 (1958).
2. Aaronson, H.I., The Mechanism of Phase Transformations in Metals, Inst. of Metals Monograph 18, 47 (1956).
3. Aaronson, H.I., Decomposition of Austenite by Diffusional Processes, Interscience Pub. N.Y. (1962), p. 387.
4. Clark, J.B., in High-Temperature, High-Resolution Metallography, Gordon and Beach Pub., N.Y., (1967).
5. Toney, S., and Aaronson, H.I., *Trans. A.I.M.E.*, 221, 909 (1961).
6. Hawbolt, E.B., and Brown, L.C., *Trans. A.I.M.E.*, 239, 1916 (1967).
7. Read, W.T., Jr., and Shockley, W., *Phys. Rev.*, 78, 275 (1950).
8. Vanghan, D., *Acta. Met.*, 16, 563 (1968).
9. Ryder, P.L. and Pitsch, W., *Acta. Met.*, 14, 1437 (1966).
10. Ryder, P.L., Pitsch, W., and Mehl, R.F., *Acta. Met.*, 15, 1431 (1967).
11. Zener, C., *J. Appl. Phys.*, 20, 950 (1949).
12. Frank, F.C., *Proc. Roy. Soc.*, A201, 586 (1950).
13. Ham, F.S., *J. Phys. Chem.* 6, 335 (1959a).
14. Ham, F.S., *J. Appl. Phys.* 30, 915 (1959c).
15. Horvay, G., and Cahn, J.W., *Acta. Met.*, 9, 695 (1961).
16. Mazanec, K., and Cadek, J., *Rev. Mét.*, 212, 501 (1958).
17. Hickley, C.M., and Woodhead, J.H., *J. Iron and Steel. Inst.* (London), 176, 129 (1954).
18. Aaron, H.B., and Aaronson, H.I., *Acta. Met.*, 16, 789 (1968).
19. Hillert, M., *Jernkontovets Ann.*, 141, 757 (1957).

20. Brailsford, A.D., and Aaron, H.B., J. Appl. Phys. 40, 1702 (1969).
21. Goldman, J., Aaronson, H.I., and Aaron, H.B., Met. Trans., 1, 1805 (1970).
22. Nolfi, Jr., F.V., Shewmon, P.G., and Foster, J.S., Trans. A.I.M.E., 245, 1427 (1969).
23. Nolfi, Jr., F.V., Shewmon, P.G., and Foster, J.S., Met. Trans. 1, 789 (1970).
24. Nolfi, Jr., F.V., Shewmon, P.G., and Foster, J.S., Met. Trans. 1, 2291 (1970).
25. Tanzilli, R.A., and Heckel, R.W., Trans. A.I.M.E., 242, 2313 (1968).
26. Tanzilli, R.A., and Heckel, R.W., Trans. A.I.M.E., 245, 1363 (1969).
27. Aaron, H.B., Fainstein, D., and Kotler, G.R., Publication Preprint Ford Motor Co. Scientific Laboratory, April, 1970.
28. Thomas, G., and Whelan, M.J., Phil. Mag., 6, 1103 (1961).
29. Whelan, M.J., Metal. Sci. Int. 3, 95 (1969).
30. Readey, D.W., and Cooper, Jr., A.R., Chem. Eng. Science, 21, 917 (1966).
31. Hall, M.G., and Haworth, C.W., Acta. Met., 18, 331 (1970).
32. Eifert, J.R., Chatfield, D.A., Powell, G.W., and Spretnack, J.W., Trans. A.I.M.E., 242, 66 (1968).
33. Tanzilli, R.A. and Heckel, R.W. Publication Preprint, Drexel Institute of Technology, Philadelphia, Pa. U.S.A.
34. Aaron, H.B., Acta. Met., 17, 407 (1969).
35. Aaron, H.B., and Kotler, G.R., Met. Trans. 2, 393 (1971).
36. Hansen, M., Constitution of Binary Alloys, 2nd ed., McGraw-Hill Book Co., N.Y. (1958), p. 2.
37. Metals Handbook, A.S.M., Cleveland, Ohio (1948), p. 1160.

38. Brown, L.C., Department of Met., U.B.C., Private Communication.
39. Murphy, J.B., Acta. Met., 9, 563 (1961).
40. Embury, J.D., and Nicholson, R.B., Acta. Met., 13, 403 (1965).
41. Pashley, D.W., Rhodes, J.W., and Sendorek, A., J. Inst. of Metals, 94, 41 (1966).
42. Aaron, H.B., and Kotler, G.R., Publication Preprint, Ford Motor Co., Scientific Laboratory (1970).
43. Achter, M.R., and Smoluchowski, R., Journal of Applied Physics, 22, 1260 (1951).
44. Smoluchowski, R., Physical Review, 83, 482 (1952).
45. Shewmon, P.G., J. Appl. Phys., 34, 755 (1963).
46. Fisher, J.C., J. Appl. Phys. 22, 74 (1951).
47. Turnbull, D., and Hoffman, R.E., Acta. Met., 2, 419 (1954).
48. Whipple, R.T.P., Phil. Mag., 45, 1225 (1954).
49. Heumann, Th., and Böhmer, H., J. Phys. Chem. Solids, 29, 237 (1968).
50. Aaron, H.B., Metal. Sci. 2, 192 (1968).
51. Crank, J., The Mathematics of Diffusion, The University Press, Oxford, p. 47 (1957).
52. Baty, D.L., Tanzilli, R.A., and Heckel, R.W., Met. Trans., 1, 1651 (1970).
53. Weinberg, F., Dept. of Met., U.B.C., Private Communication.
54. Reed, S.J.B., and Long, R.V.P., Proc. 3rd. Int. Symp. on X-Ray Optics and Micro-Analysis, Stanford Academic Press, N.Y. (1962).

55. Heinrich, K.F.J., Proc. of the Symp. on the Electron Microprobe, Washington, John Wiley, New York and London, 296 (1962).
56. Brown, L.C. and Thresh, H., Tools and Techniques in Physical Metallurgy, M. Dekker, N.Y. (1970).
57. Duncumb, P., and Reed, S.J.B., Technical Report No. 221, Tube Investments Research Laboratories, Hinxton Hall, Cambridge (May 1967).
58. Bethe, H.A., Ann. Phys. Lpz., 5, 325 (1930).
59. Belk, J.A., 4th Int. Congress on X-Ray Optics and Micro-Analysis Hermann Paris, Sept. 1965.
60. Poole, D.M., Proceedings of Seminar on Quantitative Electron Probe Microanalysis, Nat. Bur. of Stand. Special Pub. 298, Washington, p. 93 (1968).
61. Philibert, J., Proc. 3rd. Int. Symp. on X-Ray Optics and Micro-Analysis, Academic Press, N.Y., Stanford (1962).
62. Duncumb, P., and Shields, P.K., The Electron Microprobe, Wiley, N.Y. (1966).
63. Castaing, R., Advan. Electron. Electron Phys., 13, 317 (1960).
64. Murdoch, D.C., Analytic Geometry with an Introduction to Vectors and Matrices, John Wiley and Sons, Inc., N.Y. (1966)
65. Coates, D.E., Dept. of Met., U.B.C., Private Communication.
66. Hawbolt, E.B., Ph.D. Thesis, Dept. of Met., U.B.C. (1967).
67. Brown, L.C., Dept. of Met., U.B.C., unpublished work (1964).
68. Crank, J., Mathematics of Diffusion, The University Press, Oxford, p. 86 (1957).
69. Ham, F.S., Quart. Appl. Math. 17, 137 (1959).

APPENDIX I. Correction Procedures for Quantitative Electron Probe

Microanalysis

The measured X-ray intensity of element A in alloy AB may be converted to the true mass concentration (C_A) of element A in alloy AB, by applying the following corrections in the order indicated:

1. dead time;
2. background;
3. secondary fluorescent enhancement by characteristic radiation and white radiation;
4. X-ray mass absorption in the sample;
5. the atomic number effect, which is made up of two separate components:
 - (a) the electron stopping power (S);
 - and (b) the electron backscattering effect (R).

I.1 The Al-Cu System

Pure Cu was used as a reference standard for $\text{CuK}\alpha_1$ radiation. The $\text{CuK}\alpha_1$ peak was found at a Bragg angle of $26^\circ 34' \pm 3'$ using a quartz analyzing crystal to reflect the X-rays to the gas flow proportional counter. The background count was picked up on the second spectrometer at an angle of $27^\circ 4'$.

To convert the measured intensity of $\text{CuK}\alpha_1$ radiation to the concentration of Cu in the Al-Cu alloy only the deadtime, background, and atomic number corrections need be applied to the experimentally determined ratio of intensities (K_{Cu}) where:

$$K_{Cu} = \frac{I_{Al-Cu}^{K\alpha_1}}{I_{Cu}^{K\alpha_1}}$$

$I_{Al-Cu}^{K\alpha_1}$ = the $K\alpha_1$ radiation intensity of Cu in an Al-Cu alloy,

and $I_{Cu}^{K\alpha_1}$ = the $K\alpha_1$ radiation intensity of Cu in pure Cu.

A negligible secondary fluorescent enhancement is expected in this system and this was verified by applying the Reed and Long⁵⁴ correction for fluorescent excitation. The absorption for this system is also negligible as⁵⁵

$$\mu_{Al}^{Cu} \approx \mu_{Cu}^{Cu}$$

where $\mu_{Al}^{Cu} = 49.6$ = (mass absorption coefficient of $CuK\alpha_1$ radiation by Al) and $\mu_{Cu}^{Cu} = 53.7$ = (mass absorption coefficient of $CuK\alpha_1$ radiation by Cu).

(1) The dead time, d, may be calculated from the following relationship:⁵⁶

$$C_{(true)} = \frac{C_{(obs.)}}{1 - C_{(obs.)}d}$$

$C_{(true)}$ = true counts after the dead time correction is taken into consideration, $C_{(obs.)}$ = observed counts, d = dead time = .4 μ sec. for the electron probe used. This simple correction need only be

applied for high count rates (eg. >2,000 c.p.s.).

(2) The background count per ten seconds is registered for each ten second $\text{CuK}\alpha_1$ count. The background count is subtracted directly from the $\text{CuK}\alpha_1$ count, thereby eliminating the effect of background radiation.

(3) The Duncumb and Reed⁵⁷ atomic number correction was used to convert the intensity ratio of $\text{CuK}\alpha_1$ X-rays produced (K_{Cu}) to the true mass concentration of Cu (C_{Cu}). This correction has the form:

$$K_{\text{Cu}} = C_{\text{Cu}} \cdot \frac{R_{\text{Al-Cu}}}{R_{\text{Cu}}} \cdot \frac{S_{\text{Cu}}}{S_{\text{Al-Cu}}} \quad 1$$

where R = backscatter coefficient;

S = electron stopping power;

Al-Cu refers to the alloy specimen and Cu refers to the standard.

The stopping power is evaluated using the following equation:⁵⁸

$$S = \text{constant} \cdot \frac{Z}{A} \cdot \frac{1}{E} \cdot \ln \left(\frac{1.66 \cdot E}{J} \right) \quad 2$$

where Z = atomic number;

A = atomic weight;

J = mean ionization potential (tabulated values in reference 57);

E = electron energy ;

and the backscatter coefficient, R, is given by:

$$1 - R = \frac{\int_{E_K}^1 n(W) \cdot Q/S \cdot dW}{\int_{E_K}^{E_0} Q/S \cdot dE}$$

where: E_o = incident electron energy;

E_K = critical K excitation potential;

Q = ionization cross-section;

W = E/E_o ;

S as in equation 2.

$\eta(W)$ = backscattered electron energy distribution expressed in integral form.

Values of R are tabulated by Duncumb and Reid⁵⁷ as a function of $1/U$

($U = V/V_K$) and Z where: V = accelerating potential;

V_K = excitation potential of $K\alpha_1$ characteristic radiation.

Figure I-1 is a plot of C_{Cu} versus K_{Cu} for the Al-Cu system, after making the corrections described above.

The Belk⁵⁹ atomic number correction was applied to the Al-Cu system as a check on the validity of the Duncumb and Reed correction used and was found to be in good agreement with it. This correction procedure is very simple to apply and has the form:

$$K_A = \frac{C_A}{1 + \frac{Z_A - \bar{Z}}{100}}$$

$$\text{where } \bar{Z} = \frac{Z_A C_A + Z_B C_B}{C_A + C_B}$$

and Z = atomic number.

The above has been found by D. M. Poole⁶⁰ to be as accurate as any of the more sophisticated correction procedures.

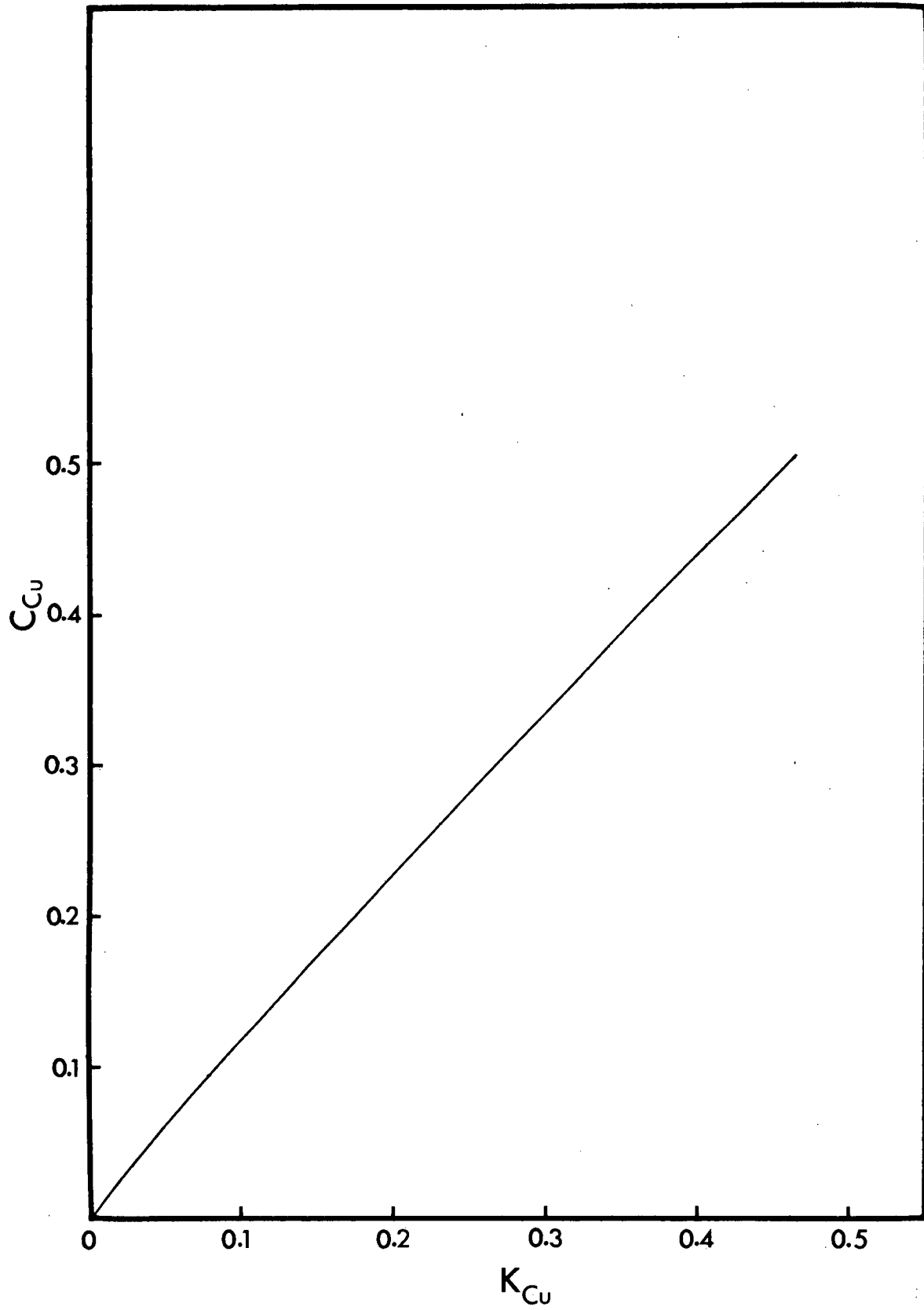


Figure I-1. C_{Cu} versus K_{Cu} .

I.2 The Al-Ag System

For this system the background, the dead time, the absorption and the atomic number correction, S, were used to convert measured $L\alpha_1$ X-ray intensity to the concentration of Ag in the alloy (C_{Ag}). The dead time, background and atomic number correction were applied in the same manner as for the Al-Cu system.

The following Philibert⁶¹ absorption correction was used

$$F(\chi) = f(\chi) \cdot F(0) = \frac{1}{(1 + \chi/\sigma)} [1 + h(1 + \chi/\sigma)]$$

where $f(\chi)$ = the fractional transmission after absorption and
represents the absorption effect only.

$F(0)$ = the atomic number effect only.

h = $1.2 A/Z^2$;

A = atomic weight;

χ = $\mu/\rho (\sec \theta)$;

μ/ρ = mass absorption coefficient;

θ = take off angle on the probe = 20° ;

σ = modified Leonard's coefficient as calculated by Duncumb and Shields⁶² and is given by

$$\sigma = \frac{2.39 \times 10^5}{E_o^{1.5} - E_K^{1.5}}$$

$$\mu_{Al}^{Ag 55} = 779.2$$

$$\mu_{Ag}^{Ag} = 521.9$$

Figure I-2 gives a calibration curve of C_{Ag} versus K_{Ag} for the Al-Ag system, after applying the corrections described above.

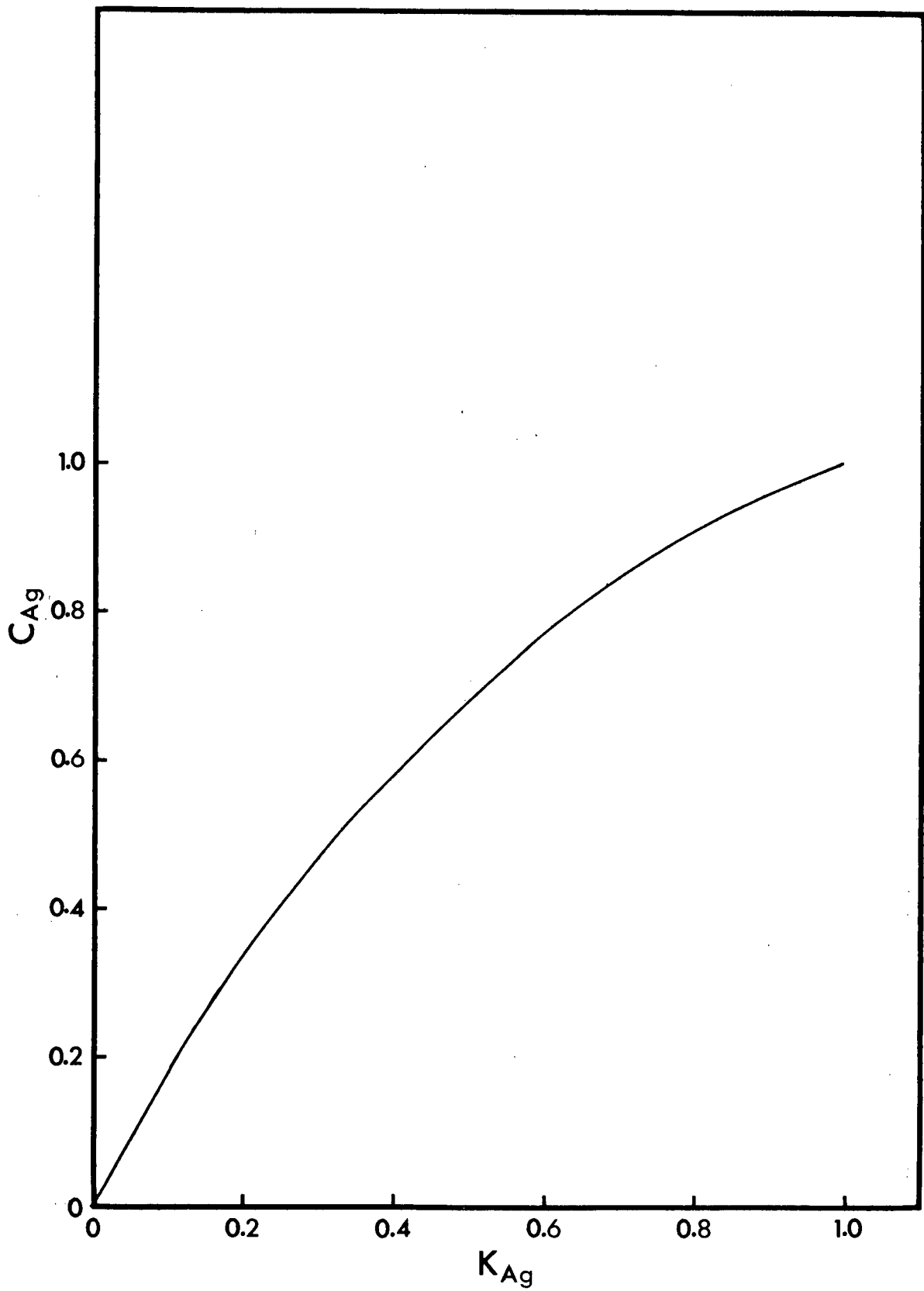


Figure I-2. C_{Ag} versus K_{Ag} .

APPENDIX II. Electron Spot Size Determination.

The electron spot size for the absorbed, backscattered and topographic electron image on the JEOLCO JXA 300 is approximately 0.7 μ . This corresponds to the resolution for these images. The X-ray spot size however varies according to the relationship:⁶³

$$\text{spot size } S = 0.033 (E_o^{1.7} - E_K^{1.7}) A / \rho Z$$

where E_o = operating voltage = 25 K.V.

E_K = excitation potential for the radiation considered;

and ρ = specimen density.

The relevant data is given in Table II-1.

Table II-1. E_K , A, Z and ρ Values for Ag $L\alpha_1$, Al $K\alpha_1$ and Cu $K\alpha_1$ Radiation.

	E_K (K.V.)	A	Z	ρ g cm ⁻³
Ag $L\alpha_1$	4.0	107.868	47	10.49
Al $K\alpha_1$	1.6	26.98	13	2.699
Cu $K\alpha_1$	9.0	63.546	29	8.96

A schematic diagram of the electron distribution in the sample is shown in Figure II-1. The total spot size is the sum of the electron beam diameter and the calculated spot size (S). On the basis of the above, the total spot size for the aluminium-rich matrix is $\approx 5.5 \mu$,

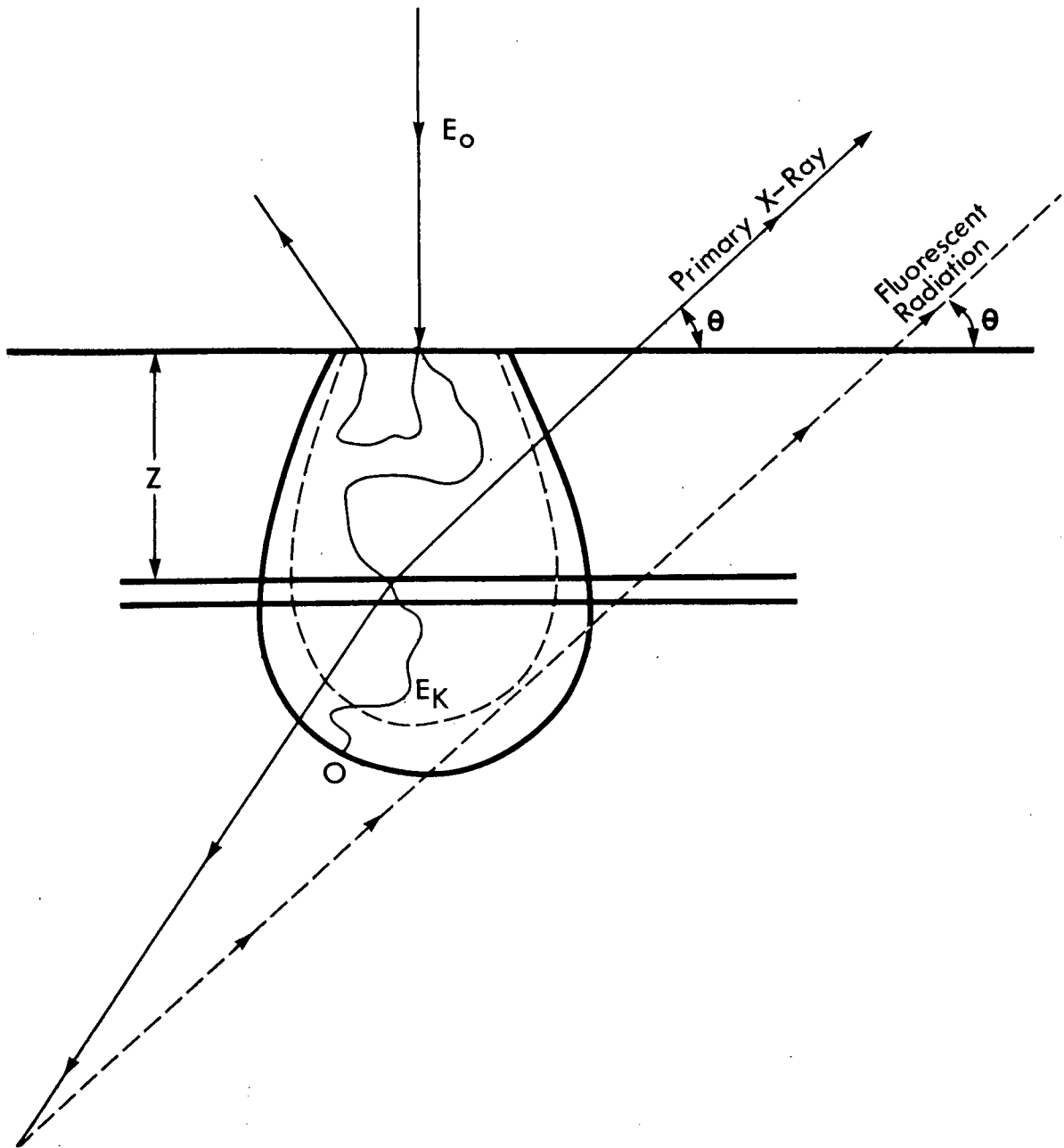


Figure II-1. Schematic diagram of the electron spot size.

taking into account the fact that the density of the α -solid solution is slightly larger than that for pure aluminum. The spot size for CuAl_2 is approximately 3μ , the spot size in the Ag rich matrix of the Ag-Al system is approximately 5μ , and the spot size in $\text{Ag}_3\text{Al} \approx 2.25 \mu$.

APPENDIX III. Calculation of the Flux Line Divergence for Different Sections of a Two Dimensional Elliptical Geometry.

The general equation for an ellipsoid as in Figure III-1(a) is given by:

$$\frac{x^2}{a^2} + \frac{y^2}{b^2} + \frac{z^2}{d^2} = 1$$

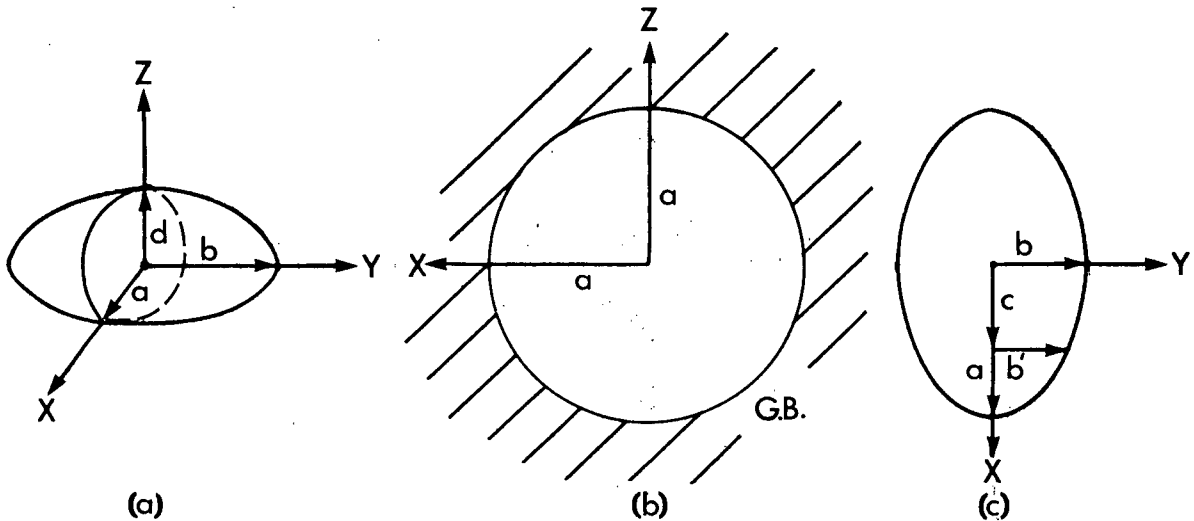


Figure III-1. Two dimensional sections of an oblate spheroid.

If $a = d > b$ one obtains an oblate spheroid, whereas if $a = b < d$ one obtains a prolate spheroid. Assume a grain boundary allotriomorph can be approximated by an oblate spheroid and assume the grain boundary lies on the $y = 0$ plane (i.e. x-z plane), (Figure III-1(b)). A cross section perpendicular to the grain boundary, the $z=0$ plane (i.e. x-y plane), is shown in Figure III-1(c) which is an ellipse of equation

$$\frac{x^2}{a^2} + \frac{y^2}{b^2} = 1 \quad 1$$

If c is the focal length of the ellipse, the following relationships exist⁶⁴

$$e = c/a = \text{eccentricity},$$

and $a^2 = b^2 + c^2$

If $c \rightarrow a$, $e = 1$, and $b \rightarrow 0$, therefore the spheroid reduces to a disc.

If $c \rightarrow 0$, $e = 0$, and $a = b$, therefore the spheroid reduces to a sphere.

In the Al-Cu system the most common allotriomorphs present have an axial ratio of 3.5. With an axial ratio, $a/b = 3.5$, Eq (1) is used to determine the angle between the tangent to the ellipse at $x = 0, y = b$, and at arbitrary values of x and y . Results are given in Table III-1.

Table III-1 $\Delta\theta^\circ$ for Different Values of x/b .

x/b	y/b	$\Delta\theta^\circ$
0	1	0
0.875	0.97	4
1.75	0.867	10
2.625	0.658	20
3.20	0.407	39

APPENDIX IV. D_V Calculation from the Diffusion Couple Results

As shown in Figure 16, a probability plot of $C_{(x,t)}$ versus x within the supersaturated α phase gives a straight line for the diffusion couple annealed at 500°C. Consequently a volume diffusion coefficient D_V , which is independent of concentration, is indicated.

All the diffusion couple results when plotted on probability paper gave diffusion coefficients independent of concentration. In Figure IV-1, the concentration profile at 500°C is used to evaluate D_V from the equation

$$D_V = \frac{Z^2}{\pi t} \quad 1$$

where Z is the point at which the tangent to the concentration gradient at the interface cuts the concentration line $C=0$. This equation gives accurate values of D_V when $D_V \neq f$ (concentration), and the interface is essentially stationary. From Figure IV-1

$$D_V = \frac{(2.80 \times 10^{-2})^2}{\pi \times 163 \times 3,600} = 4.26 \times 10^{-10} \text{ cm}^2/\text{sec}$$

D_V values were also determined in an alternate manner using the probability plots for each of the four diffusion couples. Using a standard diffusion coefficient, $D_S = 5 \times 10^{-10} \text{ cm}^2 \text{ sec}^{-1}$, and the appropriate value of time, a standard line was calculated and drawn on each probability plot. Then D_V could be calculated from the relationship:

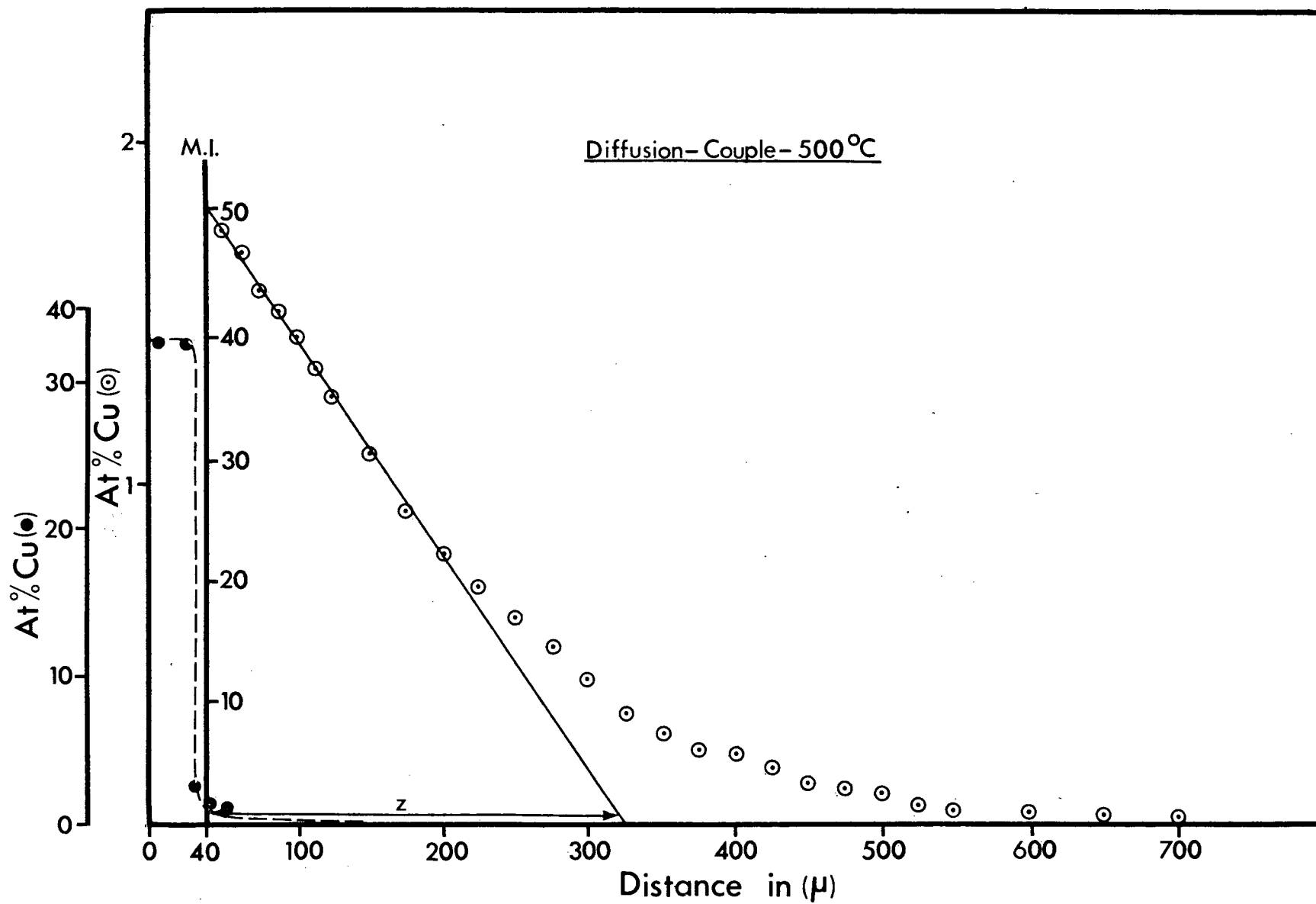


Figure IV-1. Composition profile of diffusion couple at 500°C.

$$\left(\frac{x_S}{x_V}\right)^2 = \frac{D_S}{D_V}$$

2

where x_S and x_V are the diffusion distances in the aluminum corresponding to the same copper concentration for the standard and experimental lines respectively. The value of D_V calculated in this way at 500°C differs only in the second decimal place from the D_V value calculated using equation 1.

Table IV-1. D_V Values of the Diffusion Couple Results.

$$x_S(50-1\%) = 560 \mu \quad x_S^2 = 31.36 \times 10^4 \mu^2$$

T°C	T°K	$1/T^\circ K^{-1} \times 10^4$	x_V, μ (50-1%)	$x_V^2 \times 10^{-4} \mu^2$	$D_V \times 10^{10} \text{ cm}^2 \text{ sec}^{-1}$
480	753	13.28	368	13.54	2.16
500	773	12.94	514	26.40	4.21
520	793	12.60	700	49.00	7.80
535	808	12.38	745	55.50	8.84

APPENDIX V. Calculation of Standard Deviation for the Isoconcentration Contours.

The mean (\bar{X}) of a set of data X_i is given by:

$$\text{Mean} = \bar{X} = \frac{\sum_{i=1}^n X_i}{n}$$

The standard deviation (σ) is given by:

$$\text{Standard deviation} = \sigma = \sqrt{\frac{\sum_{i=1}^n (X_i - \bar{X})^2}{n-1}}$$

Table V-1 gives the mean (\bar{X}) and standard deviation (σ) for the dissolution results of 5 precipitates in alloy B at $T_H = 0.91$ shown in Figure 19.

Table V-1. Diffusion Distance, \bar{X} , σ and $\frac{\sigma}{\bar{X}}$

Precipitate number	At centre 90 sec		At centre 360 sec	
	<u>2.1%</u>	<u>2.5%</u>	<u>2.1%</u>	<u>2.5%</u>
1	10.62	6.87	20	13.2
2	9.37	6.87	17.5	15.0
1	10.00	5.63	17.5	10.0
2	8.75	6.25		13.5
1	10.00	6.87	17.5	11.25
2	8.75	5.0	16.25	11.25
1	8.75	5.63	17.5	11.25
1	10.00	6.25	11.25	
2	8.75	5.63	16.87	11.25

Table continued.....

Table V-1 Continued

	<u>2.1%</u>	<u>2.5%</u>	<u>2.1%</u>	<u>2.5%</u>
\bar{X}	9.44	6.11	17.59	11.88
σ	0.73	0.73	1.17	1.47
σ/\bar{X}	0.08	0.11	0.066	0.11

APPENDIX VI. Calculation of ψ

Coates⁶⁵ has attempted to calculate, as a function of temperature, the relative contributions of volume and grain boundary diffusion to dissolution of grain boundary allotriomorphs. The following is an outline of his calculation. Consider the grain boundary to lie on the x-y plane. The allotriomorph is approximated by an oblate spheroid whose major axis is in the x-y plane (i.e., an ellipse in the x-z plane is rotated about its minor axis, the z axis). The foci are at $x = \pm c$ and the semi-major and semi-minor axes are a and b respectively (i.e., the spheroid intersects the x, y and z axes at $\pm a$, $\pm a$ and $\pm b$ respectively).

The first step in the calculation is to determine the distribution of solute (the diffusion field) about the precipitate assuming only volume diffusion. Provided the supersaturation is low, the diffusion field can be approximated by a solution of Laplace's equation $\nabla^2 C = 0$. Physically this is equivalent to assuming a steady state distribution of solute. Using this approximation the diffusion field about the allotriomorph is determined. Then the interface gradient of this field $\vec{\nabla}_I C$ is computed to give in turn the interface flux $\vec{J}_I = -D_V \vec{\nabla}_I C$. Finally the total interface outflow of material from the allotriomorph, $\int_I \vec{J}_I \cdot \vec{dA}$; is calculated to give

$$\left(\int_I \vec{J}_I \cdot \vec{dA} \right)_{\text{vol.}} = \frac{4\pi D_V (C_I - C_M) c}{\pi/2 - \tan^{-1} [\{(a/b)^2 - 1\}^{-1/2}]} \quad 1$$

where C_I and C_M are the interface and bulk matrix concentrations respectively, and a/b is the axial ratio of the spheroid.

The next principal step is the calculation of the diffusion field about the allotriomorph assuming the material leaves via the grain boundary only. Thus one is effectively considering diffusion from a cylindrical source (the precipitate) of radius a and height δ (the grain boundary thickness). Shewmon⁴⁶ has modified the Fisher⁴⁷ analysis of grain boundary diffusion so that it is applicable to the same cylindrical symmetry as is involved here. Using Shewmon's solution for the distribution of solute in the grain boundary, Coates calculates the interface flux $\vec{J}_S = -D_S \nabla_I \vec{C}$. The total interface outflow of material from the allotriomorph is simply

$$\int_I \vec{J}_I \cdot d\vec{A} = 2\pi a \delta J_I, \text{ i.e.,}$$

$$\left(\int_I \vec{J}_I \cdot d\vec{A} \right)_{g.b.} = 2\pi a \delta D_S \alpha (C_I - C_M) \frac{K_1(\alpha a)}{K_0(\alpha a)} \quad 2$$

$$\text{where } \alpha = \sqrt{\frac{2}{\delta (\pi D_V \tau)^{1/2} D_S / D_V}} \quad 3$$

τ is time and K_0 and K_1 are modified Bessel Functions of zeroth and first order respectively.

Now a function ψ is defined such that

$$\psi \equiv \frac{\left(\int_I \vec{J}_I \cdot d\vec{A} \right)_{g.b.}}{\left(\int_I \vec{J}_I \cdot d\vec{A} \right)_{vol.}} \quad 4$$

which is to be used as an index of the relative contributions of volume and grain boundary diffusion.

If $\psi \gg 1$, grain boundary diffusion dominates.

If $1/\psi \gg 1$, volume diffusion dominates.

After substituting equations (1), (2) and (3) into (4), Coates obtains, after considerable rearrangement:

$$\psi = \sqrt{\frac{D_S/D_V \delta}{2(\pi D_V \tau)^{1/2}}} \cdot \frac{K_1(\alpha a)}{K_0(\alpha a)} f(a/b) \quad 5$$

$$\text{where } f(a/b) = \frac{a/b[\pi/2 - \tan^{-1}\{(a/b)^2 - 1\}^{-1/2}]}{\sqrt{(a/b)^2 - 1}} \quad 6$$

Notice that the supersaturation ($C_I - C_M$) has cancelled out in Equation (6). For a sphere ($a/b = 1$) and a flat disk ($a/b = \infty$), the corresponding values of $f(a/b)$ are 1 and $\pi/2$ respectively. Clearly therefore, axial ratio has little influence since $f(a/b)$ is the only term in equation (5) in which axial ratio appears. The factor $\sqrt{\pi D_V \tau}$ is approximately the characteristic diffusion distance for the matrix.

Notice that D_S appears only in the ratio D_S/D_V (cf. equations (3) and (5)). Assume that $D_V = D_0 e^{-Q/RT}$, where Q is the activation energy for volume diffusion. If the activation energy for grain boundary diffusion is $\sim Q/2$ and the pre-exponential remains unchanged, then

$$D_S/D_V \approx e^{Q/2RT}$$

which can be substituted into equations (3) and (5) to give Coates' final result:

$$\psi = \sqrt{\frac{e^{Q/2RT} \delta}{2(\pi D_V \tau)^{1/2}}} \cdot \frac{K_1 \left[a \sqrt{\frac{2e^{-Q/2RT}}{\delta(\pi D_V \tau)^{1/2}}} \right]}{K_0 \left[a \sqrt{\frac{2e^{-Q/2RT}}{\delta(\pi D_V \tau)^{1/2}}} \right]} f(a/b) \quad 8$$

For a given precipitate size a and diffusion distance $(\pi D_V \tau)^{1/2}$ equation (8) is essentially an equation of the form

$$\psi = \psi(T)$$

i.e. a function describing the relative contributions of volume and grain boundary diffusion as a function of temperature.

APPENDIX VII. Calculations of the Impingement Resulting from the Interaction of the Confocal Spheroids about an Allotriomorph and a Surrounding Concentric Spherical Field.

For the field around the ellipsoid A in Figure 66(c) assume that the diffusion distances are shorter than the sphere radius so that we can consider the precipitate is dissolving in an infinite medium. Consider that the concentration contours are a series of confocal spheroids; in the case of a dissolving precipitate the profiles will be less spherical than this at short times as may be seen in Figure VII-1. As discussed in the text this will make the axial ratio increase faster on dissolution. The equation for confocal oblate

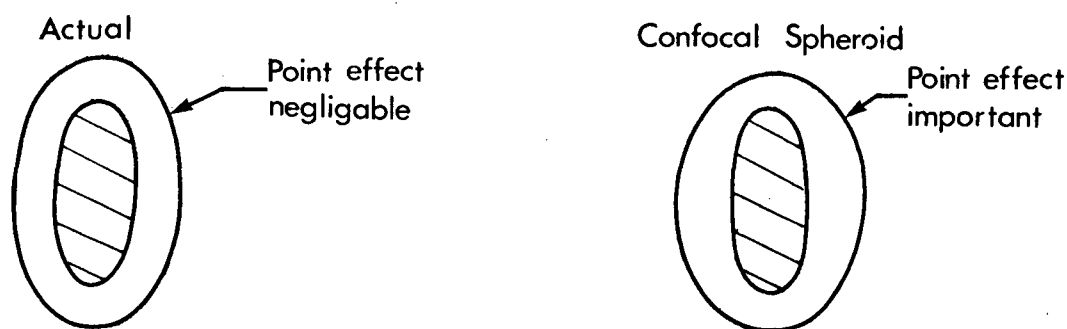


Figure VII-1. Schematic diagram comparing actual contour to confocal spheroid.

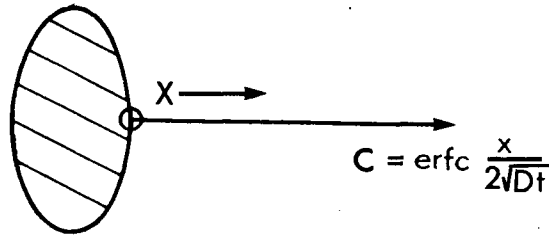
spheroids is given by⁶⁹:

$$\frac{x^2}{\eta_1^2 - \beta^2} + \frac{y^2}{\eta_1^2} + \frac{z^2}{\eta_1^2} = 1 \quad 1$$

In two dimensions the contour shapes are defined by:

$$\frac{x^2}{\eta_1^2 - \beta^2} + \frac{y^2}{\eta_1^2} = 1 \quad 2$$

The value of β (the focal length) may be obtained directly for the case of growth from a plot of the square of the minor axis $(\eta_1^2 - \beta^2)$ versus the axial ratio $\frac{\eta_1}{(\eta_1^2 - \beta^2)^{1/2}}$ for various values of the supersaturation (f) by L.C. Brown.⁶⁷ From analogy with growth at $f = 0.1$ and an axial ratio of 4, $\beta = 1.095$ and η_1 is found to vary from 1.13 to 2.82. The actual concentrations are calculated assuming that the profile at the centre of the flat face of the oblate spheroid is an error function as in Figure VII-2.



3

Figure VII-2. Position of error function profile.

Distances are $\frac{x}{2\sqrt{Dt}} = [(\eta_1^2 - \beta^2)^{1/2} - 0.283]$ where: $\beta = 1.095$,

$\eta_1 = 1.13$; $\frac{\eta_1}{(\eta_1^2 - \beta^2)^{1/2}} = 4$; and $(\eta_1^2 - \beta^2)^{1/2} = 0.283$. The confocal spheroids are calculated for $D = 5 \times 10^{-10} \text{ cm}^2 \text{ sec}^{-1}$ and $t = 500$ seconds.

$$2\sqrt{Dt} = 2 \sqrt{25 \times 10^{-8}} = 10 \mu$$

The length of the semi-minor axis will therefore be $10 \times (\eta_1^2 - \beta^2)^{1/2}$ and the semi-major axis will be $10\eta_1$. These values are listed in Table VII-1.

Table VII-1. Values of $(\eta_1^2 - \beta^2)^{1/2}$ and η_1 of Confocal Spheroids for Different C/C_I Ratios.

$[C/C_I]$	$\frac{x}{2\sqrt{Dt}}$	x	$10(\eta_1^2 - \beta^2)^{1/2}$	$10\eta_1$
1	0	0	2.83	11.3
0.75	0.23	2.3	5.1	12.1
0.5	0.48	4.8	7.6	13.5
0.25	0.81	8.1	10.9	15.5
0.1	1.16	11.6	14.4	18.1
0.05	1.39	13.9	16.7	20.0

For diffusion inward from the sphere, again consider that diffusion distances are shorter than the sphere radius so that the presence of the oblate spheroid can be neglected. The profile is of the form

$$C/C_I = a/r \sum_{n=0}^{\infty} \left[\operatorname{erfc} \frac{(2n+1)a-r}{2\sqrt{Dt}} - \operatorname{erfc} \frac{(2n+1)a+r}{2\sqrt{Dt}} \right] \quad 4$$

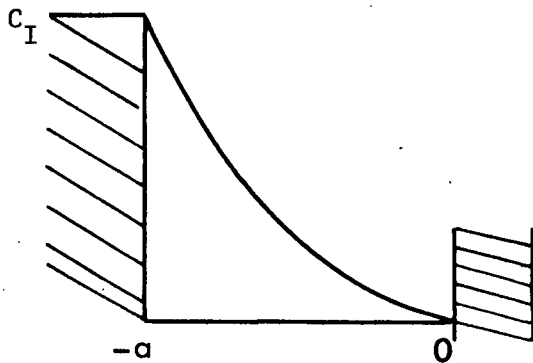


Figure VII-3. Pertaining to Equation 4

Calculations for the concentric spheres are made using a plot of C versus r/a for different values of Dt/a^2 in Crank⁶⁸ (page 86, Figure 6.1). In this case

$$\left[\frac{Dt}{a^2}\right] = \frac{5 \times 10^{-10} \times 500}{(28 \times 10^{-4})^2} = 0.0319$$

Table VII-2 gives the locations of the concentric spheres for various $[C/C_I]$ ratios.

Table VII-2. Values of r for Concentric Spheres for Different C/C_I Ratios.

$[C/C_I]$	r/a	r, μ
1	1	28.3
0.75	0.89	24.9
0.50	0.79	22.2
0.25	0.66	18.5
0.10	0.51	14.3
0.05	0.42	11.8

The actual profile can be found by summing these two independent profiles as in Figure VII-4. The final profiles are given in Figures 67 and 68 on pages 134-136.

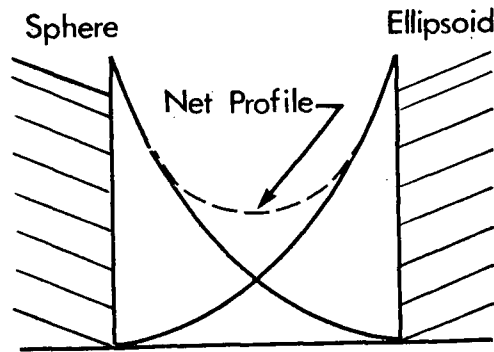


Figure VII-4. Schematic diagram of the summing up of two independent profiles.